ANÁLISE DOS MODOS DINÂMICOS DE ESCOAMENTO TRANSÔNICO EM TORNO DE UM CILINDRO

ANALYSIS OF THE DYNAMIC MODES OF TRANSONIC FLOW PAST A CYLINDER

Guilherme Mendes Santana

Dissertação de Mestrado
Ciências Mecânicas

27 de Junho de 2023

UNIVERSIDADE DE BRASÍLIA

Faculdade de Tecnologia
Departamento de Engenharia Mecânica

UNIVERSIDADE DE BRASÍLIA
FACULDADE DE TECNOLOGIA
DEPARTAMENTO DE ENGENHARIA MECÂNICA

ANALYSIS OF THE DYNAMIC MODES OF TRANSONIC FLOW PAST A CYLINDER

Guilherme Mendes Santana

Orientador: Prof. Adriano Todorovic Fabro, PhD (ENM/UnB)

Co-orientador: Prof. Roberto Francisco Bobenrieth Miserda, D.Sc. (ENM/UnB)

DISSERTAÇÃO DE MESTRADO

BRASÍLIA/DF: 27 de junho de 2023

UNIVERSIDADE DE BRASÍLIA
FACULDADE DE TECNOLOGIA
DEPARTAMENTO DE ENGENHARIA MECÂNICA

Analysis of the Dynamic Modes of Transonic Flow Past a Cylinder

Guilherme Mendes Santana

DISSERTAÇÃO DE MESTRADO SUBMETIDA AO DEPARTAMENTO DE ENGENHARIA MECÂNICA DA FACULDADE DE TECNOLOGIA DA UNIVERSIDADE DE BRASÍLIA COMO PARTE DOS REQUISITOS NECESSÁRIOS PARA A OBTENÇÃO DO GRAU DE MESTRE EM CIÊNCIAS MECÂNICAS.

APROVADA POR:

Prof. Adriano Todorovic Fabro, PhD (ENM/UnB)
(Orientador)

Prof. Roberto Francisco Bobenrieth Miserda, D.Sc. (ENM/UnB)
(Co-orientador)

Prof. Taygoara Felamingo de Oliveira, D.Sc. (ENM/UnB)
(Examinador Interno)

Prof. Samuel da Silva, D.Sc. (DEM/UNESP - Ilha Solteira)
(Examinador Externo)

BRASÍLIA/DF, 27 DE JUNHO DE 2023.

FICHA CATALOGRÁFICA

Santana, G.M.
Análise dos Modos Dinâmicos de Escoamento Transônico em Torno de um Cilindro
[Distrito Federal] 2023.
xv, 86p. (ENM/FT/UnB, Mestre, Ciências Mecânicas, 2023.
Dissertação de Mestrado - Universidade de Brasília.
Faculdade de Tecnologia.
Departamento de Engenharia Mecânica.
Palavras-chave:

1. Eascoamento Transônico	2. Aeroacoústica Computacional
3. Decomposição em Modos Dinâmicos	4. Decomposição Ortogonal Prórpia
5. Escoamento em torno do Cilindro	6. Escoamento Invíscido
I. ENM/FT/UnB	II. Título (série)

REFERÊNCIA BIBLIOGRÁFICA

Santana, G.M.(2023). Analysis of the Dynamic Modes of Transonic Flow Past a Cylinder. Dissertação de Mestrado, Departamento de Engenharia Mecânica, Universidade de Brasília, Brasília, Distrito Federal, xv, 86p.

CESSÃO DE DIREITOS

NOME DO AUTOR: Guilherme Mendes Santana.

TÍTULO DA DISSERTAÇÃO DE MESTRADO: Análise dos Modos Dinâmicos de Escoamento Transônico em Torno de um Cilindro.

GRAU / ANO: MESTRE / 2023

Guilherme Mendes Santana

Agradecimentos

Agradeço primeiramente aos meus orientadores, os Professores Adriano Fabro e Roberto Miserda, por toda a ajuda e apoio durante a realização deste trabalho, e também por me introduzirem ao tema de dinâmica baseada em dados. Agradeço também aos membros da banca examinadora, professores Taygoara de Oliveira e Samuel da Silva, pelas numerosas sugestões e contribuições para a versão final da dissertação, além de ideias para trabalhos futuros.

Agradeço também aos demais professores e funcionários do Programa de Pós Graduação em Ciências Mecânicas e do Departamento de Engenharia Mecânica da Universidade de Brasília por todas as contribuições para a minha formação e à CAPES pelo auxílio através de uma bolsa de estudos.

Por fim, agradeço à minha família e aos meus amigos e colegas pelo apoio e suporte durante a realização deste trabalho.

Resumo

As abordagens mais comuns em aeroacústica computacional são a computação direta do ruído, através da solução das equações governantes, e o uso de equações lineares para descrever a propagação do som. Uma alternativa interessante a esses métodos é o uso de um modelo baseado em dados, como os fornecidos pela Decomposição em Modos Dinâmicos (DMD) e pela Decomposição Ortogonal Própria (POD) são ferramentas de análise direcionadas por dados. Neste contexto, esta dissertação visa utilizar os métodos POD e DMD para estudar o escoamento transônico bidimensional em torno de um cilindro com números de Mach 0,5 e 0,75, modelado com as equações de Euler. O escoamento ao redor do cilindro foi escolhido como objeto deste trabalho por ser um problema clássico da mecânica dos fluidos mas que apresenta uma dinâmica rica. A aceleração do escoamento ao passar pelo cilindro causa a formação de ondas de choque, e o gradiente de pressão adverso resultante causa a separação do escoamento. À medida que os vórtices são emitidos e formam uma esteira de von Karman, as ondas de choque também se separam e se propagam pelo domínio como ondas sonoras. Os números de Strouhal para ambos os casos ficaram em torno de 0,2, o valor clássico para o escoamento ao redor de um cilindro. O POD e o DMD são métodos que decompõem um conjunto de dados, neste caso composto por campos de pressão, em estruturas coerentes, também conhecidas como modos. Os modos do POD são estruturas espacialmente ortogonais, enquanto os modos do DMD têm frequências e taxas de crescimento específicas. A análise das estruturas dos modos revelou que o cilindro emite ruído de forma semelhante a um dipolo acústico, com contribuições de outros multipolos. Além disso, os modos para $M_\infty = 0,75$ revelaram que a esteira de vorticidade também é uma fonte de ruído no escoamento. A decomposição em modos dinâmicos (DMD) também forneceu frequências associadas aos modos que corresponderam aos picos nos espectros de pressão. Os modos POD e DMD também foram usados para reconstruir os escoamentos. Os resultados obtidos com o POD coincidiram quase exatamente com os dados originais, enquanto os obtidos com o DMD apresentaram mais discrepâncias. Para $M_\infty = 0,5$, o erro da raiz da média quadrática das flutuações de pressão ficou entre 15% e 25% na maior parte do domínio, mas teve um valor máximo de mais de 200%, mas a frequência e a amplitude das oscilações representaram razoavelmente bem os dados originais. Os resultados mostraram que o POD e o DMD são ferramentas de análise interessantes, capazes de revelar características importantes sobre o sistema estudado, mas o POD é

melhor para a reconstrução dos escoamentos.

Palavras-chaves: Eascoamento Transônico; Aeroacoústica Computacional; Decomposição em Modos Dinâmicos; Decomposição Ortogonal Prórpia; Escoamento em torno do Cilindro; Escoamento Invíscido.

Abstract

The most common approaches for computational aeroacoustics are the direct noise computation through the solution of the governing equations and the use of linear equations to describe sound propagation. An interesting alternative to these methods is a data-driven approach. The Dynamic Modes Decomposition (DMD) and the Proper Orthogonal Decomposition (POD) are analysis tools that have been used recently that also provide data-based models. With that in mind, this dissertation aims to use the POD and DMD methods to study the transonic flow past a 2D circular cylinder with Mach numbers 0.5 and 0.75 and modelled with the Euler equations. The flow past the cylinder was chosen as the subject of this work because it is a classical problem in fluid mechanics but presents rich dynamics. The acceleration of the flow as it passes around the cylinder causes the formation of shock waves, and the resulting adverse pressure gradient causes the separation of the flow. As vortices are emitted and form a von Karman street at the wake, the shock waves also detach and propagate through the domain as sound waves. The Strouhal numbers for both cases were around 0.2, the well-known value for the flow around a cylinder. The POD and DMD are methods that decompose a data set, in this case composed of pressure field snapshots, into coherent structures, or modes. The POD modes are spatially orthogonal structures, while the DMD modes have specific frequencies and rates of growth. The analysis of the modes' structures revealed that the cylinder emits noise in a manner similar to an acoustic dipole, with contributions from other multipoles. Furthermore, the modes for $M_\infty = 0.75$ revealed that the vortex wake is also a noise source in this case. The DMD decomposition also provided frequencies associated with the modes that matched the peaks in the pressure spectra. The POD and DMD modes were also used to reconstruct the flow fields. The reconstruction with the POD agreed almost exactly with the original data, while those obtained with the DMD presented more discrepancies. For $M_\infty = 0.5$ the error for the pressure fluctuations root mean square value was around 15% to 25% for most of the domain and had a maximum value of over 200%, but the frequency and amplitude of the sound waves represented the original data reasonably well. The results showed that the POD and the DMD are interesting analysis tools, capable of revealing important information about the system but the POD is a better method to reconstruct the data set.

Key-words: Transonic Flow; Computational Aeroacoustics; Dynamic Modes Decomposition; Proper Orthogonal Decomposition; Flow Past a Cylinder; Inviscid Flow.

Summary

List of Figures

List of Tables

Nomenclature

This list presents the definitions of the most important symbols and parameters used in this work. Some symbols are used with different meanings in different contexts, and the symbols are always defined in the text when used.

t	time [s]
x, y	plane cartesian coordinates [m]
St	Strouhal number
M	Mach number
f	frequency [Hz]
D	diameter [m]
U	magnitude of the velocity vector [m/s]
c	speed of sound [m/s]
$\mathbf{u}$	velocity vector [m/s]
p	pressure [Pa]
μ	dynamic viscosity
$\mathbf{x}$	snapshot of the dynamical system
$\mathbf{X}$	matrix of snapshots
r	number of POD or DMD modes used
$\boldsymbol{\varphi}$	POD or DMD mode
a	POD temporal coefficient
$\mathbf{U}$	matrix of left singular vectors
$\mathbf{\Sigma}$	matrix of singular values

σ	singular value
$\mathbf{V}$	matrix of right singular vectors
$\mathbf{A}$	matrix of temporal coefficients (POD) or matrix for the approximated discrete-time linear dynamics of the system (DMD)
Δt	time step between consecutive snapshots or temporal discretization
$\tilde{\mathbf{A}}$	matrix for the reduced order approximated linear system
$\mathbf{\Phi}$	matrix of DMD modes
λ	DMD eigenvalues
ς	DMD growth rate
$\mathbf{b}$	vector of initial coefficients for the DMD modes
Δx	spatial discretization
β_T	visualisation variable
	subscripts and superscripts
∞	reference value
$\overline{a}$	mean value of a
$'$	fluctuation
r	result of truncation with r POD or DMD modes
	Acronyms
SVD	Singular Value Decomposition
DMD	Dynamic Modes Decomposition
POD	Proper Orthogonal Decomposition
VAT	Virtual Aeroacoustic Tunnel
CAALab	Computational Aeroacoustics Laboratory

1 Introduction

The impact of anthropogenic noise on human health is well-known and has motivated many research projects in different fields. In aeroacoustics, the main concern is the noise generated aerodynamically, i.e., by the flow of air past structures. One of the most recognisable subjects of aeroacoustics is the study of noise generated by traditional aircraft. Recent studies have shown that, despite regulatory efforts and technological improvements, aircraft noise remains a relevant health risk factor, especially for people that live close to airports. An analysis of nearly 25 thousand cardiovascular disease deaths that happened close to the Zurich airport, in Switzerland, between 2000 and 2015, by Saucy et al. (2020), indicated a relevant increase in mortality at night after exposure to high sound levels, associated with aircraft flyovers. The adverse health impacts of aircraft noise have also been described by Seidler et al. (2018). They analysed health data, from 2006 to 2010, from over 1 million people living close to the Frankfurt airport in Germany. The study indicated a 7% higher risk of stroke when compared to people living in similar but quieter neighbourhoods.

The negative effects of noise exposure on human health, however, are not exclusively related to aircraft. The same study by Seidler et al. (2018) also identified an increased risk of stroke due to exposure to noise from road and railway traffic. Even though some of the noise from these sources is not caused by the flow, important aeroacoustic effects are present in both cases. The aeroacoustics of railway vehicles, in particular of high-speed trains, has been studied by King III (1996) and Raghunathan, Kim e Setoguchi (2002), for example. The aeroacoustic noise in road vehicles has also been widely described. Vanherpe, Duarte e Lafon (2012) studied the effects of the flow around a car on the interior noise. Alenius (2012) studied the compressible flow through an orifice plate, as a simplified model for a turbocharger compressor. Pallas et al. (2016) investigated the noise generated by electric vehicles, motivated by the fact that in the absence of the internal combustion engine, other noise sources, including the flow, are more relevant. Chen, Hwang e Tsou (2021) studied the health effects of wind turbine noise. The authors determined that exposure to the low-frequency noise from the wind turbines caused variations in heart rate.

There is also growing concern about the impacts of noise from human activities on wildlife. Teff-Seker et al. (2022) described a series of effects of wind turbine noise on

wildlife, such as physiological damage, habitat loss, compromised communication, etc. Felli, Grizzi e Falchi (2013) studied the noise from the propeller-ruder system in ships and highlighted that ship noise can be a problem not only to the crew and passengers but also to marine animals.

Besides the problem with noise, the aviation industry is also under intense pressure to reduce carbon emissions. This led the International Air Transport Association (AITA) to adopt a goal of achieving net zero emissions by 2025 (IATA, 2021). Even though most of this goal is planned to be achieved through sustainable aviation fuel and carbon offsets, new technologies are set to play an important part in this mission. This motivated, for example, Embraer's new family of concept designs for sustainable aircraft (EMBRAER, 2022). All these concepts have open rotors as the propulsion system, and one uses contra-rotating propellers. These models present challenges in noise mitigation, as one of the most important strategies used in turbofans, the acoustic liners positioned in the interior of the nacelle (TAM; JU; WALKER, 2008), cannot be used. In addition to that, contra-rotating propellers are known to be loud noise sources (MONGEAU; HUFF; TESTER, 2013), (TORIJA; CHAITANYA; LI, 2021).

1.1 Computational Aeroacoustics

The majority of modern computational aeroacoustic studies are based on two distinct strategies that can be adequately applied to many cases. One possible method is Direct Noise Computation (DNC), which consists of solving the governing equations of the fluid flow to describe directly the propagation of sound. This approach usually involves solving the Euler Equations or, more commonly, the Navier-Stokes Equations with Large Eddy Simulation methods and requires good spatial and temporal resolution to properly capture sound propagation. There is also a need for low levels of numerical noise, as the acoustic fluctuations are usually much smaller than the aerodynamic. As a consequence, DNC usually has a high computational cost. The other possibility is to use linear equations such as the wave equation or linearized governing equations, such as the Linearized Navier-Stokes Equations, to describe the propagation of sound from a known initial state. Even though this strategy has a much smaller computational cost, it involves simplifying hypotheses that are not always satisfied.

An interesting alternative to these methods might be the use of Data-Based Models of the system of interest. Some particularly interesting methods are the Proper Orthogonal Decomposition (POD) and the Dynamic Modes Decomposition (DMD). These are data-driven methods that use evaluations, also called snapshots, of the system to identify coherent structures. The POD is a more classic method widely used in the study of turbulence, originally proposed by Lumley (1967), to extract orthogonal modes (POD modes) with associated kinetic energy contents. The DMD is a more recent method

originally presented by Schmid e Sesterhenn (2008) and Schmid (2010) for the modal decomposition of a data set that represents a dynamical system. The DMD identifies coherent structures, called dynamic modes, with associated frequencies and growth or decay rates. The POD and DMD modes provide valuable information about the dynamic systems and have been used, for example, to identify noise sources, shock-boundary layer interaction modes, and transonic buffet in wings, among other flow structures. The modes provided by the POD and DMD can also be used to build Reduced-Order Models when combined with other methods, but this is beyond the scope of this work.

1.2 Objectives

The objective of this work is to investigate the transonic flow past a 2D circular cylinder with the POD and DMD methods. The specific objectives are:

1. Identify flow structures and noise sources through the POD and DMD modes and the DMD frequencies;
2. Reconstruct the flow with the POD and DMD modes.

This work will contribute to the description of the noise generated in the transonic flow past a cylinder due to the detachment of the shock waves that appear at its upper and lower sides. Even though this flow has been the subject of several numerical and experimental works, and this phenomenon has been observed experimentally before, it does not appear to have been studied in detail yet. Another contribution of this work is a detailed description of the POD and DMD methods with the practical aspects and challenges faced during implementation and application. This might help to guide future works that use these methods for different problems.

1.3 Methodology

From the specific objectives presented in the previous section, we can define the method adopted in the present work. The object of study will be the transonic flow past a 2D circular cylinder. This case was chosen because the flow past the cylinder is one of the most classical problems in fluid mechanics and is well understood, even for transonic flows. The flow presents rich dynamics, with a von Karman vortex street, shock waves and an acoustic field. The complexity of the flow depends on the Mach number, which offers an opportunity to investigate how the decomposition methods provide information on different cases.

We chose to model the flow with the compressible Euler equations because they allow for the flow to be solved on a large domain with a uniform computational grid

capable of capturing the acoustic and vortical structures without the need to describe the boundary layer or deal with turbulence through RANS or LES methods. In addition to that, we chose to use the Virtual Aeroacoustic Tunnel (VAT) code to solve the equations. This code is the implementation of a very robust and tested numerical method developed in-house at the Computational Aeroacoustics Laboratory at the University of Brasilia.

The POD and DMD methods were implemented in the FORTRAN language and were applied to pressure field snapshots generated from the VAT code. The POD method was chosen for the analysis because it is a classic tool widely used in turbulence and aeroacoustics to identify flow structures and noise sources. The DMD was used because it is a newer tool, with the potential of bringing gains of interpretation, as it provides flow structures associated with specific frequencies.

In summary, the methodology of this work consists in:

- Solve the transonic flow past a circular cylinder, modelled with the Euler Equations for a compressible flow, using a finite volumes discretization combined with an immersed boundary method implemented in the VAT code;
- Analyse the simulation results with the conventional strategies used in computational aeroacoustics, such as the observation of pressure signals, visualisation of the flow with different properties, spectral analysis with the Fast Fourier Transform and calculation of the Sound Pressure Level;
- Implement the POD and DMD methods;
- Apply the POD and DMD methods to the results of the simulation of the transonic flow around a cylinder.

The following section, presents the organisation of the dissertation to follow the proposed methodology.

1.4 Organization of the dissertation

This dissertation is organised into 5 chapters, including this introduction. Chapter 2 presents the theoretical foundations of this work and a brief review of some relevant works about the flow past the circular cylinder and the POD and DMD methods. Chapter 3 presents the work methodology. First, it presents the governing equations and the numerical method used for the simulations of the flow. It also details how the numerical simulations were performed and describes the decomposition methods as they were implemented, as well as some practical aspects and challenges faced during the analyses. Chapter 4 presents the results of the work. In addition to the analysis of the flow, it presents the modal decomposition with POD and DMD, with the interpretation of the modes and the

flow reconstructions. At last, chapter 5 brings the conclusions of the research and some recommendations for future works.

1.5 Publication as a result of this work

Part of the research presented in this work was presented at the XIX International Symposium on Dynamic Problems in Mechanics - DINAME 2023, and published in the conference proceedings with the title "Dynamic Modes Decomposition of The Transonic Flow Around a Cylinder", <dx.doi.org/10.26678/ABCM.DINAME2023.DIN2023-0118>.

2 Fundamentals and Bibliographic Review

2.1 Flow around the cylinder

The flow around the circular cylinder is a classical problem in the study of fluid mechanics. In the eighteenth century, D'Alembert used potential theory to solve the flow of an inviscid, incompressible fluid around a cylinder and obtained the result that the drag was null. He observed that his own results were not compatible with observations of real flows, an inconsistency that became known as D'Alembert's Paradox. In the nineteenth century, Strouhal studied how wires emitted sound due to wind. For his contributions to the study of periodic flows, the Strouhal number, a non-dimensional parameter associated with the flow frequency, was named after him. For the flow around a cylinder, the Strouhal number is defined as

$$St = \frac{fD}{U_\infty}, \tag{2.1}$$

where f is the frequency, D is the diameter of the cylinder and U_∞ is the velocity of the undisturbed flow A well-known result is that the Strouhal number for the flow past a cylinder is around 0.2 for a wide range of Reynolds and Mach numbers. In 1904, Prandtl finally solved D'Alembert's Paradox by describing the boundary layer, a small region near the surface of an object where viscous effects are important, and its separation due to adverse pressure gradients. In 1912, von Karman explained how instabilities cause a periodic emission of vortices in the wake of the cylinder. The vortex street also became known as the von Karman vortex street (WHITE, 2016; ANDERSON, 2017).

After World War II, the interest in compressible flows grew significantly, and the transonic and supersonic flows around cylinders became the subject of many numerical and experimental studies. For these flows, the important parameter is the Mach number, M, defined as

$$M = \frac{U}{c}, \tag{2.2}$$

where U is the flow velocity and c is the local speed of sound. Gowen e Perkins (1952) used transonic and supersonic wind tunnels to study the flow over a cylinder for a wide range of Mach numbers. For transonic flows, the authors observed shock waves formed

alternately on the upper and lower sides of the cylinder with an associated oscillation of the vortex street. They also observed, through Schlieren photography, compression waves propagating upwind from the cylinder, for a Mach number of $M_\infty = 0.51$.

Rodriguez (1984) performed experiments for the flow around a cylinder with Mach numbers of 0.4, 0.55, 0.75 and 0.85. The author observed the periodic shedding of vortices, with a Strouhal number of approximately 0.2, mostly independent of the Mach number.

The inviscid transonic flow around the cylinder has also been the subject of several numerical studies. Buning e Steger (1982) developed a numerical method to solve the two-dimensional Euler equations with an implicit finite differences method with body-conforming coordinates to describe arbitrary geometries. The authors applied their method to the flow around a circular cylinder with $M_\infty = 0.5$ and the results showed an unsteady oscillation. Hughes e Tezduyar (1984) presented a finite element method capable of capturing discontinuities in the solution of the compressible Euler equations and used the flow around a cylinder with a Mach number of 0.5 as a test case. The results showed periodic and alternating vortex shedding and oscillating shock waves in the top and bottom of the cylinder. Pandolfi e Larocca (1989) also used a numerical method to solve the inviscid transonic flow around a cylinder with Mach numbers of 0.5 and 0.6 and observed the periodic shedding of vortices.

Botta (1995) presents an overview of the results for the inviscid transonic flow around a cylinder, based on previous works. The author used a finite volumes method to solve the compressible Euler equations, to study the transonic flow around a cylinder. The author describes some critical Mach numbers that define ranges with particular flow dynamics. For a reference Mach number (M_∞) of about 0.38, the flow becomes transonic, i.e., the maximum velocity, at the extremities of the cylinder, reaches $M = 1.0$. However, the flow remains symmetric as the Mach number grows, until it reaches $M_\infty = 0.5$. At this value, the periodic vortex shedding begins, associated with the oscillation of shock waves on the upper and lower surfaces. The resulting vortex street is very similar to the one obtained for the viscous incompressible flow. Around $M_\infty = 0.6$, the author described a transition from periodic to chaotic flow. The last critical Mach number observed was around $M_\infty = 0.9$. At this point, the flow shifts to what the author calls a "quasi-periodic state, whit high-frequency and low amplitude oscillations". The calculated Strouhal numbers were around 0.2 for $0.5 \leq M_\infty < 0.9$, and increased to 0.4 for $M_\infty \geq 0.9$.

Miserda e Leal (2006) used a finite volumes method to perform a Detached Eddy Simulation of the flow around a cylinder with $M_\infty = 0.8$. Through an analysis of the lift and drag coefficients, the authors observed a chaotic behaviour of the flow and obtained a Strouhal number of 0.18. The flow visualisation also highlighted the association between the shock waves and the boundary layer separation.

Xu, Chen e Lu (2009a) and Xu, Chen e Lu (2009b) used detached eddy simulations to investigate the transonic flow around a cylinder with a Mach number range of 0.85 to

0.98, and also observed the critical value of $M_\infty = 0.9$ described by Botta (1995). For $M_\infty < 0.9$, the flow was unsteady and oscillating shock waves interacted with the turbulent flow. For $M_\infty > 0.9$, on the other hand, the flow was described as "quasi-steady", with stationary shock waves.

Xu, Chen e Lu (2010) used Large Eddy Simulation to study the flow around a cylinder with $M_\infty = 0.75$. Their results also show the interaction between the oscillating shock waves and the detached vortices and a Strouhal number of 0.19.

The interest in the compressible flow around a cylinder goes beyond the transonic cases presented before. Takahashi, Nonomura e Fukuda (2014) developed a numerical method based on the immersed boundary method to solve the compressible turbulent flows with gas-particle interaction, and used the flow around a circular cylinder as a form of verification. They used Mach numbers equal to 0.3, 1,2 and 2.0. The authors were also able to simulate the flow due to the movement of two cylinders in opposite directions at $M_\infty = 1.2$. Maier e Kronbichler (2021) used the supersonic flow with $M_\infty = 3.0$ around a 3D circular cylinder to test a parallel implementation of a finite element method to solve the Euler equations.

These works are just a small list of examples of how the flow around a cylinder is an interesting and relevant problem. Because it has been widely studied, the dynamics of the flow are well understood, which makes it an interesting problem on which to test new methods and analysis tools. That is the reason the flow around a cylinder was chosen as the subject of this work.

2.1.1 Comment on Flow Separation

Before moving on to the decomposition methods, it is important to explain the flow separation, especially when the flow is modelled with the Euler equations, as in the present work.

In real flows, and models that include viscous effects, the first layer of fluid adheres to the solid surface, in what is called the no-slip condition. The flow velocity then increases in a region of the flow called the boundary layer, depicted schematically in figure 2.1 at position x_0. Outside the boundary layer, the viscous effects are usually neglected, and the effects of the wall friction are no longer perceptible. The velocity profile established in the boundary layer ($u(y)$ in figure 2.1) causes a momentum deficit, i.e. the total momentum of the fluid in this region is smaller than it would be if the velocity were uniform and equal to that outside the boundary layer (U). From a closer inspection of the Navier-Stokes equation,

$$\frac{D\rho\mathbf{u}}{Dt} = -\nabla p + \mu\nabla^2\mathbf{u} + \frac{1}{3}\mu\nabla\left(\nabla\cdot\mathbf{u}\right), \tag{2.3}$$

where ρ is the density, $\mathbf{u}$ is the velocity vector, p is the pressure and μ is the dynamic viscosity of the fluid, we can see clearly that the effect of the adverse pressure gradient ∇p

is to reduce the linear momentum $\rho\mathbf{u}$. Due to the momentum deficit, this effect can stop the flow in the boundary layer and even reverse its direction, as shown in figure 2.1. When it happens, the boundary layer is said to have separated and from this point, the vorticity is no longer restricted to a region close to the solid surface (WHITE, 2016).

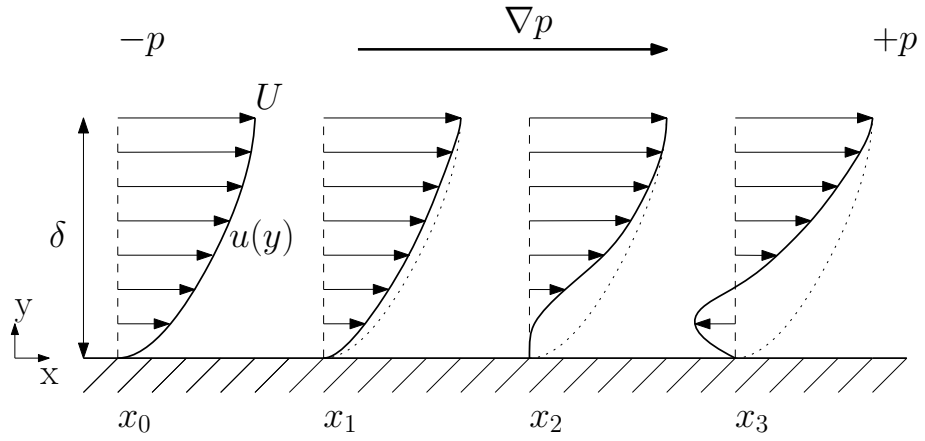

Figura 2.1 – Schematic representation of the boundary layer separation. The dashed line represents the initial velocity profile.

When the flow is modelled with the Euler equations, disregarding the viscous effects, the flow near solid surfaces is significantly different. The solution method used in this work uses a boundary condition of full slip and imposes $\partial u/\partial y = 0$ at the surface, which means that the tangential velocity of the fluid in contact with the wall is not zero and is uniform in the normal direction, as shown in figure 2.2 at position x_0, which means that there is no linear momentum deficit. If we make $\mu = 0$ in equation 2.3, we get the Euler equation, and we see that the adverse pressure gradient has the same effect of reducing the momentum $\rho\mathbf{u}$ but, because there is no momentum deficit, the pressure gradient associated with the geometry of the flow might not separate the flow, as shown in figure 2.2, even if it would cause separation of the boundary layer.

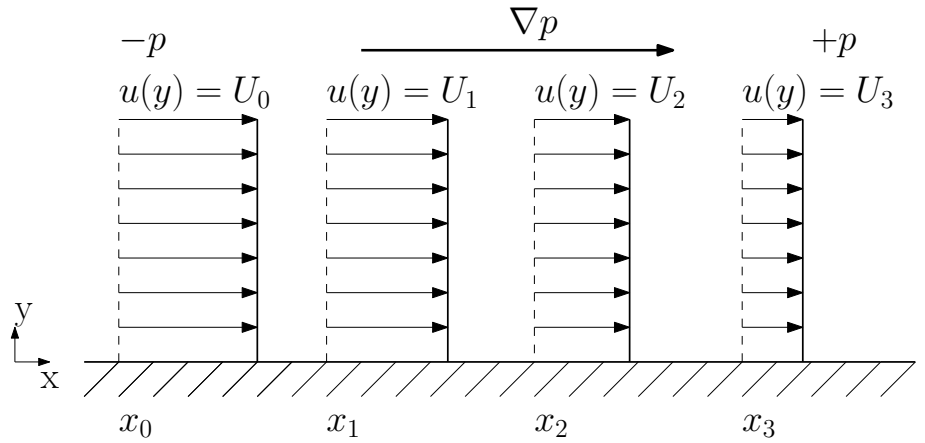

Figura 2.2 – Schematic representation of the effect of the adverse pressure gradient on the flow near a surface, modelled with the Euler equations.

Figure 2.3 shows how the shock wave contributes separation of transonic flows. The shock wave, represented by the red vertical line, compresses the flow and the additional adverse pressure gradient established through the shock, $p_2 - p_1$, causes the flow separation, marked by the change in the direction of the flow in the position x_3', after the shock wave. This is the separation mechanism observed in the cases studied in this work.

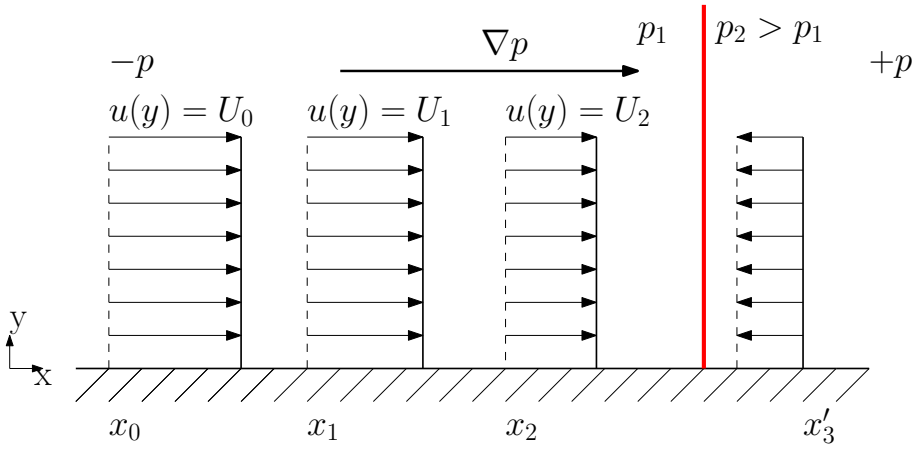

Figura 2.3 – Schematic representation of the effect of the adverse pressure gradient and shock wave on the flow near a surface, modelled with the Euler equations. The red line represents the shock wave.

2.2 Proper Orthogonal Decomposition

The Proper Orthogonal Decomposition (POD) is a statistical method used to extract coherent structures, or modes, from a data set that originates from experiments or numerical simulations. This method was first used to study fluid dynamics and, in particular, turbulence, by Lumley (1967), but it is used in different areas. In the field of signal processing, for example, this method is also referred to as the Karhunen-Loeve Transform (KLT), and in statistics it is called Principal Component Analysis (PCA) (GERBRANDS, 1981).

Berkooz, Holmes e Lumley (1993) present an overview of the POD method, in particular, applied to turbulence. As the authors explain, the POD method comes from an optimisation problem that, given a data set $\mathbf{X}_{n\times m}$, formed by the combination of m evaluations $\mathbf{x}_k$, $k = 1, 2, ..., m$, of an n-dimensional system of interest, with $n \gg m$, aims to find the vector basis $\boldsymbol{\varphi}_k$ that results in the best approximation of the data $\mathbf{x}_k^r$, given by

$$\mathbf{x}_k^r = \sum_{i=1}^{r} \boldsymbol{\varphi}_i a_{i,k}, \tag{2.4}$$

where where $a_{i,k}$ is a temporal coefficient associated with the mode $\boldsymbol{\varphi}_i$ and the snapshot $\mathbf{x}_k$ and $r < m$ is the rank of the approximation. This optimisation problem can be written

as

$$\frac{\max_{\theta} < \mathbf{x}, \boldsymbol{\theta} >}{< \boldsymbol{\theta}, \boldsymbol{\theta} >} = \frac{< \boldsymbol{x_k}, \boldsymbol{\varphi} >}{< \boldsymbol{\varphi}, \boldsymbol{\varphi} >}, \tag{2.5}$$

where $\boldsymbol{\theta}$ is the variable to be optimised.

Sirovich (1987) demonstrated that the eigenvectors of the correlation matrix $\mathbf{C}$ of the data set $\mathbf{X}$,

$$\mathbf{C} = \mathbf{X}\mathbf{X}^{\mathbf{T}}, \tag{2.6}$$

are a solution to the optimisation problem. This is the Method of Snapshots for the calculation of the POD modes $\boldsymbol{\varphi}_k$, also explained in detail by Holmes et al. (2012). The original data can then be written exactly as a function of the POD modes by setting $r = m$ in equation 2.4,

$$\mathbf{x}_k = \sum_{i=1}^{m} \boldsymbol{\varphi_i} a_{i,k}. \tag{2.7}$$

From this method, comes an interesting interpretation of the POD modes, as highlighted by Weiss (2019). If the POD modes are arranged according to the respective eigenvalues ordered from largest to smallest, the first mode can be understood as the direction, in an n-dimensional space, in which the variance of the data is maximum. The second mode, then, is the direction in this space in which the variance is maximum while being orthogonal to the first mode. In general, the ith mode is the direction with the maximum variance that is also orthogonal to the previous $i - 1$ modes.

In this work, the Singular Value Decomposition (SVD) of the data matrix $\mathbf{X}$,

$$\mathbf{X} = \mathbf{U}\boldsymbol{\Sigma}\mathbf{V}^T, \tag{2.8}$$

was used as a simple algorithm to extract the POD modes because, from the definition of the SVD, the columns of matrix $\mathbf{U}$, called the left singular vectors, are the eigenvectors of $\mathbf{X}\mathbf{X}^T$, i.e., the columns of $\mathbf{U}$ are the POD modes. Furthermore, the columns of $\mathbf{V}$, the right singular vectors, are the eigenvectors of $\mathbf{X}^T\mathbf{X}$ and the terms of the diagonal matrix $\boldsymbol{\Sigma}$, the singular values, are the square roots of the eigenvalues of $\mathbf{X}\mathbf{X}^T$ and $\mathbf{X}^T\mathbf{X}$.

Weiss (2019) mentions that, even though the SVD makes the algorithm for calculating the Proper Orthogonal Decomposition simpler, it may be computationally faster, for certain data sets, to build the correlation matrix $\mathbf{C} = \mathbf{X}\mathbf{X}^{\mathbf{T}}$ and calculate its eigendecomposition. It might be worth, in future works, to investigate which method is better for the present case. The choice of using the SVD method in this work was based on the fact that there are several optimised functions in the LAPACK library that calculate the SVD of a matrix and, in particular, the function used calculates only the first r columns of $\mathbf{U}$, the first r terms of $\boldsymbol{\Sigma}$ and the first r lines of $\mathbf{V}^T$. The advantage of this is that only the most relevant modes are calculated and used in the truncated sum at equation 2.4.

If $\mathbf{U}^r$ is a matrix whose columns are the r first POD modes, we can define a POD reconstruction of the data set with reduced order as

$$\mathbf{X}^r = \mathbf{U}^r\mathbf{A}, \tag{2.9}$$

where the matrix $\mathbf{A}$ of the temporal coefficients can be calculated as

$$\mathbf{A} = (\mathbf{U}^r)^T \mathbf{X}, \tag{2.10}$$

taking advantage of the propriety of the orthogonality of the POD modes, $(\mathbf{U}^r)^T = (\mathbf{U}^r)^{-1}$.

2.3 Applications of the Proper Orthogonal Decomposition

Thomas, Dowell e Hall (2003) used a POD-based Reduced Order Model (ROM) to study the aeroelasticity of a 3D wing in an inviscid transonic flow in the frequency domain. The authors created accurate models for the flutter of the wing and showed that different structural configurations can be studied with the same basic set of snapshots and specific mode shapes can be obtained by simply adding the adequate snapshots at the extremities of the frequency range.

Trindade, Wolter e Sampaio (2005) studied the dynamics of a vertical beam subjected to impacts with an outer cylinder due to oscillations through a non-linear finite elements model. The results from the simulation were analysed with the proper orthogonal decomposition. The authors concluded that a non-linear axial-bending coupling model is necessary to properly represent the dynamics of the structure, and they were able to reconstruct the dynamics with 15 POD modes.

Bellizzi e Sampaio (2006) calculated the POD of the responses of linear and non-linear dynamic systems subjected to random excitations through the Karhunen-Loeve expansion, and the results were compatible with the classical POD method.

Violato e Scarano (2013) used POD to decompose experimental data of a 3D jet obtained with particle image velocimetry (PIV). The POD modes highlighted certain vortex structures and allowed for the characterisation of aeroacoustic sources.

Lui e Wolf (2019) used a variation of the POD called spectral proper orthogonal decomposition, combined with neural networks, to build a ROM. This ROM was applied to the compressible flow past a cylinder and to the flow around a stalled airfoil. The method captured the leading edge and trailing edge vortices accurately even beyond the training window.

Ricciardi et al. (2021) used the POD method to analyse the results from a simulation of the flow past a realistic landing gear. With the POD modes, the authors were able to identify how different structures contribute to sound generation.

The POD was also used by Xu et al. (2022), combined with different machine learning algorithms, to build Reduced Order Models. These models were then applied to the low Reynolds flow around a cylinder and to the transonic flow in an airfoil. The authors compared the predictions to the numerical solutions and were able to select the best algorithms.

Tang, Li e Wei (2023) used the POD to study features of the transonic flow over a hemisphere. With the decomposition, they were able to identify that the most relevant aspects of the flow were lateral and wall-normal oscillations.

These works show how the POD is a very useful tool for the analysis of fluid flows. The POD modes often assist in the identification of dominant structures and sound sources in a flow. The decomposition is also often used as the basis of reduced order models for the fluid flow, in combination with machine learning methods.

2.4 Dynamic Modes Decomposition

The Dynamic Modes Decomposition (DMD), introduced by Schmid (2010), is a data-driven method used to extract coherent space-time structures, called dynamic modes, from the results of numerical simulations or experiments. Mathematically, the DMD consists of the computation of eigenvalues and eigenvectors of a finite-dimensional approximation to the linear, infinite-dimensional Koopman operator that describes a non-linear, finite-dimensional dynamical system. An advantage of the DMD is that it does not depend on a previous model of the system and is applied directly to variables that describe the state of the system of interest.

The DMD algorithm presented here was mostly adapted from Kutz et al. (2016), and we kept the same notation for simplicity. The DMD consists initially of registering the state of the flow of interest, either by experiments or numerical simulations, in m different time instants with time step Δt. These states, also called snapshots, are then organised into vectors x_k, $k = 1, 2, ..., m$, that form the columns of two matrices X and $X^{'}$ as

$$\mathbf{X} = \begin{bmatrix} | & | & & | \\ \mathbf{x}_1 & \mathbf{x}_2 & \cdots & \mathbf{x}_{m-1} \\ | & | & & | \end{bmatrix} \tag{2.11}$$

and

$$\mathbf{X}^{'} = \begin{bmatrix} | & | & & | \\ \mathbf{x}_2 & \mathbf{x}_3 & \cdots & \mathbf{x}_{m} \\ | & | & & | \end{bmatrix}. \tag{2.12}$$

If we describe the flow as a generic dynamical system,

$$\frac{d\mathbf{x}}{dt} = f(\mathbf{x}, t), \tag{2.13}$$

i.e., the rate of change of the state $\mathbf{x}$ is a function of time and of the state of the system, we can also write a linear approximation as

$$\frac{d\mathbf{x}}{dt} = \mathcal{A}\mathbf{x}, \tag{2.14}$$

where $\mathcal{A}$ is the matrix for the approximated linear system.

We can then use a simple finite differences discretization to approximate

$$\mathbf{x}_{k+1} \approx \exp(\mathcal{A}\Delta t)\mathbf{x}_k \approx \mathbf{A}\mathbf{x}_k, \tag{2.15}$$

where $\mathbf{A}$ is now the matrix that represents the approximated discrete time, linear dynamics of the system. We can also write this linear approximation in matrix form, using equations 2.11 and 2.12

$$\mathbf{X}^{'} \approx \mathbf{A}\mathbf{X}, \tag{2.16}$$

In order to minimise the error $\left\|\mathbf{X}^{'} - \mathbf{A}\mathbf{X}\right\|_F$, the linear operator $\mathbf{A}$ is given by $\mathbf{A} = \mathbf{X}^{'}\mathbf{X}^{\dagger}$, where $\dagger$ indicates the Moore-Penrose pseudo-inverse matrix of $\mathbf{X}$. We can interpret these equations as a linear regression of the data onto the dynamics described by the linear operator $\mathbf{A}$. The eigenvectors of $\mathbf{A}$ are the dynamic modes, or DMD modes, and the corresponding eigenvalues indicate the frequency and rate of growth or decay of the mode.

However, the matrix $\mathbf{A}$ is of dimension $n \times n$, and n, the size of the snapshots, is generally large, which means it may not be possible to compute the eigendecomposition of $\mathbf{A}$ directly. A more efficient approach is to first calculate the singular value decomposition (SVD) approximation of $\mathbf{X}$ with a reduced order r, given by $\mathbf{X} \approx \mathbf{U}\mathbf{\Sigma}\mathbf{V}^{*}$, where $\mathbf{U}$ and $\mathbf{V}$ are orthogonal matrices of dimensions $n \times r$ and $m \times r$, respectively, $*$ indicates the conjugate transpose and $\mathbf{\Sigma}$ is a diagonal matrix of dimensions $r \times r$. A reduced matrix with dimensions $r \times r$, the projection of $\mathbf{A}$ onto the Proper Orthogonal Decomposition (POD) modes obtained from the SVD, is given by

$$\tilde{\mathbf{A}} = \mathbf{U}^{*}\mathbf{A}\mathbf{U} = \mathbf{U}^{*}\mathbf{X}^{'}\mathbf{V}\mathbf{\Sigma}^{-1}. \tag{2.17}$$

Since $\tilde{\mathbf{A}}$ is of much lower dimension than $\mathbf{A}$, its eigendecomposition can be directly calculated, which results in

$$\tilde{\mathbf{A}}\mathbf{W} = \mathbf{W}\mathbf{\Lambda}, \tag{2.18}$$

where the columns of $\mathbf{W}$ are the eigenvectors of $\tilde{\mathbf{A}}$ and Λ is a diagonal matrix with the eigenvalues. The eigenvectors of $\mathbf{A}$, which are the DMD modes φ_k can be recovered from $\mathbf{W}$ as the columns of the matrix $\mathbf{\Phi}$ given by

$$\mathbf{\Phi} = \mathbf{X}^{'}\mathbf{V}\mathbf{\Sigma}^{-1}\mathbf{W}. \tag{2.19}$$

The terms of matrix $\mathbf{\Lambda}$, λ_k, are the eigenvalues of $\mathbf{A}$. From these eigenvalues, it is possible to calculate the DMD modes' frequencies, f_k, as

$$f_k = \arg(\lambda_k)/2\pi\Delta t \tag{2.20}$$

and rates of growth, ς_k, as

$$\varsigma_k = \mathrm{Re}(\ln(\lambda_k)) \tag{2.21}$$

In principle, it is possible to use the DMD modes to predict the future of the dynamical system by writing the linear combination of the DMD modes weighted by their coefficients $\mathbf{b}$ of initial conditions as

$$\mathbf{x}(t) = \mathbf{\Phi} \exp(\mathbf{\Omega} t)\, \mathbf{b}, \tag{2.22}$$

where $\mathbf{\Omega}$ is a diagonal matrix with $\omega_k = \ln(\lambda_k)/\Delta t$, and $\mathbf{b} = \mathbf{\Phi}^{\dagger}\mathbf{x_1}$, $\dagger$ denotes the pseudo-inverse matrix and $\mathbf{x}_1$ is the initial snapshot.

Given the reduced-order matrix $\tilde{\mathbf{A}}$ and the left singular vectors $\mathbf{U}$ (KUTZ et al., 2016), it is also possible to write

$$\tilde{\mathbf{x}}_{k+1} = \tilde{\mathbf{A}}\tilde{\mathbf{x}}_k, \tag{2.23}$$

which is the reduced-order equation for the equivalent linear system given by Eq. (2.16). Starting from an initial condition $\tilde{\mathbf{x}}_0 = \mathbf{U}^*\mathbf{x}_0$, it is possible to reconstruct the full state $\mathbf{x}_k = \mathbf{U}\tilde{\mathbf{x}}_k$ at any instant $t = k\,\Delta t$ by a series of iterations of Eq. (2.23).

2.5 Applications of the Dynamic Modes Decomposition

2.5.1 General applications to fluid dynamics

In addition to presenting the DMD, Schmid (2010) applied the method to several examples of numerical and experimental results. With the results from the simulation of the flow past an open square cavity, the author showed that it is possible to select only the more relevant parts of the flow to apply the DMD. The results showed that the use of a section of the domain is enough to represent the dynamics of the flow in this case, and there were only small differences in the calculated eigenvalues. Schmid (2010) also applied the DMD successfully to experimental measurements with Particle Image Velocimetry (PIV) of the flows past a flexible membrane and past an array of cylinders.

Schmid et al. (2011) also used the DMD to extract the dynamic modes from Schlieren photographs of a helium jet. The interesting aspect of this example is that the method was applied directly to the images since the Schlieren visualisation technique does not result directly in a measured variable. The authors were also able to use the DMD to extract the dynamic modes of unforced and forced axisymmetric jets, using PIV measurements from experiments.

Bagheri (2013) calculated the Koopman modes for the flow around a circular cylinder and showed that if some conditions are satisfied, the DMD method might provide a good approximation of the Koopman modes.

Although the Dynamic Modes Decomposition method was designed to reduce the computational cost of the process of extracting dynamic modes from data, it may still be reasonably expensive from a computational point of view. If the snapshots used are the

result of high-resolution numerical simulations or experimental measurements, the number of lines n of the matrices from equations 2.11 and 2.12 may be too large for the Singular Value Decomposition to be performed as usual. In addition to that, if the objective is to capture low-frequency phenomena, it is necessary to use a number of snapshots m that may be large enough to make the calculations nonviable. With that in mind, Hemati, Williams e Rowley (2014) developed algorithms that are not only more efficient computationally, but also allow the DMD to be calculated in real-time, as data becomes available from experiments or simulations. The greater computational efficiency is achieved by a POD compression step that reduces the necessary memory storage to compute the method, which allows the DMD to be applied to larger sets of data. Their algorithm also allows the extraction of the dynamic modes from a streaming set of data, which means that it is possible to calculate the modes in real-time, as the experiment or the numerical simulation is conducted.

Sarmast et al. (2014) performed numerical simulations to study the instability of blade tip vortexes on the wake of a horizontal axis wind turbine. The authors analysed the results with DMD and POD methods and were able to observe the dominant modes of the flow in the wake and understand how the unstable modes are associated with the interaction between vortexes of consecutive spirals. With the results for the growth rate of the unstable modes, the authors were able to formulate an analytical model to determine the length of the stable wake based on the turbulence intensity.

Statnikov et al. (2016) used the dynamic modes decomposition to study the 3D wake flow in a backwards-facing step, using data from numerical simulations. The main stable modes identified by the DMD had frequencies that coincided well with the spectra of wall pressure. The DMD modes revealed that the dynamics of the wake is governed by the low-frequency movement of the recirculation bubble and by the high-frequency oscillation of the shear layer. These modes allowed the authors to better understand the results of PIV experiments.

Priebe et al. (2016) were able to use the DMD to study the dynamics of the separation of the boundary layer induced by a shock wave. The DMD modes extracted from the direct numerical simulations of the flow in a compression ramp showed that the unsteadiness of the shock wave is directly associated with the unsteady downstream regions with high and low momentum. The authors used the low-frequency DMD modes to reconstruct the dynamics of the flow, which captured the original dynamics accurately.

Nichols et al. (2017) also used the DMD to study the interaction of shock waves and boundary layers. The DMD modes showed that this interaction results in two simultaneous types of flows. One with a lower frequency associated with the movement of the separation bubble and accompanied by a flapping movement of the reflected shock wave is present, and one with a higher frequency, associated with the propagation of instability waves past the interaction region. The authors also performed a Global Stability Analysis, which revealed weakly stable oscillatory modes, some of which are similar to the low-frequency

DMD mode.

2.5.2 Applications to acoustics and aeroacoustics

In addition to more general applications to the study of fluid dynamics, the DMD has also been widely used in acoustics and aeroacoustics, especially to identify structures in fluid flows responsible for noise generation. Alenius (2012) used the DMD and the POD methods to study the compressible flow through an orifice plate. The author was able to identify the most relevant flow structures and their corresponding frequencies with the DMD but was only able to properly reconstruct the flow with the POD modes, and not with the DMD. This was attributed to the fact that the DMD modes' rates of growth might change with time, an effect that the method does not capture.

Seid et al. (2012) calculated the POD and DMD modes of 2D compressible flows. To compose the snapshots, the authors used both components of the velocity vector and an inner product of the pressure and enthalpy, as they claimed that the inclusion of both thermodynamic and kinematic variables is necessary to properly capture aeroacoustic effects with a reduced order model. Both methods provided relevant information about the structures of the flow, and the authors presented the differences between POD and DMD decompositions. The POD results provided structures associated with aeroacoustic phenomena with multiple frequency components, while the DMD resulted in modes with characteristic frequencies and rates of growth.

The DMD method was also used by Jourdain et al. (2013) to identify acoustic modes and predict damping in a 3D chamber. In order to reduce the computational cost, the authors applied the DMD to the pressure field in two planes inside the chamber, one vertical, in the middle of the chamber, and one horizontal, in the axial direction. The DMD analysis was able to correctly determine the geometrical configuration that optimises the damping of the acoustic modes, in accordance with other methods.

Alenius, Åbom e Fuchs (2015) studied the plane sound waves propagating in a flow past an orifice plate with large eddy simulations, and the results were analysed with the DMD method. The authors were able to observe an increase in acoustic energy as the waves interacted with the flow past the orifice. They also noticed that, for an axisymmetric inflow, there is a feedback mechanism that results in self-sustained instability, which is associated with tonal noise. For a non-axisymmetric inflow, this instability is suppressed.

Nair et al. (2016) also studied the flow past orifice plates with large eddy simulations. The results were post-processed with the DMD to decompose the flow field and, in sequence, the authors performed a Lagrangian analysis and tracked the ridges in the Finite-Time Lyapunov Exponents. This approach resulted in the identification of coherent structures in the flow field, and it was possible to distinguish structures responsible for sound generation from those that are mostly silent. This method is presented as a possible strategy for

the identification of structures associated with large amplitude noise and could assist the design of noise control strategies.

Ali, Pandey e Gregory (2016) performed experiments with an acoustic resonance cavity, using one or two speakers to excite the cavity with different frequencies. The authors used fast-response pressure-sensitive paint (PSP) to measure the pressure field in one of the cavity walls and analysed the results with DMD, POD and phase averaging methods. Even though all methods were able to extract the pressure fields and remove noise, the DMD and the POD were better at analysing aperiodic and multi-frequency signals. In addition to that, the authors concluded that the DMD is better at removing noise and identifying the dominant structures because the POD only extracts spatially orthogonal modes, while the DMD modes can be understood as orthogonal in time.

Frank e Munz (2016) studied, via numerical simulations, the mechanisms of noise generation in automotive side-view mirrors. With the DMD and stability analysis methods, they were able to identify that the noise is generated by acoustic feedback phenomena, and is directly associated with the geometry of the mirror. In particular, the DMD allowed the identification of unstable modes associated with tonal noise generation.

Liu et al. (2018) performed numerical simulations of the transonic flow past an open cavity and used the POD and the DMD methods to study the propagation of sound waves emitted from the cavity. The DMD modes showed the advective transport of pressure patterns and the propagation of sound waves and indicated correctly the presence of the feedback mechanism for sound generation.

Broatch et al. (2019) used the DMD to analyze the acoustic field of a radial compressor. The DMD allowed the understanding of how the spatial features of the flow influence acoustic emissions. Because the DMD is capable of including the entire pressure field in the analysis and does not depend on previous assumptions about the system, it was possible to better characterise the amplitudes for each frequency, when compared to the results from the classical Tyler-Sofrin model for mode propagation in ducts, probably because this model depends on assumptions that are not always valid for radial compressors, especially with complex geometries.

2.6 Variations of the DMD algorithm

The difficulty in using the DMD modes to reconstruct flow fields, such as the one mentioned by Alenius (2012), has motivated research on alternatives to the original DMD algorithm that provide better reconstruction results. Jovanovic, Schmid e Nichols (2014) presented a variation of the DMD called Sparsity-Promoting Dynamic Modes Decomposition. This method uses an optimisation algorithm to select the smallest amount of DMD modes that result in the best approximation of the data set. With this new method, the authors were able to extract the most relevant frequencies and flow structures

from the numerical solutions of a Poiseuille flow and a supersonic jet, as well as from PIV data for a jet passing through two cylinders.

Another variation of the DMD algorithm was presented by Ohmichi (2017). The proposed method consists of preconditioning the input data through a projection on a basis formed with POD modes. This projection significantly reduces the dimension of the data set and consequently the memory cost. To further reduce the memory cost, the authors use an incremental approach, similar to the one by Hemati, Williams e Rowley (2014). Another element of the proposed method is the selection of the most physically relevant DMD modes through the solution of an optimisation problem with greedy algorithms. This method was used by Ohmichi, Ishida e Hashimoto (2018) to study the transonic buffet on a 3d wing.

Anantharamu e Mahesh (2019) also presented a variation of the DMD based on the Arnoldi algorithm for orthogonalization. Their method also uses an incremental approach to save memory and can be parallelised. In addition to that, the authors presented an error analysis that indicates the optimal size of the data set.

A very detailed review of the DMD method and its variants was presented by Schmid (2022).

3 Methods

This chapter brings an overview of the work method adopted in the present work. It starts with the description of the governing equations chosen to model the fluid flow and in sequence presents the numerical method used to solve these equations. After that, it presents the most relevant details of the simulations, such as the layout of the domain, the discretization and the performance. At last, the modal decomposition methods are described and some practical aspects and challenges of the analysis are highlighted.

3.1 Governing Equations

Since the objective of this work is to study the flow around a cylinder with numerical simulations, it is necessary to choose a model to describe the flow of air. The physical principles that govern the flow are the conservation of mass, Newton's second law of motion and the first law of thermodynamics. From these principles, it is possible to obtain different partial differential equations that describe the movement of a fluid, depending on the chosen model for the behaviour of the specific fluid when subjected to a particular flow. In this work, the fluid of interest is air subjected to a compressible flow. Based on that, we write the continuity equation as

$$\frac{\partial \rho}{\partial t} + \nabla \cdot (\rho \mathbf{v}) = 0, \tag{3.1}$$

where ρ is the density of the fluid and $\mathbf{v}$ is the velocity vector.

The momentum equation, based on Newton's second law of motion for a Newtonian fluid that follows Stokes' hypothesis, is the Navier-Stokes equation, which is given by

$$\frac{\partial (\rho \mathbf{v})}{\partial t} + \nabla \cdot (\rho \mathbf{v} \otimes \mathbf{v}) = -\nabla p + \nabla \cdot \left\{ \mu \left[\nabla \mathbf{v} + (\nabla \mathbf{v})^T \right] - \frac{2}{3} \mu (\nabla \cdot \mathbf{v}) \mathbf{I} \right\} + \rho \mathbf{f}, \tag{3.2}$$

where p is the pressure μ is the dynamic viscosity, $\mathbf{I}$ is the identity tensor and $\mathbf{f}$ is the vector of body forces, and the energy equation, based on the first law of thermodynamics, is given by

$$\frac{\partial (\rho e_T)}{\partial t} + \nabla \cdot (\rho e_T \mathbf{v}) = \kappa \nabla^2 T - \nabla \cdot (p \mathbf{v}) + \nabla \cdot (\boldsymbol{\tau} \cdot \mathbf{v}) + \rho \mathbf{f} \cdot \mathbf{v}, \tag{3.3}$$

where e_T is the total energy per unit mass, T is the temperature, κ is the thermal conductivity coefficient, and $\boldsymbol{\tau}$ is the deviatoric part of the stress tensor.

Equations 3.1, 3.2 and 3.3 are known as the Navier-Stokes equations for an unsteady compressible flow. They form a system of nonlinear partial differential equations that can only be solved with numerical methods. The adequate solution of these equations, including a turbulent boundary layer, has a very high computational cost. In order to reduce this computational cost, we disregard the viscous and heat conduction terms in the momentum and energy equations. This simplification results in a new system of nonlinear partial differential equations, called the Euler equations for a compressible flow, that can be solved numerically with a much smaller computational cost. The equations that form this system are the continuity equation,

$$\frac{\partial \rho}{\partial t} + \nabla \cdot (\rho \mathbf{v}) = 0, \tag{3.4}$$

the momentum equation,

$$\frac{\partial (\rho \mathbf{v})}{\partial t} + \nabla \cdot (\rho \mathbf{v} \otimes \mathbf{v}) = -\nabla p + \rho \mathbf{f}, \tag{3.5}$$

and the energy equation,

$$\frac{\partial (\rho e_T)}{\partial t} + \nabla \cdot (\rho e_T \mathbf{v}) = -\nabla \cdot (p\mathbf{v}) + \rho \mathbf{f} \cdot \mathbf{v}, \tag{3.6}$$

where the total energy per unit mass is given by the sum of the internal energy, e and the kinetic energy, $(u^2 + v^2)/2$,

$$e_t = e + \frac{u^2 + v^2}{2}, \tag{3.7}$$

and u and v are the velocity components in the x and y directions, respectively.

To complete the system of equations, it is also necessary to use the constitutive equations for an ideal and calorically perfect gas,

$$p = (\gamma - 1)\, \rho\, e \tag{3.8}$$

and

$$T = \frac{\gamma M_\infty^2 p}{\rho}, \tag{3.9}$$

where the reference Mach number, M_∞ is

$$M_\infty = \frac{U_\infty}{\sqrt{\gamma R T_\infty}}, \tag{3.10}$$

and $\gamma = c_p/c_v$ is the ratio of the specific heats at constant pressure and constant volume. Note that equation 3.8 establishes the density as a function of both the pressure and the temperature (as $e = c_v T$). This results in a misalignment of the pressure and density gradients that generates vorticity and is called the baroclinic mechanism (HOLTON; HAKIM, 2013).

These equations have been written in the non-dimensional form suggested by Anderson, Tannehill e Pletcher (1997), with the non-dimensional variables given by

$$x = \frac{x^*}{L} \quad y = \frac{y^*}{L} \quad u = \frac{u^*}{U_\infty} \quad v = \frac{v^*}{U_\infty} \quad t = \frac{t^*}{L/U_\infty} \quad \rho = \frac{\rho^*}{\rho_\infty}$$

$$p = \frac{p^*}{\rho_\infty U_\infty^2} \quad e = \frac{e^*}{U_\infty^2} \quad T = \frac{T^*}{T_\infty} \quad f = \frac{f^*}{\rho_\infty U_\infty^2 L}$$

where L is the reference length, U_∞ is the dimensional reference velocity, the other terms with the subscript ∞ are the dimensional properties of the undisturbed flow and the terms with the superscript $*$ are the dimensional variables.

3.2 Numerical Method

To solve the Euler equations numerically, it is convenient to write them in the vector form suggested by Anderson, Tannehill e Pletcher (1997),

$$\frac{\partial \mathbf{U}}{\partial t} + \frac{\partial \mathbf{E}}{\partial x} + \frac{\partial \mathbf{F}}{\partial y} = \mathbf{R}, \tag{3.12}$$

for a two-dimensional flow, where

$$\mathbf{U} = \begin{bmatrix} \rho \\ \rho\, u \\ \rho\, v \\ \rho\, e_t \end{bmatrix} \tag{3.13}$$

is the vector of the conservative properties,

$$\mathbf{E} = \begin{bmatrix} \rho\, u \\ \rho\, u\, u + p \\ \rho\, u\, v \\ (\rho\, e_t + p)\, u \end{bmatrix} \tag{3.14}$$

and

$$\mathbf{F} = \begin{bmatrix} \rho\, v \\ \rho\, u\, v \\ \rho\, v\, v + p \\ (\rho\, e_t + p)\, v \end{bmatrix} \tag{3.15}$$

are the flux vectors in the x and in the y directions, respectively.

$$\mathbf{R} = \begin{bmatrix} 0 \\ f_x \\ f_y \\ f_x\, u + f_y\, v \end{bmatrix} \tag{3.16}$$

is the vector of pseudo-forces and pseudo-works used to accelerate the flow from the stagnation condition to the desired condition.

The second and third terms in the left side of equation 3.12 can be written as the divergent of a second-order tensor, $\mathbf{\Pi}$, defined as

$$\mathbf{\Pi} = \mathbf{E} \otimes \mathbf{i} + \mathbf{F} \otimes \mathbf{j}, \tag{3.17}$$

where **i** and **j** are the base vectors of the coordinates system. The system of governing equations can thus be written in the vector form as

$$\frac{\partial \mathbf{U}}{\partial t} + \nabla \cdot \mathbf{\Pi} = \mathbf{R}. \tag{3.18}$$

3.2.1 Finite Volumes Discretization

To numerically solve the system of equations given by equation 3.18, it is necessary to integrate it in a finite control volume V and apply the divergence theorem to the second term on the left side, which results in

$$\frac{\partial}{\partial t}\int_V \mathbf{U} dV + \int_S (\mathbf{\Pi} \cdot \mathbf{n})\, dS = \int_V \mathbf{R} dV. \tag{3.19}$$

Defining the volumetric mean of conservative properties vector as

$$\overline{\mathbf{U}} \equiv \frac{1}{V}\int_V \mathbf{U} dV, \tag{3.20}$$

and the volumetric mean of the pseudo forces and pseudo work vector as

$$\overline{\mathbf{R}} \equiv \frac{1}{V}\int_V \mathbf{R} dV, \tag{3.21}$$

equation 3.19 can be rewritten as

$$\frac{\partial \overline{\mathbf{U}}}{\partial t} = -\frac{1}{V}\int_S (\mathbf{\Pi} \cdot \mathbf{n})\, dS + \overline{\mathbf{R}}. \tag{3.22}$$

Considering the tensor $\mathbf{\Pi}$ constant over the surfaces of the control volume and approximating the temporal derivative as the ratio of finite differences, it is possible to write an approximation of equation 3.22 with discrete time and finite volumes as

$$\frac{\Delta \overline{\mathbf{U}}_{i,j}}{\Delta t} = -\frac{1}{V_{i,j}}\left[(\mathbf{\Pi} \cdot \mathbf{S})_{i+\frac{1}{2}} + (\mathbf{\Pi} \cdot \mathbf{S})_{i-\frac{1}{2}} + (\mathbf{\Pi} \cdot \mathbf{S})_{j+\frac{1}{2}} + (\mathbf{\Pi} \cdot \mathbf{S})_{j-\frac{1}{2}}\right]. \tag{3.23}$$

On equation 3.23, $\mathbf{S}_{i+\frac{1}{2}}$, $\mathbf{S}_{i-\frac{1}{2}}$, $\mathbf{S}_{j+\frac{1}{2}}$ and $\mathbf{S}_{j-\frac{1}{2}}$ are the normal unit vectors associated with the surfaces of the control volumes. $\mathbf{S}_{i+\frac{1}{2}}$ corresponds to the surface between control volumes $V_{i,j}$ and $V_{i+1,j}$, $\mathbf{S}_{i-\frac{1}{2}}$ corresponds to the surface between control volumes $V_{i-1,j}$ and $V_{i,j}$. In the same way, $\mathbf{S}_{j+\frac{1}{2}}$ corresponds to the surface between control volumes $V_{i,j}$ and $V_{i,j+1}$ and $\mathbf{S}_{j-\frac{1}{2}}$ corresponds to the surface between control volumes $V_{i,j-1}$ and $V_{i,j}$. The approximation of tensor $\mathbf{\Pi}$ as constant over the control surfaces and of the derivative as the ratio between the difference of conservative variables and the time step are sources of error in the method.

From equation 3.23, we can to define the vector $\mathcal{F}_i$, that represents the net flux of tensor $\mathbf{\Pi}$ through the control surfaces in a time interval Δt, as

$$\mathcal{F}_{i,j} = \frac{\Delta t}{V_{I,j}} \left[(\mathbf{\Pi} \cdot \mathbf{S})_{i+\frac{1}{2}} + (\mathbf{\Pi} \cdot \mathbf{S})_{i-\frac{1}{2}} + (\mathbf{\Pi} \cdot \mathbf{S})_{j+\frac{1}{2}} + (\mathbf{\Pi} \cdot \mathbf{S})_{j-\frac{1}{2}} \right], \tag{3.24}$$

and equation 3.23 can be written as

$$\Delta \overline{\mathbf{U}}_{i,j} = -\mathcal{F}_{i,j}. \tag{3.25}$$

To calculate the flux vector $\mathcal{F}_{i,j}$, it is necessary to determine the properties of the flow on the surfaces of the control volume since, originally, only the mean conservative properties inside the control volume, $\overline{\mathbf{U}}_{i,j}$, are known, and the vector $(\mathbf{\Pi} \cdot \mathbf{S})_{i+\frac{1}{2},j}$, for example, is

$$(\mathbf{\Pi} \cdot \mathbf{S})_{i+\frac{1}{2}} = \begin{bmatrix} (\mathbf{\Pi} \cdot \mathbf{S})_1 \\ (\mathbf{\Pi} \cdot \mathbf{S})_2 \\ (\mathbf{\Pi} \cdot \mathbf{S})_3 \\ (\mathbf{\Pi} \cdot \mathbf{S})_4 \end{bmatrix}_{i+\frac{1}{2}}, \tag{3.26}$$

where the first component is associated with the continuity equation,

$$\left[(\mathbf{\Pi} \cdot \mathbf{S})_1 \right]_{i+\frac{1}{2}} = \rho_{i+\frac{1}{2}} \, (q_s)_{i+\frac{1}{2}}, \tag{3.27}$$

the second and third are associated with the momentum equation,

$$\left[(\mathbf{\Pi} \cdot \mathbf{S})_2 \right]_{i+\frac{1}{2}} = (\rho \, u)_{i+\frac{1}{2}} \, (q_s)_{i+\frac{1}{2}} + p_{i+\frac{1}{2}} \, (s_x)_{i+\frac{1}{2}} \tag{3.28}$$

and

$$\left[(\mathbf{\Pi} \cdot \mathbf{S})_3 \right]_{i+\frac{1}{2}} = (\rho \, v)_{i+\frac{1}{2}} \, (q_s)_{i+\frac{1}{2}} + p_{i+\frac{1}{2}} \, (s_y)_{i+\frac{1}{2}} \tag{3.29}$$

and the fourth component is associated with the energy equation,

$$\left[(\mathbf{\Pi} \cdot \mathbf{S})_4 \right]_{i+\frac{1}{2}} = (\rho \, e_T)_{i+\frac{1}{2}} \, (q_s)_{i+\frac{1}{2}} + p_{i+\frac{1}{2}} \, (q_s)_{i+\frac{1}{2}}, \tag{3.30}$$

where

$$(q_s) = u_{i+\frac{1}{2}} \, (s_x)_{i+\frac{1}{2}} + v_{i+\frac{1}{2}} \, (s_y)_{i+\frac{1}{2}} \tag{3.31}$$

is the volumetric flux through surface $\mathbf{S} = [s_x, s_y]$ between volumes V_i e V_{i+1}. The index j has been omitted from these equations for simplicity.

3.2.2 Surface Interpolation Scheme

As equations 3.27, 3.28, 3.29, 3.30 e 3.31 show, it is necessary to determine the values of the conservative properties, (ρ, $\rho \, u$, $\rho \, v$ and $\rho \, e_T$) and of the primitive properties

(u, v and p) over the surfaces of the control volumes. For this, the fourth-order, non-amplifying interpolation scheme proposed by Pimenta (2016) will be used. The properties over surface $S_{i+\frac{1}{2},j}$ for example, are given by

$$\rho_{i+\frac{1}{2},j} = \frac{9}{16}\left(\overline{\rho}_{i,j} + \overline{\rho}_{i+1,j}\right) - \frac{1}{16}\left(\overline{\rho}_{i-1,j} + \overline{\rho}_{i+2,j}\right), \tag{3.32a}$$

$$(\rho\, u)_{i+\frac{1}{2},j} = \frac{9}{16}\left(\overline{\rho u}_{i,j} + \overline{\rho u}_{i+1,j}\right) - \frac{1}{16}\left(\overline{\rho u}_{i-1,j} + \overline{\rho u}_{i+2,j}\right), \tag{3.32b}$$

$$(\rho\, v)_{i+\frac{1}{2},j} = \frac{9}{16}\left(\overline{\rho v}_{i,j} + \overline{\rho v}_{i+1,j}\right) - \frac{1}{16}\left(\overline{\rho v}_{i-1,j} + \overline{\rho v}_{i+2,j}\right) \tag{3.32c}$$

and

$$(\rho\, e_T)_{i+\frac{1}{2},j} = \frac{9}{16}\left(\overline{\rho e_T}_{i,j} + \overline{\rho e_T}_{i+1,j}\right) - \frac{1}{16}\left(\overline{\rho e_T}_{i-1,j} + \overline{\rho e_T}_{i+2,j}\right), \tag{3.32d}$$

and the properties over surface $S_{i-\frac{1}{2},j}$ are given by

$$\rho_{i-\frac{1}{2},j} = \frac{9}{16}\left(\overline{\rho}_{i,j} + \overline{\rho}_{i-1,j}\right) - \frac{1}{16}\left(\overline{\rho}_{i-2,j} + \overline{\rho}_{i+1,j}\right), \tag{3.33a}$$

$$(\rho\, u)_{i-\frac{1}{2},j} = \frac{9}{16}\left(\overline{\rho u}_{i,j} + \overline{\rho u}_{i-1,j}\right) - \frac{1}{16}\left(\overline{\rho u}_{i-2,j} + \overline{\rho u}_{i+1,j}\right), \tag{3.33b}$$

$$(\rho\, v)_{i-\frac{1}{2},j} = \frac{9}{16}\left(\overline{\rho v}_{i,j} + \overline{\rho v}_{i-1,j}\right) - \frac{1}{16}\left(\overline{\rho v}_{i-2,j} + \overline{\rho v}_{i+1,j}\right) \tag{3.33c}$$

and

$$(\rho\, e_T)_{i-\frac{1}{2},j} = \frac{9}{16}\left(\overline{\rho e_T}_{i,j} + \overline{\rho e_T}_{i-1,j}\right) - \frac{1}{16}\left(\overline{\rho e_T}_{i-2,j} + \overline{\rho e_T}_{i+1,j}\right). \tag{3.33d}$$

The properties over surfaces $(S)_{i,j+\frac{1}{2}}$ and $(S)_{i,j-\frac{1}{2}}$ are defined analogously. This interpolation is a source of error in the method, as well as the approximations used to arrive in equation 3.23.

To obtain the primitive properties over the surfaces of the control volumes, it is first necessary to determine these properties inside the control volumes. These properties are calculated with the Favre averaging, an average weighted by the density. This is another source of error in the numerical method. The velocity components are given by

$$\widetilde{u}_{i,j} = \frac{\overline{\rho u}_{i,j}}{\overline{\rho}_{i,j}} \tag{3.34a}$$

and

$$\widetilde{v}_{i,j} = \frac{\overline{\rho v}_{i,j}}{\overline{\rho}_{i,j}}, \tag{3.34b}$$

the total energy is given by

$$\widetilde{e_T}_{i,j} = \frac{\overline{\rho e_T}_{i,j}}{\overline{\rho}_{i,j}}, \tag{3.34c}$$

the internal energy is

$$\widetilde{e}_{i,j} = \widetilde{e_T}_{i,j} - \frac{1}{2}\left(\widetilde{u}_{i,j}\,\widetilde{u}_{i,j} + \widetilde{v}_{i,j}\,\widetilde{v}_{i,j}\right) \tag{3.34d}$$

and, for an ideal and calorically perfect gas, the temperature is given by

$$\widetilde{T}_{i,j} = \frac{\widetilde{e}_{i,j}}{c_v} \tag{3.34e}$$

and the pressure, by

$$\widetilde{p}_{i,j} = \overline{\rho}_{i,j}\, R\, \widetilde{T}_{i,j}. \tag{3.34f}$$

With these properties, the values over the surfaces can then be calculated with the same scheme used for the conservative variables.

3.2.3 Artificial Dissipation

The numerical method presented in sections 3.2.1 and 3.2.2 includes several approximations that, even though are necessary to solve the Euler equations, introduce numerical errors that need to be controlled in order to ensure the stability of the method and keep the results consistent with the physics the equations describe. In order to achieve this control of the error, an artificial dissipation operator, $\mathcal{D}_i$, described by Miserda, Pimenta e Rocha (2020) and based on the operator proposed by Jameson, Schmidt e Turkel (1981), needs to be included in equation 3.25, which results in

$$\Delta\overline{\mathbf{U}}_{i,j} = -\mathcal{F}_{i,j} + \mathcal{D}_{i,j}. \tag{3.35}$$

$\mathcal{D}_{i,j}$ depends on the artificial dissipation calculated for each surface of the control volume and is given by

$$\mathcal{D}_{i,j} = \left(d_{i+\frac{1}{2}} - d_{i-\frac{1}{2}}\right) + \left(d_{j+\frac{1}{2}} - d_{j-\frac{1}{2}}\right). \tag{3.36}$$

For the surface $\mathbf{S}_{i+\frac{1}{2}}$, for example,

$$d_{i+\frac{1}{2}} = \epsilon^{(2)}_{i+\frac{1}{2}} \left[\overline{\mathbf{U}}_{i+1,j} - \overline{\mathbf{U}}_{i,j}\right] - \epsilon^{(4)}_{i+\frac{1}{2}} \left[\overline{\mathbf{U}}_{i+2,j} - 3\overline{\mathbf{U}}_{i+1,j} + 3\overline{\mathbf{U}}_{i,j} - \overline{\mathbf{U}}_{i-1,j}\right]. \tag{3.37}$$

In equation 3.37, $\epsilon^{(4)}_{i+\frac{1}{2}}$ is the coefficient of the fourth order dissipation operator, given by

$$\epsilon^{(4)}_{i+\frac{1}{2}} = \max\left[0, \left(K^{(4)} - \epsilon^{(2)}_{i+\frac{1}{2}}\right)\right], \tag{3.38}$$

where $K^{(4)}$ is a calibrated constant and $\epsilon^{(2)}_{i+\frac{1}{2}}$ is the coefficient of the second order dissipation operator,

$$\epsilon^{(2)}_{i+\frac{1}{2}} = \max\left[\left(\Psi_{\text{div}}\right)_{i+\frac{1}{2}}, \left(\Psi_{\text{rot}}\right)_{i+\frac{1}{2}}, \left(\Psi_{\text{prs}}\right)_{i+\frac{1}{2}}, \left(\Psi_{\text{den}}\right)_{i+\frac{1}{2}}\right]. \tag{3.39}$$

As equation 3.39 indicates, the coefficient $\epsilon^{(2)}_{i+\frac{1}{2}}$ is calculated as the maximum value of sensors associated with the divergent of the velocity field,

$$\left(\Psi_{\text{div}}\right)_{i+\frac{1}{2}} = K^{(2)}_{\text{div}} \left|\nabla \cdot \widetilde{\mathbf{u}}\right|_{i+\frac{1}{2}}, \tag{3.40a}$$

to the curl of the velocity field,

$$\left(\Psi_{\text{rot}}\right)_{i+\frac{1}{2}} = K^{(2)}_{\text{rot}} \left|\nabla \times \widetilde{\mathbf{u}}\right|_{i+\frac{1}{2}}, \tag{3.40b}$$

to the gradient of the pressure field,

$$\left(\Psi_{\text{prs}}\right)_{i+\frac{1}{2}} = K^{(2)}_{\text{prs}} \left|\nabla \widetilde{p}\right|_{i+\frac{1}{2}}, \tag{3.40c}$$

and to the gradient of the density field,

$$(\Psi_{\text{den}})_{i+\frac{1}{2}} = K_{\text{den}}^{(2)} \, |\nabla \overline{\rho}|_{i+\frac{1}{2}} \, , \tag{3.40d}$$

where $K_{\text{div}}^{(2)}$, $K_{\text{rot}}^{(2)}$, $K_{\text{prs}}^{(2)}$ e $K_{\text{den}}^{(2)}$ are calibrated constants.

3.2.4 Temporal integration

The time advance of equation 3.35 is performed with a third-order Runge-Kutta scheme, given by

$$\overline{\mathbf{U}}_{i,j}^{1} = \overline{\mathbf{U}}_{i,j}^{n} - \left(\mathcal{F}_{i,j}^{n} - \mathcal{D}_{i,j}^{n} \right) , \tag{3.41a}$$

$$\overline{\mathbf{U}}_{i,j}^{2} = \frac{3}{4}\overline{\mathbf{U}}_{i,j}^{n} + \frac{1}{4}\overline{\mathbf{U}}_{i,j}^{1} - \frac{1}{4}\left(\mathcal{F}_{i,j}^{1} - \mathcal{D}_{i,j}^{1} \right) \tag{3.41b}$$

and

$$\overline{\mathbf{U}}_{i,j}^{n+1} = \frac{1}{3}\overline{\mathbf{U}}_{i,j}^{n} + \frac{2}{3}\overline{\mathbf{U}}_{i,j}^{2} - \frac{2}{3}\left(\mathcal{F}_{i,j}^{2} - \mathcal{D}_{i,j}^{2} \right) , \tag{3.41c}$$

where $\overline{\mathbf{U}}_{i,j}^{n}$ is the vector of conservative properties at a certain time step n, $\overline{\mathbf{U}}_{i,j}^{n+1}$ is the vector of conservative properties at the next time step, $n+1$ and $\overline{\mathbf{U}}_{i,j}^{1}$ e $\overline{\mathbf{U}}_{i,j}^{2}$ are the vectors of the conservative properties in the intermediate steps of the Runge-Kutta scheme. Besides that, $\mathcal{F}_{i,j}^{n}$ and $\mathcal{D}_{i,j}^{n}$ are the flux and dissipation vectors calculated with $\overline{\mathbf{U}}_{i,j}^{n}$, $\mathcal{F}_{i,j}^{1}$ e $\mathcal{D}_{i,j}^{1}$ are calculated with $\overline{\mathbf{U}}_{i,j}^{1}$, and $\mathcal{F}_{i,j}^{2}$ and $\mathcal{D}_{i,j}^{2}$ are calculated with $\overline{\mathbf{U}}_{i,j}^{2}$. With this Runge-Kutta scheme, all steps described in sections 3.2.1, 3.2.2 and 3.2.3 are executed three times for each time step.

3.2.5 Stability - CFL Number

Numerical methods with an explicit temporal integration, i.e., in which the properties in a time instant $t_0 + \Delta t$ are directly calculated from the properties in the previous time instant, t_0, need to follow a restriction on the size of the time step, as is explained by Anderson, Tannehill e Pletcher (1997) and Anderson (2009). This restriction is called the Courant-Friedrichs-Lewy (CFL) condition, and is defined as

$$CFL = \frac{(u + c)\,\Delta t}{\Delta x}, \tag{3.42}$$

where u is the maximum velocity of the flow and c is the speed of sound in the undisturbed flow. To prevent the numerical error from growing after each time step, we need to ensure that $CFL \leq 1$ for explicit methods. Based on its definition in equation 3.42, the CFL condition means that the maximum velocity in the flow must be smaller than a certain numerical advance velocity, $\Delta x/\Delta t$, which means that no information that propagates in the flow can move from a certain control volume $V_{i,j}$ at time step n directly to control volume $V_{i+2,j}$, for example, at the time step $n+1$, without first passing through control volume $V_{i+1,j}$. A more detailed explanation, based on the hyperbolic nature of the governing equations, is given by Anderson (2009).

3.2.6 Immersed Boundary Methodology

This numerical method described from sections 3.2.1 to 3.2.4 is applied indistinctly to all control volumes in the domain. Therefore, after each Runge-Kutta step, it is necessary to apply the boundary conditions on the solid walls. In this work, a moving body, immersed boundary method is used, because it is a simple method of applying boundary conditions for cases with regular cartesian meshes. With this method, the boundary conditions are directly applied to the control volumes that contain the solid walls. The boundary condition for the velocity is impenetrability, which means that the normal component of the fluid velocity at the wall, $\widetilde{u}_n$, is equal to the normal component of the velocity of the wall, u_{n_b}. The subscript b indicates that the property is evaluated at the boundary and the subscript n indicates the normal direction. In addition to that, there is no momentum diffusion at the wall, which means that

$$\frac{\partial \widetilde{\mathbf{u}}}{\partial x_n} = 0. \tag{3.43}$$

From the momentum equation (3.5), we see that the boundary condition for the static pressure is

$$\frac{\partial \widetilde{p}}{\partial x_n} = 0. \tag{3.44}$$

The boundary condition for the temperature is given by the hypothesis that the walls are isentropic,

$$\frac{\partial \widetilde{T}}{\partial x_n} = 0. \tag{3.45}$$

This condition, along with the condition for pressure, implies that, for an ideal and calorically perfect gas, the boundary conditions for density and internal energy are

$$\frac{\partial \overline{\rho}}{\partial x} = 0 \tag{3.46}$$

and

$$\frac{\partial \widetilde{e}}{\partial x} = 0. \tag{3.47}$$

If the wall-normal unit vector is $\mathbf{n} = n_x\mathbf{i} + n_y\mathbf{j}$, for a two-dimensional case, the derivatives can be written as

$$\frac{\partial \widetilde{\mathbf{u}}}{\partial x_n} = n_x \frac{\partial \widetilde{\mathbf{u}}}{\partial x} + n_y \frac{\partial \widetilde{\mathbf{u}}}{\partial y}, \tag{3.48a}$$

$$\frac{\partial \overline{\rho}}{\partial x_n} = n_x \frac{\partial \overline{\rho}}{\partial x} + n_y \frac{\partial \overline{\rho}}{\partial y} \tag{3.48b}$$

and

$$\frac{\partial \widetilde{e}}{\partial x_n} = n_x \frac{\partial \widetilde{e}}{\partial x} + n_y \frac{\partial \widetilde{e}}{\partial y}. \tag{3.48c}$$

These equations can be rewritten, with the boundary conditions, as

$$0 = n_x \left(\frac{\partial \widetilde{\mathbf{u}}}{\partial x}\right)_{i,j}^{b} + n_y \left(\frac{\partial \widetilde{\mathbf{u}}}{\partial y}\right)_{i,j}^{b}, \tag{3.49}$$

$$0 = n_x \left(\frac{\partial \overline{\rho}}{\partial x}\right)_{i,j}^{b} + n_y \left(\frac{\partial \overline{\rho}}{\partial y}\right)_{i,j}^{b}, \tag{3.50}$$

$$0 = n_x \left(\frac{\partial \widetilde{e}}{\partial x}\right)_{i,j}^{b} + n_y \left(\frac{\partial \widetilde{e}}{\partial y}\right)_{i,j}^{b}, \tag{3.51}$$

The derivatives in equations 3.49, 3.50 and 3.51 are calculated with a fourth-order precision, finite differences scheme proposed by Anderson, Tannehill e Pletcher (1997). The derivative of the density in the x direction, for example, is given by

$$\left(\frac{\partial \overline{\rho}}{\partial x}\right)_{i,j}^{b} = \frac{1}{12\Delta x}\left[-25\overline{\rho}_{i,j}^{b} + 48\overline{\rho}_{i+1,j} - 36\overline{\rho}_{i+2,j} + 16\overline{\rho}_{i+3,j} - 3\overline{\rho}_{i+4,j} + \mathcal{O}\left(\Delta x\right)^4\right] \tag{3.52a}$$

if the n_x component is in the positive x axis direction, or

$$\left(\frac{\partial \overline{\rho}}{\partial x}\right)_{i,j}^{b} = \frac{1}{12\Delta x}\left[-25\overline{\rho}_{i,j}^{b} + 48\overline{\rho}_{i-1,j} - 36\overline{\rho}_{i-2,j} + 16\overline{\rho}_{i-3,j} - 3\overline{\rho}_{i-4,j} + \mathcal{O}\left(\Delta x\right)^4\right] \tag{3.52b}$$

if n_x is in the negative direction.

It is then possible to define the difference operators

$$D_i^{+}\overline{\rho} = \frac{1}{25}\left(48\overline{\rho}_{i+1,j} - 36\overline{\rho}_{i+2,j} + 16\overline{\rho}_{i+3,j} - 3\overline{\rho}_{i+4,j}\right) \tag{3.53a}$$

and

$$D_i^{-}\overline{\rho} = \frac{1}{25}\left(48\overline{\rho}_{i-1,j} - 36\overline{\rho}_{i-2,j} + 16\overline{\rho}_{i-3,j} - 3\overline{\rho}_{i-4,j}\right). \tag{3.53b}$$

The difference operators for the y direction and for the other properties are analogously defined. With these operators, the boundary conditions are applied as

$$\overline{\rho}_{i,j}^{b} = \frac{|n_x|\, D_i\overline{\rho} + |n_y|\, D_j\overline{\rho}}{|n_x| + |n_y|} \tag{3.54}$$

for the density,

$$\widetilde{\mathbf{u}}_{i,j}^{b} = \frac{|n_x|\, D_i\widetilde{\mathbf{u}} + |n_y|\, D_j\widetilde{\mathbf{u}}}{|n_x| + |n_y|} \tag{3.55}$$

for the velocity and

$$\widetilde{e}_{i,j}^{b} = \frac{|n_x|\, D_i\widetilde{e} + |n_y|\, D_j\widetilde{e}}{|n_x| + |n_y|} \tag{3.56}$$

for the internal energy.

Since the normal velocity components at the boundary,

$$(\widetilde{\mathbf{u}}_n)_{i,j}^{b} = \left(\widetilde{u}_{n_x}\mathbf{i} + \widetilde{u}_{n_y}\mathbf{j}\right)_{i,j}^{b} \tag{3.57}$$

and the velocity at the boundary,

$$\widetilde{\mathbf{u}}_{i,j}^{b} = \left(\widetilde{u}\mathbf{i} + \widetilde{v}\mathbf{j}\right) \tag{3.58}$$

are known, it is then possible to calculate the tangential components of the velocity at the boundary, as

$$(\widetilde{u_{tx}})_{i,j}^{b} = (\widetilde{u} - \widetilde{u_{nx}})_{i,j}^{b} \tag{3.59}$$

and

$$\left(\widetilde{u_{ty}}\right)_{i,j}^{b} = \left(\widetilde{v} - \widetilde{u_{ny}}\right)_{i,j}^{b}. \tag{3.60}$$

Thus, the conservative properties at the boundary points are given by

$$\overline{\mathbf{U}}_{i,j}^{b} = \left[\begin{array}{c} \overline{\rho} \\ \overline{\rho}\left(\widetilde{u}_{t_x} + \widetilde{u}_{n_x}\right) \\ \overline{\rho}\left(\widetilde{u}_{t_y} + \widetilde{u}_{n_y}\right) \\ \overline{\rho}_i^b\left[\widetilde{e}_i^b + \frac{1}{2}\left[\left(\widetilde{u}_{t_x} + \widetilde{u}_{n_x}\right)\left(\widetilde{u}_{t_x} + \widetilde{u}_{n_x}\right) + \left(\widetilde{u}_{t_y} + \widetilde{u}_{n_y}\right)\left(\widetilde{u}_{t_y} + \widetilde{u}_{n_y}\right)\right]\right] \end{array}\right]_{i,j}^{b}. \tag{3.61}$$

To prevent the extremities of the computational domain from interfering with the flow, the domain is divided into two regions. The regular region is the region of the flow of interest and has a uniform cartesian mesh. The stretched region, on the other hand, is composed of control volumes that grow with a geometric progression, which results in very long, stretched control volumes. The effects of this region are the dissipation of the structures of the flow and an increase in the time necessary for perturbations that are reflected in the extremities to return to the regular region, without the need for a much higher number of control volumes. This prevents the reflection, especially of sound waves, on the extremities of the computational domain. At the extremities, the applied boundary conditions are of null derivatives for the velocity, density and internal energy.

3.3 Simulations - Discretization, Setup and Parameters

The numerical method presented in the previous section has been implemented in a parallel code called the Virtual Aeroacoustic Tunnel (VAT) by professors and students from the Computational Aeroacoustics Laboratory at The University of Brasilia (CAALab - UnB) and has been used in several previous research projects, such as Pimenta (2016) and Miserda, Pimenta e Rocha (2020). We chose to use this method in the present work because it is highly robust, as the explicit artificial dissipation allows for full control over the strategy for numerical error control. In addition to that, the method uses a non-amplifying interpolation scheme, which contributes to the stability of the solution (PIMENTA, 2016).

The VAT code is implemented in FORTRAN language and parallelized with both shared and distributed memory strategies, using OpenMP and MPI, respectively and is executed in the AMADEA cluster, installed at the CAALab. The cluster is composed of 8 nodes, each fitted with an Intel Xeon Phi 7230 Knights Landing CPU, with 64 cores and capable of performing 1024 simultaneous double precision floating point operations per cycle. Each node is also equipped with 96 GB of MCDRAM memory, and the cluster has a total storage space of 12 TB. The cluster also contains a visualisation node, equipped with an Intel Xeon E5 2620V4 CPU, 256 GB of RAM memory and an Nvidia Quadro P5000 GPU.

All simulations of the flow around a cylinder in the present work were performed with the same domain configuration. The regular region depicted in figure 3.1 has dimensions of $25D \times 25D$, where D is the diameter of the cylinder, used as a reference length. Some measurement probes were distributed over the domain to capture pressure signals in specific regions. Probes 1-6 are located upwind of the cylinder and are meant to capture the sound waves that propagate upwind. Probes 7-12 are located downwind from the cylinder and are meant to describe the flow inside the wake (probes 7-9 in particular) and sound waves that propagate downwind (probes 10-12). Probes 13-16 are located directly above the cylinder, in the region where the maximum value for the sound intensity was calculated. The flow is mostly symmetric with respect to $y = 0$ except for a phase shift of π rad, so it is not necessary to place probes at the bottom half of the domain.

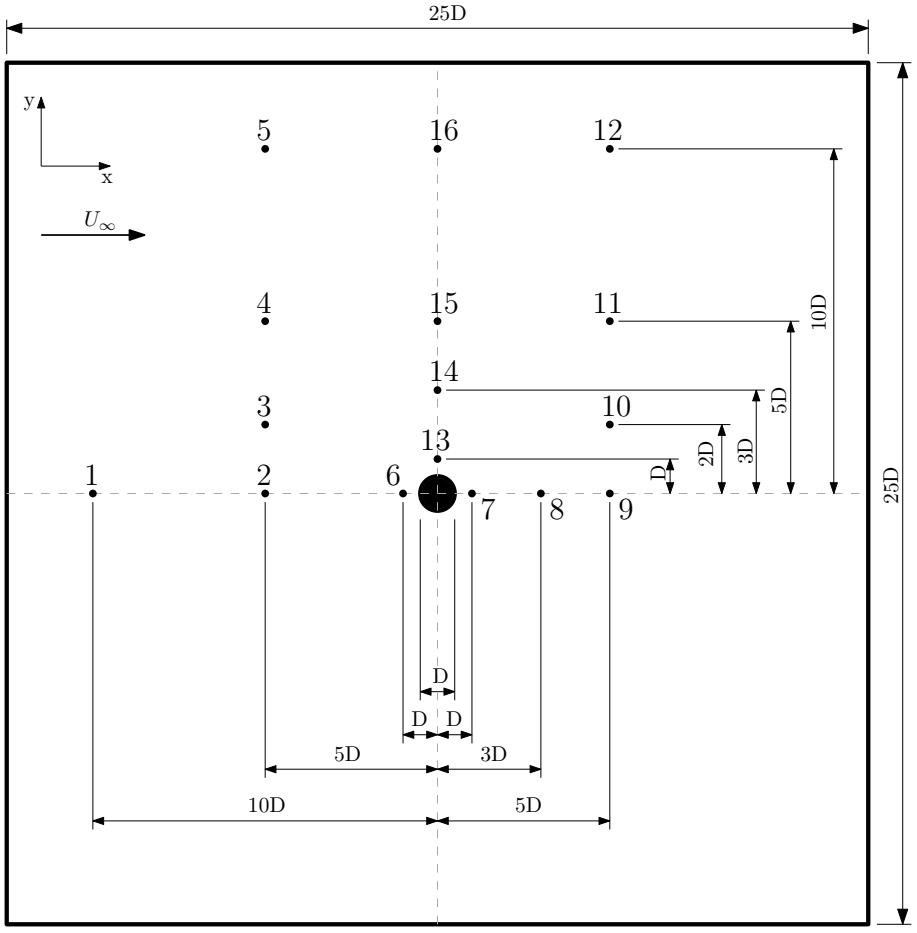

Figura 3.1 – Configuration of the regular region of the domain.

3.3.1 Spatial and Temporal Discretization

For most of the simulations, for $M_\infty = 0.5$ and $M_\infty = 0.75$, the regular region of the domain was discretized with 128 control volumes along the diameter of the cylinder, which corresponds to $\Delta x = \Delta y = 0.0078125D$. This leads to a regular region with around 10^7 control volumes. Figure 3.2a shows the resulting computational grid in this regular

region. The time step chosen for the simulation with $M_\infty = 0.5$ was 6.0×10^{-6}, as it leads to a CFL number around 0.4 (equation 3.42). An additional simulation was performed for $M_\infty = 0.5$, with a discretization of 256 control volumes along the diameter of the cylinder, with the objective of checking if the discretization is satisfactory. To maintain the CFL number at 0.4, the time step for this simulation was 3.0×10^{-6}. The time step chosen for the simulation with $M_\infty = 0.75$ was 1.5×10^{-6}. This led to a CFL number of around 0.12, a necessary reduction due to the increased complexity of the flow when compared to $M_\infty = 0.5$.

In addition to the regular region, the computational domain contains a stretched region, composed of 256 control volumes in each direction. These control volumes start with the same size as those of the regular region and grow with a geometric progression with a ratio of 1.05. As a consequence, the last control volumes have a dimension of approximately $2076D$. As stated previously, the function of this stretched region is to allow pressure fluctuations to propagate while they are dissipated by the growing control volumes. This prevents the reflection of sound waves in the extremities of the domain and ensures that no "artificial" reflections interfere with the flow in the regular region. With this region, the entire computational domain has around 1.3×10^7 control volumes. Figure 3.2b shows the entire discretized domain. In this figure, the regular region is located at the center, but cannot be distinguished with this figure's resolution. For comparison, the largest control volumes, at the corners of the domain, are around 85 times larger than the entire regular region.

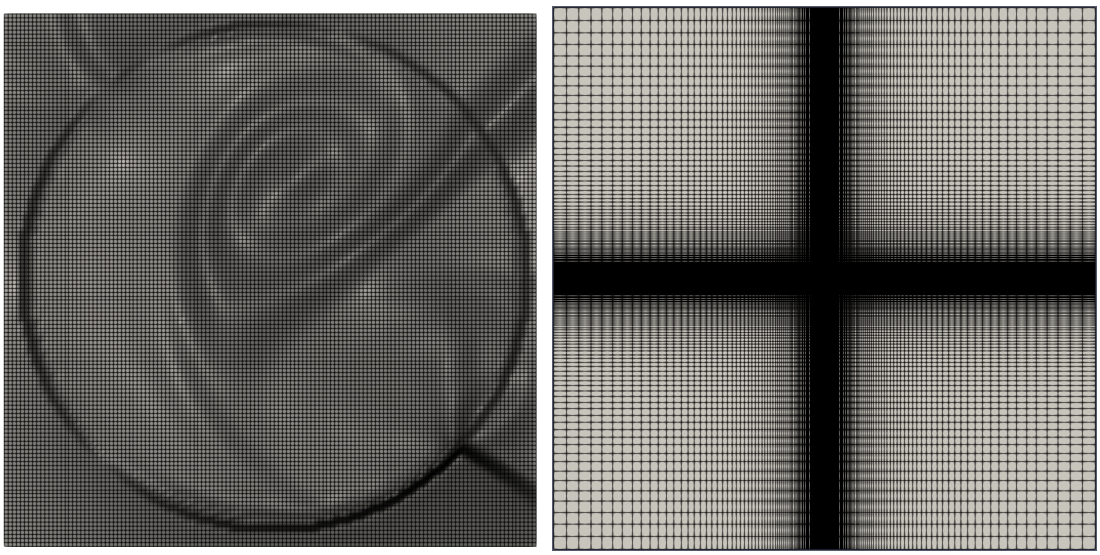

(a) Discretization of the cylinder. (b) Stretched region.

Figura 3.2 – Computational grid.

3.3.2 Simulation Parameters

The same reference fluid properties were used for both cases. The reference pressure p_∞ was equal to 101300 Pa and the reference temperature T_∞ was 300 K. The ratio of

specific heats for air γ was 1.4 and the gas constant R was 287 J/(kg K).

Table 1 shows the artificial dissipation calibration parameters, described in section 3.2.3. The values used for $M_\infty = 0.5$ were the default parameters used for most simulations with the vat code. For $M_\infty = 0.75$, however, it was necessary to increase these values by five times to control the numerical error. This and the smaller CFL number are signs of how this case is much more complex than the previous one.

Tabela 1 – Artificial Dissipation Calibration Parameters

Parameter	$M_\infty = 0.5$	$M_\infty = 0.75$
$K^{(2)}_{div}$	1.0×10^{-3}	5.0×10^{-3}
$K^{(2)}_{rot}$	1.0×10^{-3}	5.0×10^{-3}
$K^{(2)}_{prs}$	1.0×10^{-2}	5.0×10^{-2}
$K^{(2)}_{den}$	1.0×10^{-2}	5.0×10^{-2}
$K^{(4)}$	1.0×10^{-1}	5.0×10^{-1}

3.3.3 Performance and Outputs

Only one node from the AMADEA cluster was necessary for the execution of the VAT code with the standard discretization used in the present work, of 128 control volumes along the diameter. The approximate time required for the solution of the equations at each time step was 0.112 s.

Output files periodically were periodically generated to build the data sets used by the POD and DMD. These outputs contain the pressure at each control volume as well as the coordinates of the volumes and are written with double precision in files with FORTRAN's binary format. The time spent to write each output file was around 81 s and each file had a size of 420 MiB. This means that the total time required to generate the 400 snapshots used for the flow decomposition with $M_\infty = 0.5$ was around 9 h and the results occupied 166.8 GiB of disk space. In contrast, the rest of the simulation that generated this data set took only about 1 h and 40 min. The 800 snapshots for the analysis of the flow with $M_\infty = 0.75$ were generated in approximately 18 h and occupied 373.5 GiB, while the rest of the simulation took around 4 h and 40 min.

3.4 Modal Decomposition Methods

The decomposition methods used in the present work were implemented in FORTRAN language, especially because the output files from the vat code are written in FORTRAN's binary format. These files are written with some details that make them difficult to read with other programming languages. Except for this aspect, the methods could have been implemented in different programming languages, such as Python or

Matlab/octave without problem, as it is also possible to run programs in these languages in the cluster and there would not have been much loss of performance as the codes were not parallelized.

The following sections present the main steps of the POD and DMD methods as they were implemented, as well as some particularities that might not be obvious from the description of the methods in chapter 2.

3.4.1 POD Algorithm

Step 1 - Read files: The first step of the POD algorithm is to read the binary output files and build the data matrix $\mathbf{X}$. This is one of the most time-consuming steps.

Step 2 - Singular Value Decomposition: The second step is to calculate the singular value decomposition of the data matrix. The LAPACK function DGESVDX was used for the calculation. Its advantage is that it only calculates the first r singular values and corresponding singular vectors. The left singular vectors are the POD modes. This step also has a significant computational cost.

Step 3 - Calculate temporal coefficients: The third step is to calculate temporal coefficients as $\mathbf{A} = \mathbf{X}\left(\mathbf{U^r}\right)^{\mathbf{T}}$. Since the DGESVDX function used to calculate the SVD in the previous step destroys the contents of matrix $\mathbf{X}$, it is necessary to either copy the matrix or read the files again. This choice depends on the available memory and time.

Step 4 - Flow reconstruction: With the first r POD modes and the temporal coefficients, it is then possible to calculate the flow reconstruction with $\mathbf{X^r} = \mathbf{U^r A}$.

3.4.2 DMD Algorithm

Step 1 - Read files: The beginning of the DMD algorithm is similar to the POD. First, it is necessary to read the output files used to build matrices $\mathbf{X}$ and $\mathbf{X}'$. These matrices have $m-2$ columns in common, so ideally these columns should only be stored once. But the same issue from the POD happens here. The SVD calculation destroys the content of $\mathbf{X}$, so it is necessary to either copy the data or read it again later.

Step 2 - Singular Value Decomposition: The next step is to calculate the Singular Value Decomposition of $\mathbf{X}$. Again, the DGESVDX function was used to calculate the first r singular values $\mathbf{\Sigma}^r$ and the first singular vectors $\mathbf{U}^r$ and $\left(\mathbf{v}^T\right)^r$.

Step 3 - Calculate $\tilde{\mathbf{A}}$: The third step is to calculate $\tilde{\mathbf{A}} = \mathbf{U^r X' V^r \Sigma}^{r^{-1}}$, the matrix that approximates the reduced order linear system.

Step 4 - Eigendecomposition: The fourth step is to calculate the eigendecomposition of $\tilde{\mathbf{A}}$. The eigenvectors are the complex-valued DMD modes, and the real part is used for the analysis of the mode shapes. The eigenvalues λ are associated with the frequencies, $f_k = \arg(\lambda_k)/2\pi\Delta t$, and the rates of growth, $\varsigma_k = \mathrm{Re}(\ln(\lambda_k))$.

Step 5 - calculation of $\mathbf{\Phi}^{-1}$ and b: To calculate the flow reconstruction, it is first necessary to calculate the vector $\mathbf{b} = \mathbf{\Phi}^{-1}\mathbf{x}_1$, that corresponds to the initial condition for each mode. To calculate the inverse matrix $\mathbf{\Phi}^{-1}$, we used the Singular Value Decomposition of $\mathbf{\Phi}$, $\mathbf{\Phi}^{-1} = \mathbf{V}\mathbf{\Sigma}^{-1}\mathbf{U}^T$.

Step 6 - Flow reconstruction: The last step is to calculate the flow reconstruction with the DMD modes, $\mathbf{x}(t) = \mathbf{\Phi}\exp(\mathbf{\Omega}t)\,\mathbf{b}$, where $\omega_k = \log(\lambda_k)/\Delta t$.

Table 2 shows the required time for each step of the DMD method. These times were measured during the analysis of the flow with $M_\infty = 0.75$, which used 800 snapshots. The table shows how the time for each step scales with the number of calculated modes, r. The most time-consuming steps of the method are reading the files and calculating the singular value decomposition of the data, and the steps more dependent on the number of calculated modes are the svd, the calculation of $\tilde{\mathbf{A}}$ and the calculation of $\mathbf{\Phi}^{-1}$.

Tabela 2 – Time for each step of the DMD algorithm, for different numbers of modes

Step	Time (s)		
	$r = 21$	$r = 51$	$r = 91$
1	2527 (42 min)	2453 (40 min)	2706 (45 min)
2	9709 (161 min)	10389 (173 min)	11874 (197.9 min)
3	73.9	122	187
4	8.4	0.007	0.03
5	44	232	704 (11 min)
6	0.3	0.5	0.8
total	12630 (210 min)	13865 (231 min)	16723 (278 min)

The total time shown in table 2 includes the time spent writing the results to files, as well as some other computational steps that are not directly part of the DMD algorithm, such as variable declaration and memory allocation and deallocation.

3.4.3 Practical Aspects and Challenges

Even though the analysis methods were executed in the cluster, they were implemented in serial code. This was justified, firstly, by the novelty of the algorithms, as implementing new methods directly into parallel code is a big challenge. In addition to that, the most time-consuming steps of the analysis are reading the data files and calculating the singular value decomposition. Since we used functions from GCC's LAPACK library for these calculations, we have no control over their optimisation. We tried to use the functions available in the Intel oneAPI's High-Performance Computing toolkit but there

were some issues with its installation on the cluster's visualisation node. Some smaller tests on the regular nodes, however, indicate this library is more optimised when compared to GCC's. One final reason is that these methods are mostly memory bound and had to be executed in the visualisation node, which has more memory but lower processing power. This lack of parallelism did not compromise the analysis in any way, as for this problem the memory use is a much greater constraint than processing time. In addition to that, table 2 shows that even the longest analysis took less than 5 h to run completely, and in the world of computational fluid dynamics, this is not at all a long time. The methods would benefit, however, from distributed memory parallelism, as it would allow the use of multiple nodes, with more combined memory than the visualisation nodes, but this would require a different algorithm, such as the ones proposed by Hemati, Williams e Rowley (2014) or Anantharamu e Mahesh (2019).

Over the course of this work, the use of the FORTRAN binary format for the outputs from the vat code proved to be a hindrance in some points. These files have some features that make them difficult to read with other programming languages. In addition to that, there was a recurring, and not yet explained problem with reading the files in the first step of the POD and DMD methods. On some occasions, a file that had been read normally in a previous run would appear to be corrupted but, in a posterior run, would be read correctly again.

4 Results

This chapter presents the investigation of the flows past a cylinder with Mach numbers of 0.5 and 0.75. For each case, the dynamics of the flow are analysed and compared to the literature. The pressure field results are then decomposed using the Proper Orthogonal Decomposition (POD) and the Dynamic Modes Decomposition (DMD) methods. Finally, the flow structures, or modes, obtained from the decompositions are used for the reconstruction of the flows, and the influence of the data set and the number of modes on the quality of the reconstruction is investigated.

The choice for the Mach numbers used in this work was guided by the results presented by Botta (1995). The author reported that $M_\infty = 0.5$ is close to the critical value that results in the separation and emission of vortices through the mechanisms described in section 2.1.1 but at this point, the flow is still periodic. This simplicity made it an interesting preliminary case for the observation of how the DMD method extracts coherent structures with specific frequencies.

A Mach number of 0.75, on the other hand, was chosen because it is in the region between 0.6 and 0.9 in which Botta (1995) described the flow as chaotic, with a richer frequency content. This case allowed for the further exploration of the DMD's capability of identifying flow structures that correspond to the dominating frequencies and, in particular, structures associated with noise generation. It was also a more interesting opportunity to evaluate the capability of the POD and DMD methods to provide reconstructions of the flow field from a small number of modes.

For both cases, we can divide the flow into two parts with distinct natures, to simplify the description of the observed phenomena. One is the von Kármán vortex street, located in the wake, downwind from the cylinder. This region is dominated by aerodynamic effects, and the vortices are transported by the flow. The other is the acoustic region, dominated by the pressure fluctuations that propagate in all directions with the speed of sound.

4.1 Grid Test

Before properly studying the flow around the cylinder, we investigated the influence of the spatial and temporal discretizations through a simple, qualitative test. We chose this simpler approach instead of a formal grid convergence study because the convergence of the VAT code has been demonstrated by Miserda, Pimenta e Rocha (2020). For this test, the simulations were performed with two spatial discretizations, $\Delta x = D/128$ and $\Delta x = D/256$, and time steps were adjusted to maintain the same CFL. Figure 4.1 depicts the results of the simulations. Figures 4.1a and 4.1b show the flow visualisations for both cases with a variable defined as $\beta_T = |\nabla T|^{1/10}$. This variable was chosen because it brings the acoustic and aerodynamic fluctuations to the same order of magnitude, allowing visualisation of all physical phenomena in the flow. These figures show that the simulation results for the different spatial discretizations are very similar, and the use of the coarser grid yields a satisfactory result.

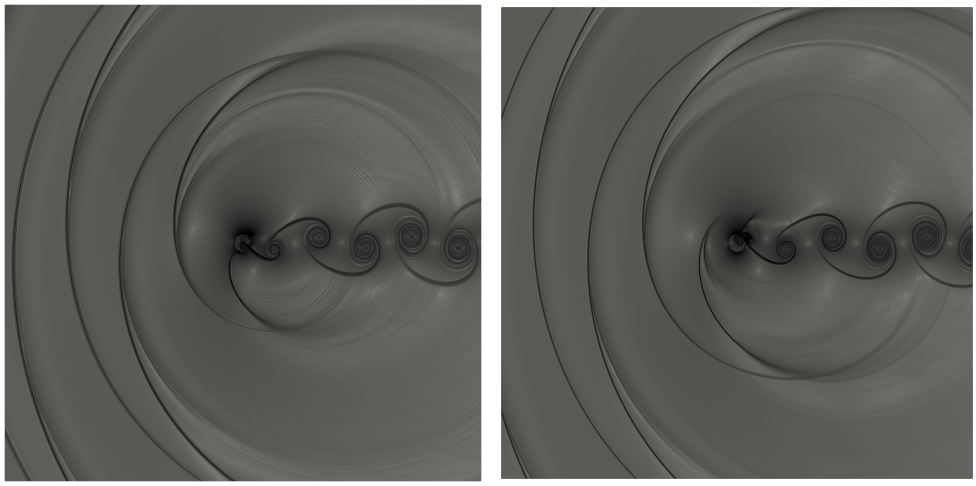

(a) β_T, $\Delta x = D/128$.

(b) β_T, $\Delta x = D/256$.

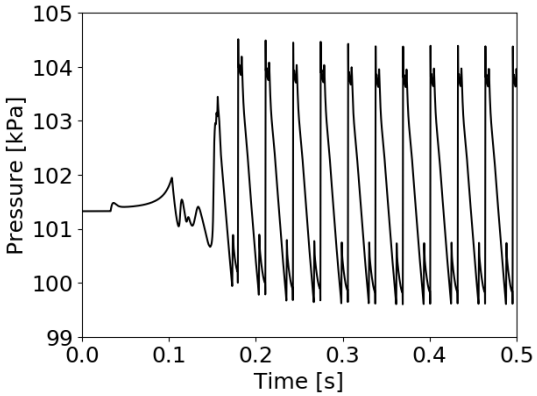

(c) Probe 5, $\Delta x = D/128$.

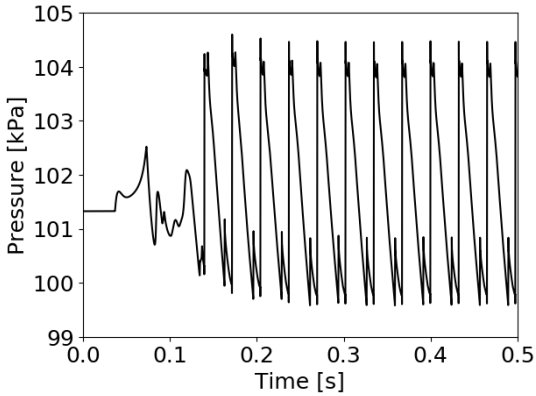

(d) Probe 5, $\Delta x = D/256$.

Figura 4.1 – Grid test, $M_\infty = 0.5$.

The pressure signals at probe 5 (see figure 3.1 for the position of the probe), presented in figures 4.1c and 4.1d, show that the change in discretization influences the initial part of the flow, which begins steady and numerical instabilities cause the break

in symmetry and the alternating emission of vortices and shock waves. Other than this difference, which leads to a difference in phase for the signals, the results are also very similar.

Based on this test, we decided to use the coarser discretization, with $\Delta x = D/128$, for the rest of this work, as the more refined grid does not provide much better results but would require 4 times as much memory, making the decomposition analyses much more computationally expensive.

4.2 Mach 0.5

The flow around the cylinder with a Mach number of 0.5 is illustrated in figure 4.2 with different variables for the same time instant. Figure 4.2a shows the pressure field and figure 4.2b shows the visualisation variable β_T, while figures 4.2c and 4.2d depict the Mach number and vorticity, respectively.

As the flow passes through the cylinder, it is accelerated until it reaches a locally supersonic velocity, as shown in the Mach number visualisation in figure 4.2c, where the contour line marks $M = 1.0$. Eventually, a shock wave decelerates the flow back to subsonic condition, but the strong compression associated with the shock causes the separation of the flow and, consequently, the emission of vortices and the formation of a von Kármán vortex street. As the vortices shed from the cylinder, the shock waves also detach from the surface and propagate, as pressure waves, away from the cylinder. This dynamic can be seen in the video of the temporal advance of the β_T field, available here, and in the pressure signals shown in figure 4.3, extracted from probes shown in the diagram on figure 3.1. The vorticity shown in figure 4.2d is a consequence of the baroclinity of the flow, as the use of equation 3.8 allows for a misalignment of the pressure and density gradients.

The upwind probes (figures 4.3a and 4.3b) show that the pressure waves that propagate upwind present very intense discontinuities, resembling the shock waves that originated them. A comparison of these two signals shows that, because probe 1 is at the same vertical position as the cylinder ($y = 0$), it captures equally the pressure waves emitted from the upper and the lower surfaces of the cylinder. Probe 5, on the other hand, is above this line of symmetry, at $y = 10$, and thus at this point the intensity of the wave emitted from the upper surface is much higher than the emitted from the lower. This is a consequence of the strong irreversibility of these waves, which dissipate as they propagate.

The downwind probes (figures 4.3c and 4.3d) capture the pressure fluctuations due to the passage of the low-pressure core of the vortices. Since probe 7 is positioned at $y = 0$, its signal depicts the passage of both the upper and lower vortices, while probe 10, with $y = 2$, is mostly influenced by the upper vortex and by lower intensity pressure waves that propagate downwind.

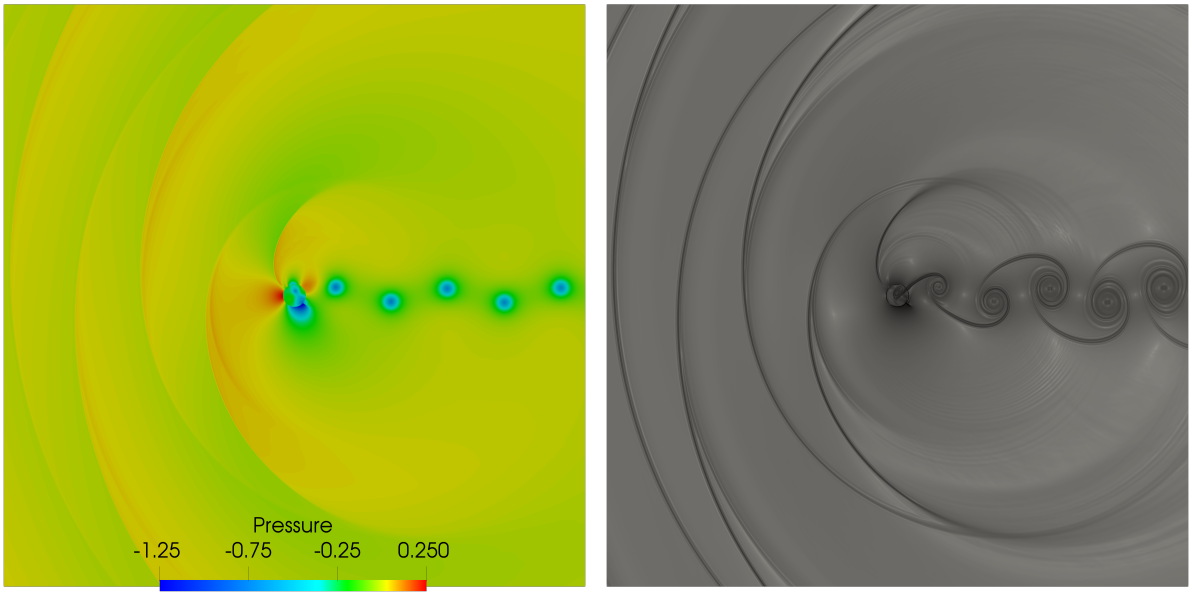

(a) Pressure.

(b) β_T.

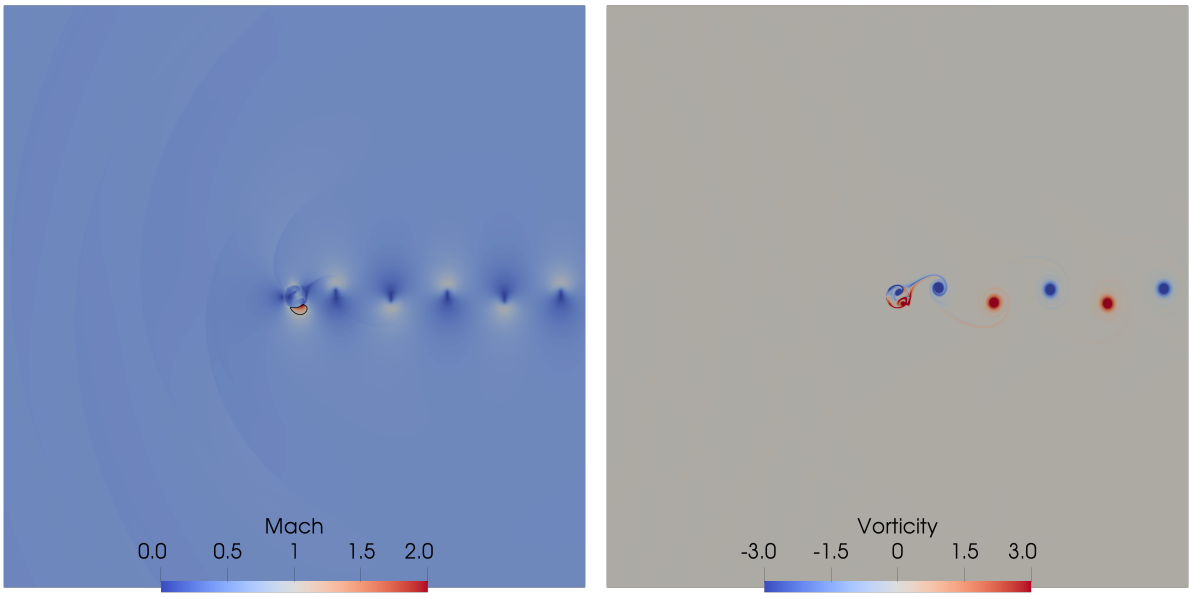

(c) Mach number.

(d) Vorticity.

Figura 4.2 – Flow visualisation, $M_\infty = 0.5$.

The probes located directly above the cylinder (figures 4.3e and 4.3f), at $x = 0$, also capture the passage of the pressure waves that propagate when the shock separates from the cylinder surface. These signals present the highest pressure fluctuations observed which indicates that this is the preferential direction for noise propagation. These pressure signals, in a similar manner to those obtained upwind, present very strong pressure gradients in the compression phase of the waves.

The flow visualisation from figure 4.2 and the pressure signals from figure 4.3 all indicate a periodic flow. This observation is reinforced by the pressure spectra depicted in figure 4.4. The spectra show that the Strouhal number (St), Eq. 2.1, for the flow is approximately 0.18, a result consistent with the literature. The spectra for the pressure signals for probes 1 and 7 (figures 4.4a and 4.4c) present the dominant peak at $St = 0.36$,

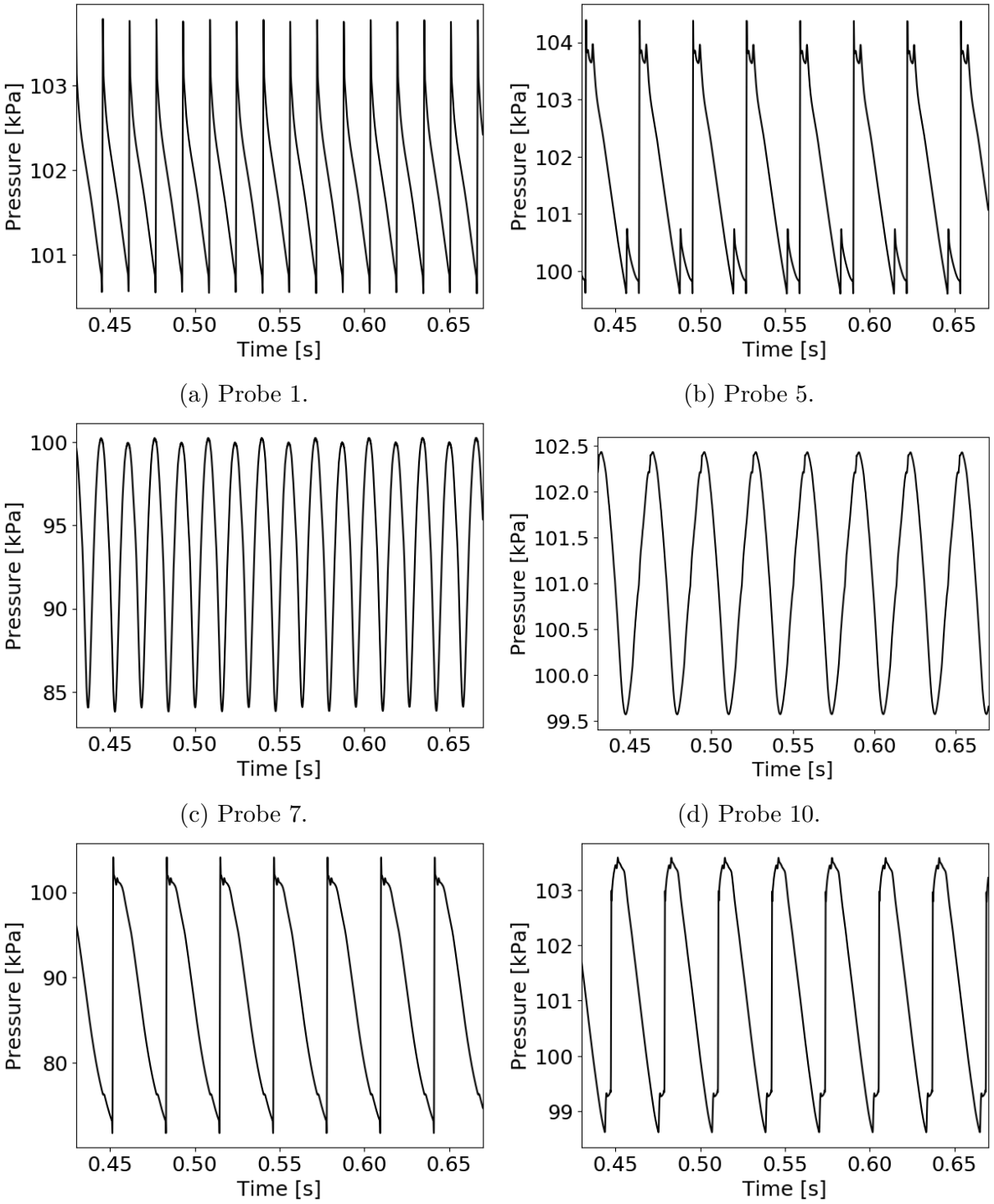

(a) Probe 1.

(b) Probe 5.

(c) Probe 7.

(d) Probe 10.

(e) Probe 13.

(f) Probe 16.

Figura 4.3 – Time domain pressure signals at selected probes.

the first harmonic of the fundamental frequency, because, as discussed before, these probes are located at the symmetry line $y = 0$. Therefore they capture equally the pressure waves (probe 1) or the vortices (probe 7) emitted from the upper and the lower sides of the cylinder.

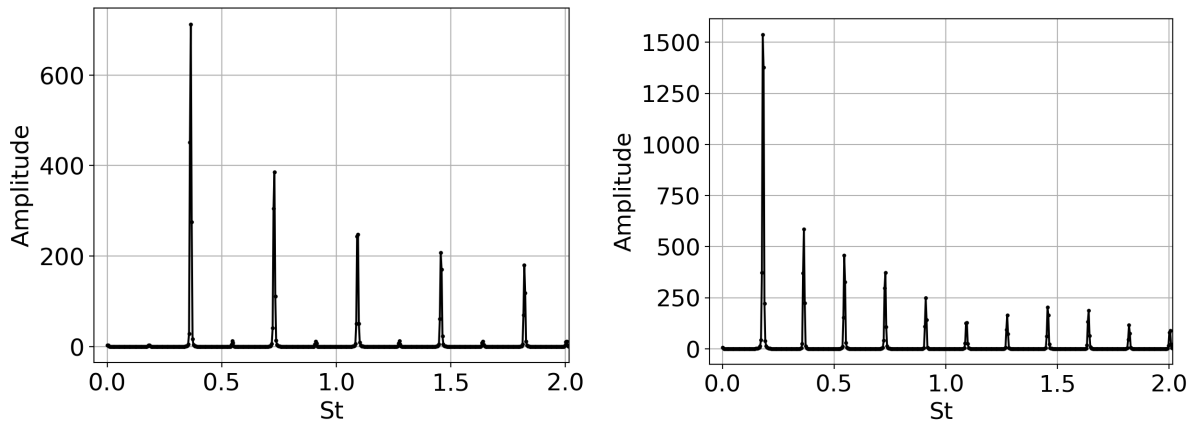

(a) Probe 1.

(b) Probe 5.

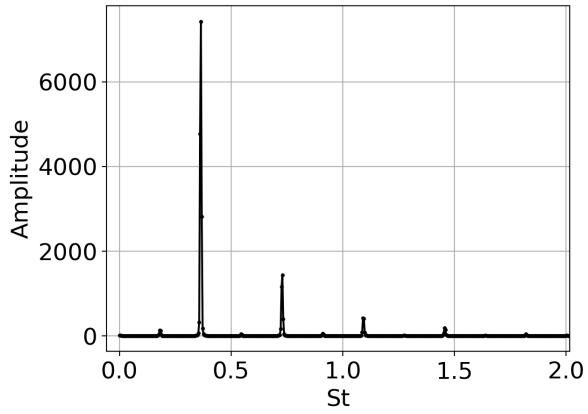

(c) Probe 7.

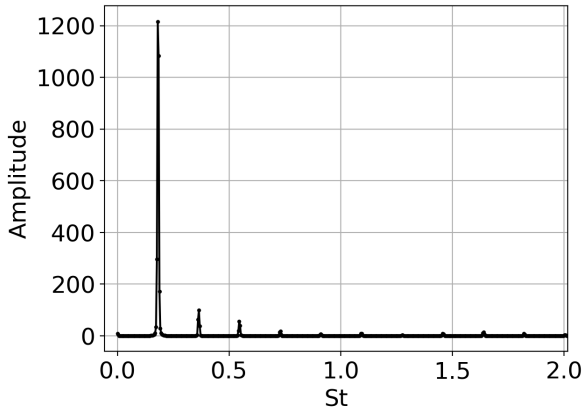

(d) Probe 10.

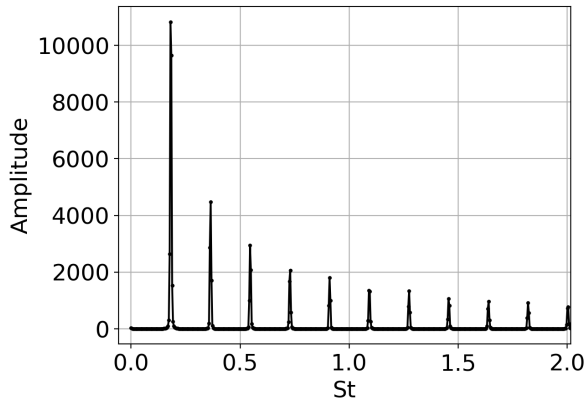

(e) Probe 13.

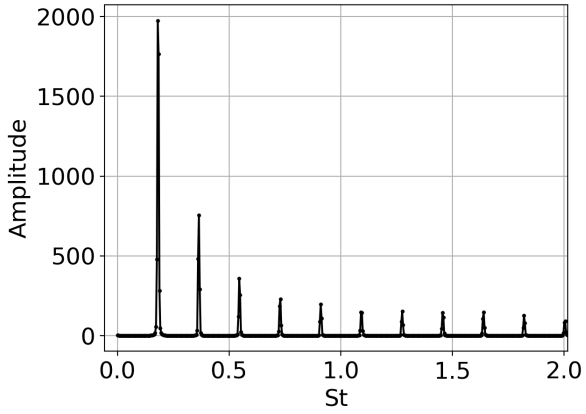

(f) Probe 16.

Figura 4.4 – Pressure spectra as a function of the Strouhal number at selected probes.

To better understand the noise generated by the flow, the Sound Pressure Level (SPL) field was calculated as

$$SPL = 20 \log_{10} \left(\frac{p'_{rms}}{2 \times 10^{-5}} \right), \tag{4.1}$$

were p'_{rms} is the root mean square value of the pressure fluctuations $p' = p - \overline{p}$ and 2×10^{-5} Pa corresponds to the lower limit of the human hearing capacity. The result is shown in figure 4.5. The SPL field shows that the regions above and below the cylinder present the highest noise intensity, due to the shock waves that appear in these regions. As these waves

propagate, their amplitudes decrease, and the SPL values decrease as a result. It is also possible to observe the pseudo-noise at the vortex wake. This is a result of the pressure fluctuations due to the passage of the low-pressure vortex cores, which are computed by equation 4.1 without distinction from the acoustic pressure fluctuations. These fluctuations are called pseudo-noise because they are of an aerodynamic nature, and propagate with the velocity of the flow.

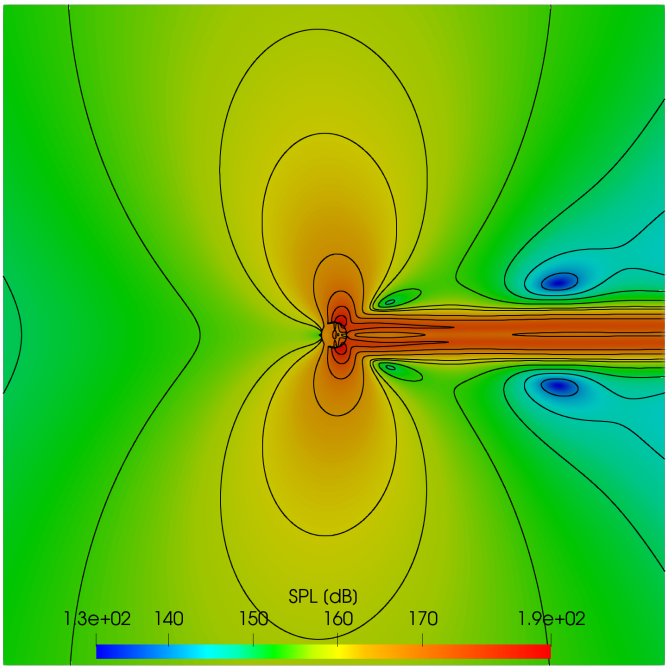

Figura 4.5 – Sound Pressure Level field, $M_\infty = 0.5$.

4.2.1 Proper Orthogonal Decomposition

The results from the simulation of the flow around a cylinder with a Mach number of 0.5 were decomposed using the Proper Orthogonal Decomposition (POD) method. In order to build the data matrix $\mathbf{X}$ mentioned in section 2.2, a data set of pressure snapshots was created by the evaluation of the pressure field at a rate of 40 snapshots per period over a total time corresponding to 10 periods, using the fundamental frequency as a reference.

Figure 4.6 shows the calculated singular values, and figure 4.7 shows some selected POD modes, numbered according to their corresponding singular values ordered from highest to lowest. From the interpretation of the POD modes given by Weiss (2019) and described in section 2.2, the partial sum of the singular values, $\sum_{k=1}^{i} \sigma_k / \sum_{k=1}^{r} \sigma_k$, represents the fraction of the total variance of the data that is captured by the first i singular vectors. As shown in figure 4.6b, the first mode alone, the mean flow shown in figure 4.7a, accounts for over 91% of the total variance of the data. The second mode, in figure 4.7b, contributes with approximately 1.2 % of the variance, and the influence of the

subsequent modes, determined by their singular values shown in figure 4.6a, falls rapidly.

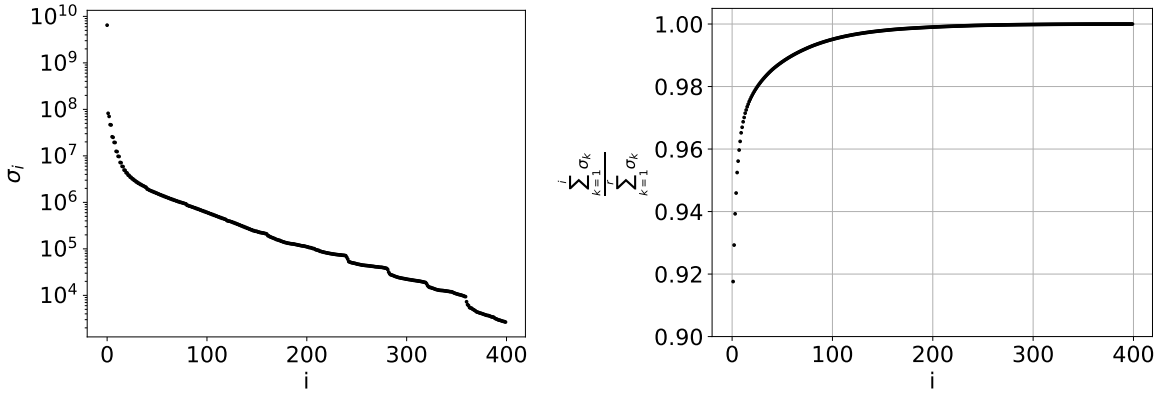

(a) Singular values

(b) Partial sum of the singular values

Figura 4.6 – Singular values of the data matrix $\mathbf{X}$.

The POD decomposed the acoustic field, generated from the propagation of the shock waves, in a mean pressure field, mode 1 in figure 4.7a, and in structures that resemble acoustic multipoles, that account for the fluctuations around that mean field. Mode 2, in figure 4.7b, is similar to a dipole, mode 4, in figure 4.7c, to a monopole and mode 10, in figure 4.7d, resembles a higher order multi-pole. However, it is important to note that the POD decomposes the data set in a set of spatially orthogonal structures, and each mode may be influenced by different frequencies.

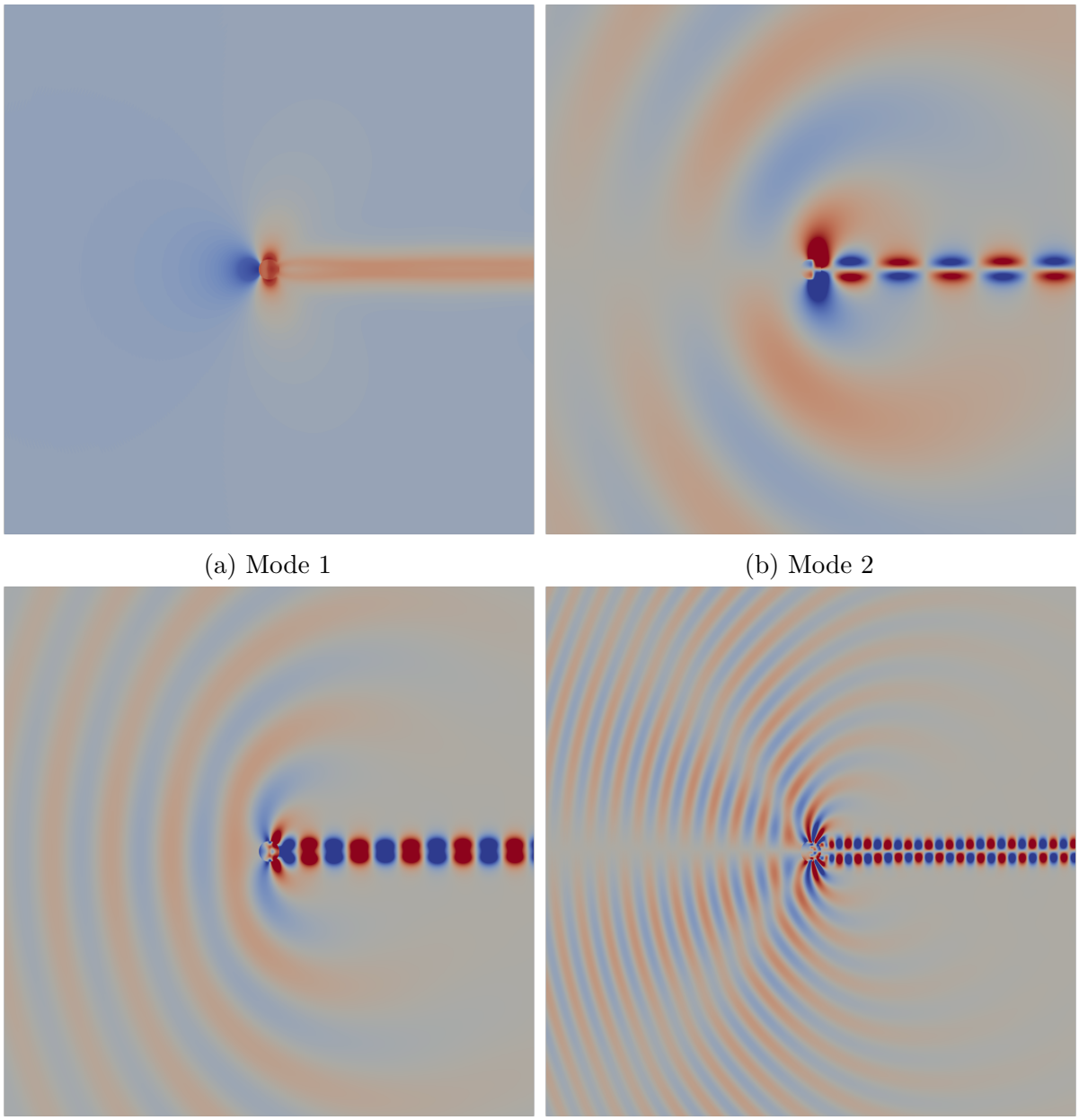

(a) Mode 1

(b) Mode 2

(c) Mode 4

(d) Mode 10

Figura 4.7 – Selected POD modes

With the POD modes, Equation 2.4 was used to reconstruct the pressure field, and the results are presented in figure 4.8. Based on the partial sum of the singular values shown in figure 4.6b, the first 21 POD modes were used for the reconstruction of the flow, as they account for over 97 % of the variance of the data set. The upwind probes in figures 4.8a and 4.8b show that the strong discontinuities are well captured, but there are small oscillations in the expansion phase of the waves, in particular on probe 5 for the lower amplitude wave that originates from the lower surface of the cylinder.

The downwind probes in figures 4.8c and 4.8d also show that the first 21 POD modes are enough to properly describe the von Kármán vortex street at the wake, as the reconstructed signals match almost perfectly those from the solution with the vat code.

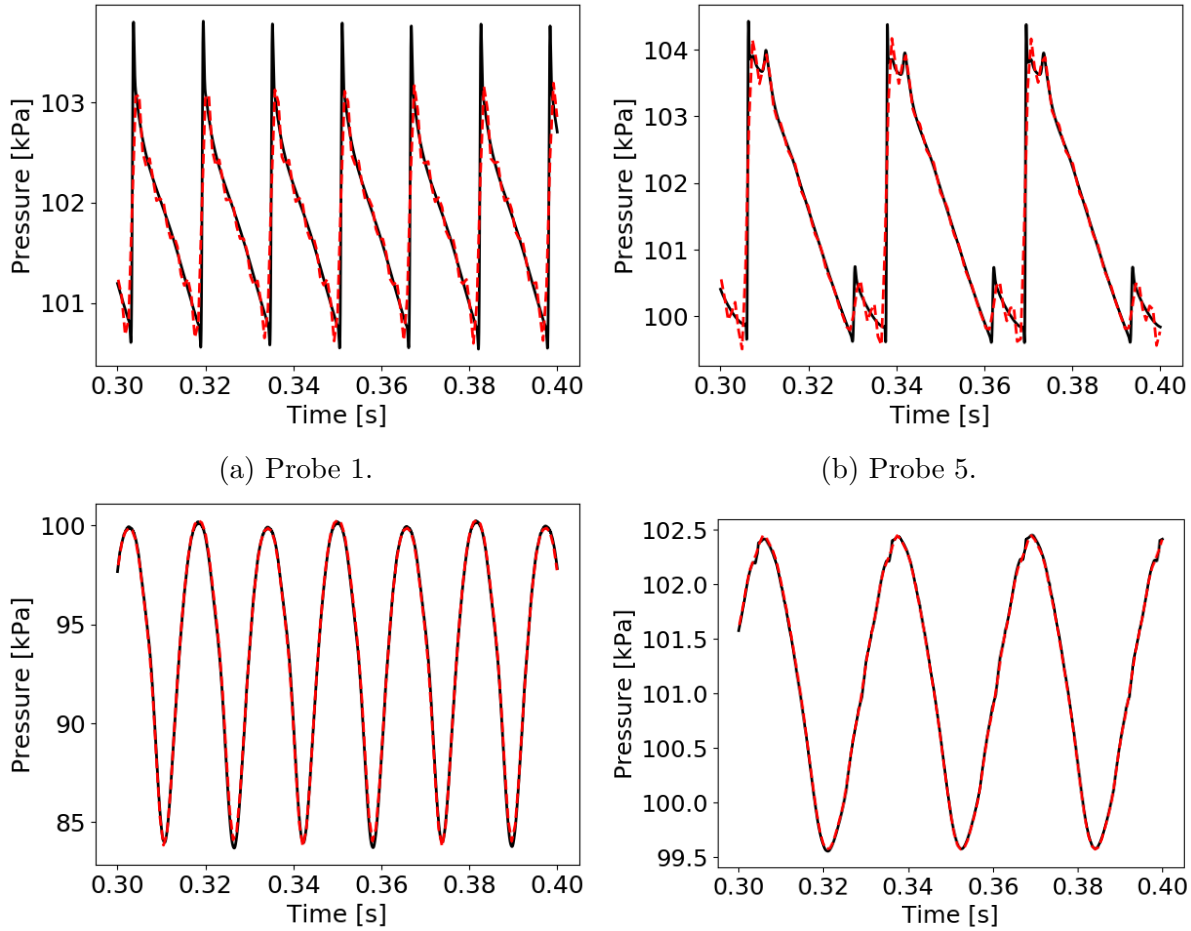

(a) Probe 1.

(b) Probe 5.

(c) Probe 7.

(d) Probe 10.

Figura 4.8 – Pressure signals. Black line: original result from the vat code. Red dashed line: Reconstruction with POD modes.

4.2.2 Dynamic Modes Decomposition

The same data set used in Section 4.2.1, consisting of 400 pressure field evaluations performed at a rate of 40 per period for 10 periods of the fundamental frequency, was decomposed with the Dynamic Modes Decomposition (DMD) method. For an initial analysis, matrix $\tilde{\mathbf{A}}$, defined in equation 2.17, was calculated through a projection on the first 21 POD modes, i.e. $r = 21$. This choice was guided by the observation, in Section 4.2.1, that the first 21 POD modes were capable of describing the flow accurately.

Figure 4.9 shows some selected DMD modes ordered from lowest to highest frequency. The DMD method, similarly to the POD, decomposed the acoustic part of the domain in structures that resemble acoustic multipoles. The first mode, in figure 4.9a, has the structure of a dipole, mode 2, in figure 4.9b, is similar to a monopole, and modes 5 and 6, shown in figures 4.9c and 4.9d, resemble higher order acoustic multipoles. The decomposition of the vortex street at the cylinder wake is consistent with results from Kutz et al. (2016) for the DMD of the incompressible flow past a cylinder, and are also similar to the Koopman modes obtained by Bagheri (2013).

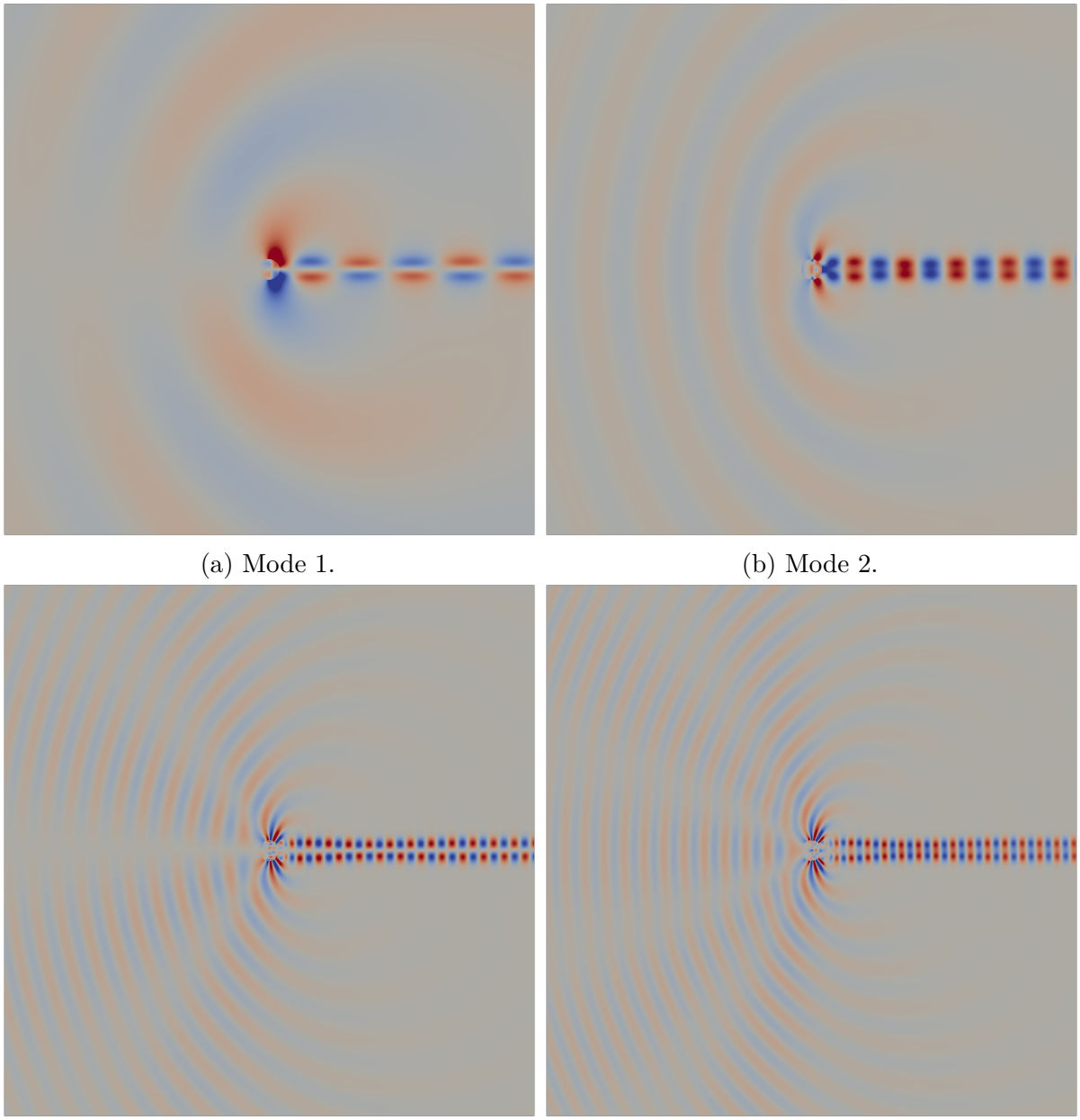

(a) Mode 1. (b) Mode 2.

(c) Mode 5. (d) Mode 6.

Figura 4.9 – Selected DMD modes.

It is interesting to note that the structures of the DMD modes are, in general, very similar to the structures of the POD modes, shown in figure 4.7. However, only the DMD modes can be associated with the temporal behaviour of the flow, as its eigenvalues provide the frequencies and rates of growth of the modes. Figure 4.10 shows the DMD eigenvalues, λ, plotted on the complex plane, along with the unit circle. The fact that all eigenvalues lie on the unit circle shows that all calculated DMD modes are marginally stable, i.e., their amplitudes remain constant with time. This is consistent with the data set, as all pressure snapshots were captured when the flow was fully established.

Figure 4.11 shows the DMD modes' frequencies f_i and rates of growth ς_i, calculated according to equations 2.20 and 2.21, respectively. Most modes present growth rates very close to zero, and the modes with the highest frequencies have negative rates, which means

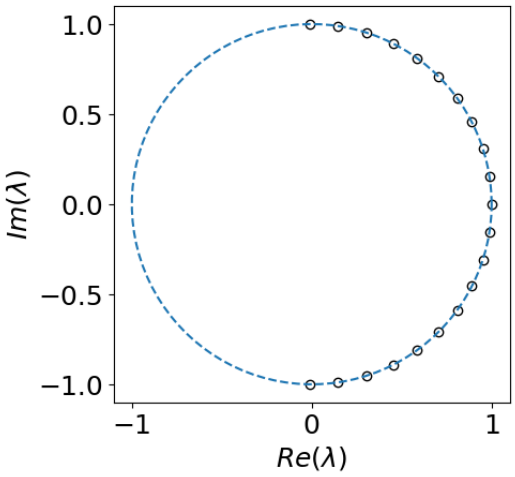

Figura 4.10 – DMD eigenvalues λ.

that these modes actually decrease in amplitude as time advances.

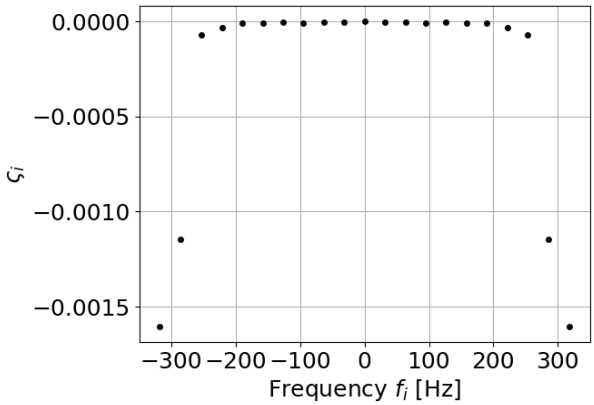

Figura 4.11 – DMD frequencies and rates of growth

To obtain a better interpretation of the DMD modes and their relation to the dynamics of the flow, the frequencies of the modes were plotted, as red vertical dashed lines, with the spectra from the pressure signals, and the result is presented in figure 4.12. It is possible to observe that the first DMD mode, shown in figure 4.9a, is directly related to the fundamental frequency of the flow, and each subsequent mode corresponds to one of its harmonics. This is consistent with the fact that the flow is periodic with only one frequency.

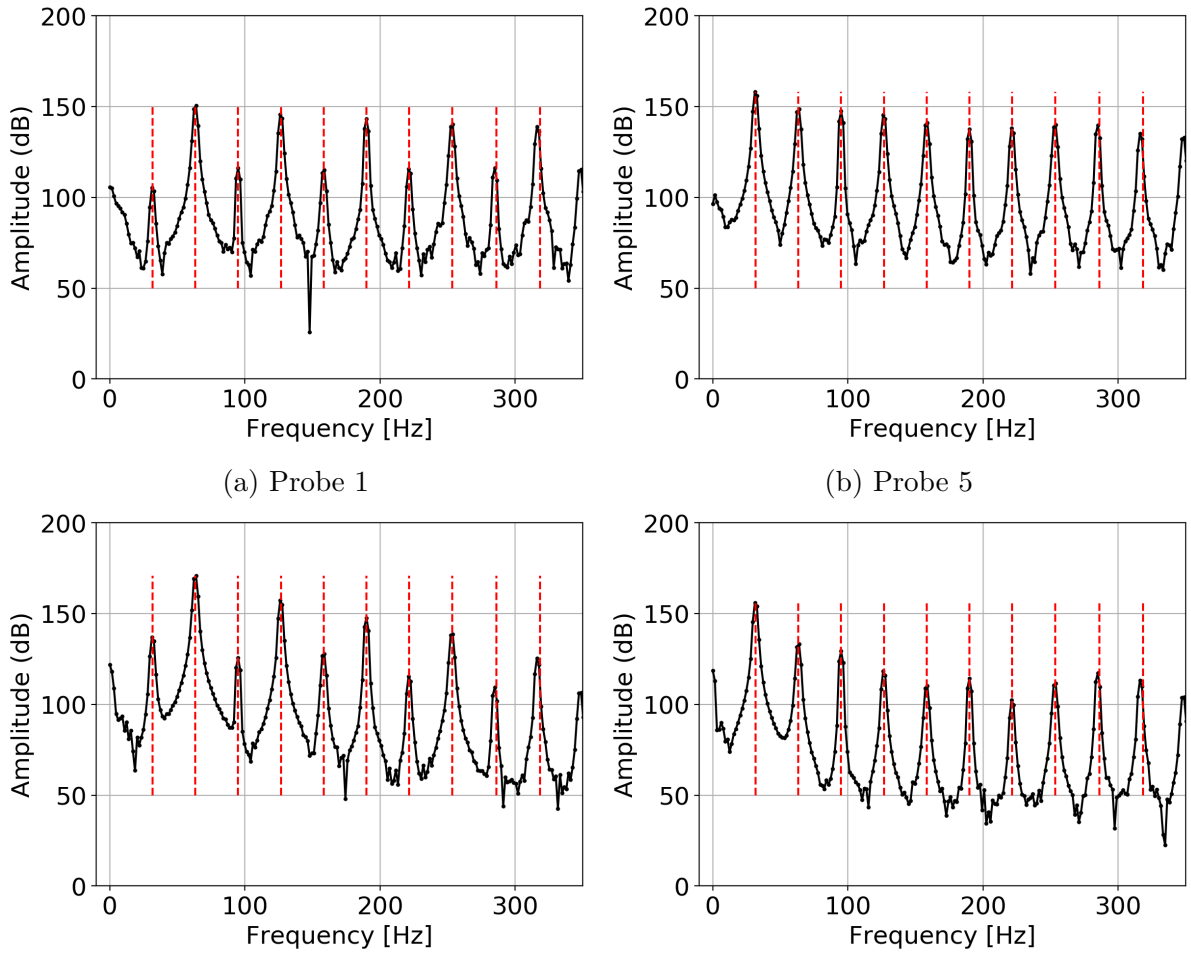

(a) Probe 1

(b) Probe 5

(c) Probe 7

(d) Probe 10

Figura 4.12 – Fourier transform of the pressure signal at different probes. The red dashed vertical lines represent the frequencies of the DMD modes obtained for $r = 21$. $M_\infty = 0.5$

4.2.3 Flow reconstruction with the DMD modes

The DMD modes and eigenvalues were used to reconstruct the flow, using equation 2.22, and figure 4.13 presents the results, in red dashed lines, compared to the original pressure signals, in black lines, obtained with the vat code.

The DMD reconstruction was able to properly describe the discontinuities of the pressure waves that propagate upwind, as shown in figures 4.13a and 4.13b, but there is a considerable error in the signals. The expansion phase at probe 1 was basically not described at all, and the lower pressure peak at probe 5 was not captured. The reconstruction at probe 7, shown in figure 4.13c, located inside the vortex wake and very close to the cylinder, also had a significant error. In addition to the discrepancies in phase and mean value, the shape of the reconstructed wave was also not described correctly. The original pressure signal has a more abrupt variation in the low-pressure points, while the reconstructed signal varies more smoothly. This difficulty for the DMD to describe the flow at the wake near the cylinder might be a consequence of the complexity of the

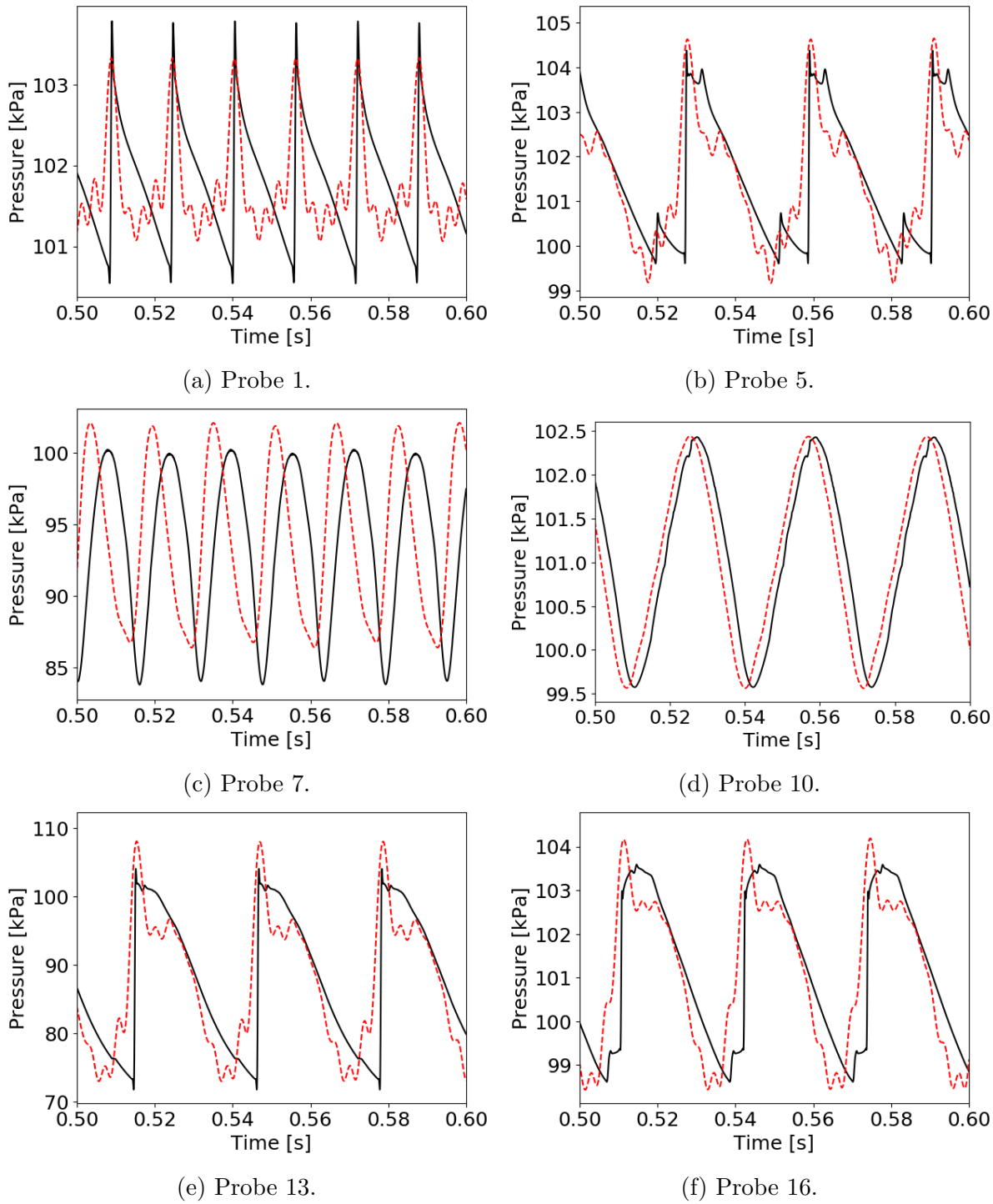

(a) Probe 1.

(b) Probe 5.

(c) Probe 7.

(d) Probe 10.

(e) Probe 13.

(f) Probe 16.

Figura 4.13 – Pressure signals. Black lines: original signal from the vat code. Dashed red lines: DMD reconstruction.

flow in this region, with high-pressure variations that are not properly captured with the DMD's linear approximation. Probe 10, shown in figure 4.13d, had the best agreement between the original and reconstructed signals, with a small phase shift and an acoustic perturbation in the high-pressure region of the wave not captured by the DMD. The DMD was also able to capture the discontinuities at the top of the cylinder, at probes 13 and 16, shown in figures 4.13e and 4.13e. The expansion phase of these signals also presented some errors but there is a much better agreement with the original data than the results from the upwind probes.

Overall, the comparison of the original and the reconstructed signals in the probes showed that the DMD reconstruction can capture the frequency and the amplitude of the pressure fluctuations, but is unable to properly describe the shape of the waves, especially in the more complex regions of the flow. To evaluate the DMD reconstruction of the flow over the entire domain, the instantaneous, relative error was calculated as

$$E = 100 \times \frac{|p - p_{dmd}|}{p},$$

where E is the error, p is the original pressure value and p_{dmd} is the pressure calculated with the DMD modes. Figure 4.14 shows the resulting error.

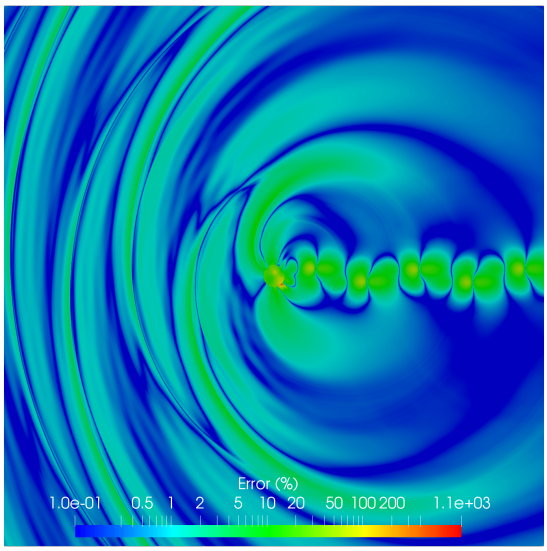

Figura 4.14 – Relative error for the instantaneous flow reconstructed with the DMD modes.

The relative error at the entire domain mostly confirms the observations made with the pressure signals at the probes. From the acoustic region, we can see that the discontinuities are well captured, with an error close to 1%. In the subsequent expansion, however, the error grows to about 20%. At the vortex street, the error is considerable and gets as high as 100% at certain points. This can be explained by the phase and mean value error, shown in figure 4.13c. At the downwind region outside the wake, the error is, in general, smaller, as in this region the flow is less complex, without large pressure

fluctuations or discontinuities. The largest error, of over 1,000%, is at the region close to the cylinder wall, just before the shock wave, where the flow is locally supersonic.

Even though the analysis of the instantaneous error revealed many aspects of the difference between the original and the reconstructed flows, the phase shift observed in probe 7 and, to a lesser extent, probe 10, had an important contribution to the instantaneous error but is far less relevant to an analysis of the intensity of the generated noise. With that in mind, the DMD modes were used to generate a new set of snapshots for the pressure field, and this set was then used to calculate a reconstructed Sound Pressure Level field, using equation 4.1. The error, in decibels, between this reconstructed SPL field and the original, shown in figure 4.5, was calculated as

$$E_{dB} = |SPL - SPL_{DMD}|\,,$$

where E_{dB} is the error, SPL is the original Sound Pressure Level, and SPL_{DMD} is the Sound Pressure Level calculated with the pressure fields reconstructed with the DMD modes. The resulting error is shown if Fig. 4.15.

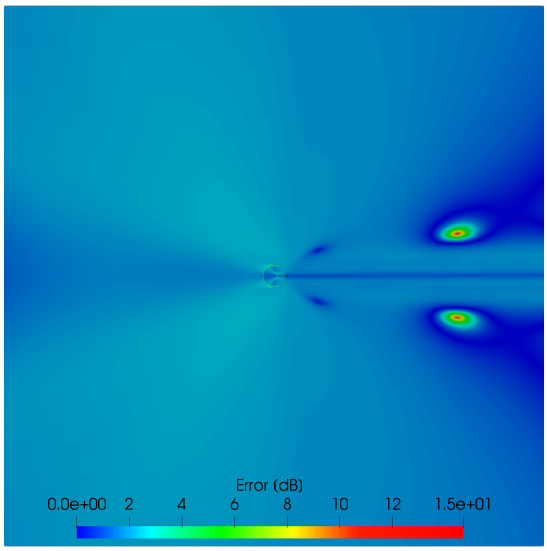

Figura 4.15 – Error for the Sound Pressure Level field reconstructed with the DMD modes.

The error over most of the domain was around 2.5 dB, including the wake region, where the instantaneous error got over 100% at certain points. However, the DMD was unable to capture the two regions of silence above and below the wake shown in figure 4.5. The DMD reconstruction actually overestimated the Sound Pressure Level in these regions by about 10 dB.

Although the error for the Sound Pressure Level is relatively small in most of the flow field, of about 2 dB when the original SPL is close to 150 dB, it is important to notice that the Sound Pressure Level scale is logarithmic. Therefore, a change of 2 dB actually corresponds to a significant increase in sound intensity. With that in mind, the relative

error for the root mean square value of the pressure fluctuations (p'_{rms}) was calculated as

$$E_{rms} = 100 \times \frac{|p'_{rms} - p'_{rmsDMD}|}{p'_{rms}},$$

where E_{rms} is the relative error, p'_{rms} is the original pressure root mean square value and p'_{rmsDMD} is the pressure root mean square value calculated with the same set of reconstructed pressure fields used for the SPL error calculation. The result is depicted in figure 4.16.

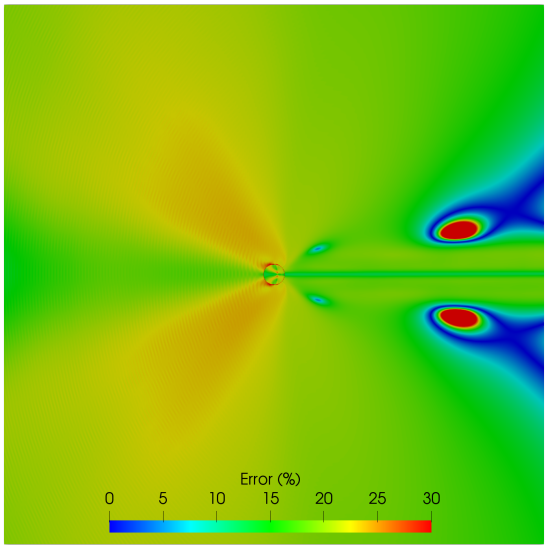

Figura 4.16 – Relative error for the p'_{rms} field reconstructed with the DMD modes.

For most of the flow field, the resulting error varies from approximately 15% to 25%. The error is only higher than 30% near the wall of the cylinder and in the silence regions near the wake, where the maximum error gets above 200%. These values for the error are consistent with the results for the instantaneous error, from figure 4.14, and give a better understanding of the difference between the original flow and the DMD reconstruction when compared to the SPL error.

When compared to the flow reconstruction with the POD modes, these results show that while the DMD analysis provides relevant information regarding the temporal behaviour of the flow, the POD is a better tool for the reconstruction of the flow field. It is important to highlight, however, that equation 2.22, used for the DMD reconstruction, is continuous in time, while equation 2.4, used for the POD reconstruction, is discreet in time. This means that, given an initial condition, the DMD method allows for the reconstruction of the flow field at any instant in time, while the POD mode is only capable of reconstructing the flow at the time instants in which the snapshots were captured.

The next sections present a series of qualitative studies of the DMD reconstruction. First, equation 2.23 was used to reconstruct the flow using matrix $\tilde{\mathbf{A}}$ and a projection

of the initial condition on the left singular vectors. In sequence, the Mach number field was appended to the pressure snapshots to verify if the reconstruction results improve. After that, the reconstruction was performed with different data sets. At last, the relation between the quality of the reconstruction and the number of DMD modes used was studied.

Reduced order linear equation

An alternative to the reconstruction of the flow with the DMD modes and eigenvalues (equation 2.22) is to use equation 2.23, $\tilde{\mathbf{x}}_{k+1} = \tilde{\mathbf{A}}\tilde{\mathbf{x}}_k$. This equation consists of the projection of the linear approximation $\mathbf{X}' \approx \mathbf{AX}$ on a basis formed by the first r left singular vectors, $\mathbf{U}_1^r$, which results in a reduced order linear equation that approximates the linear system. The resulting reconstruction is presented in figure 4.17.

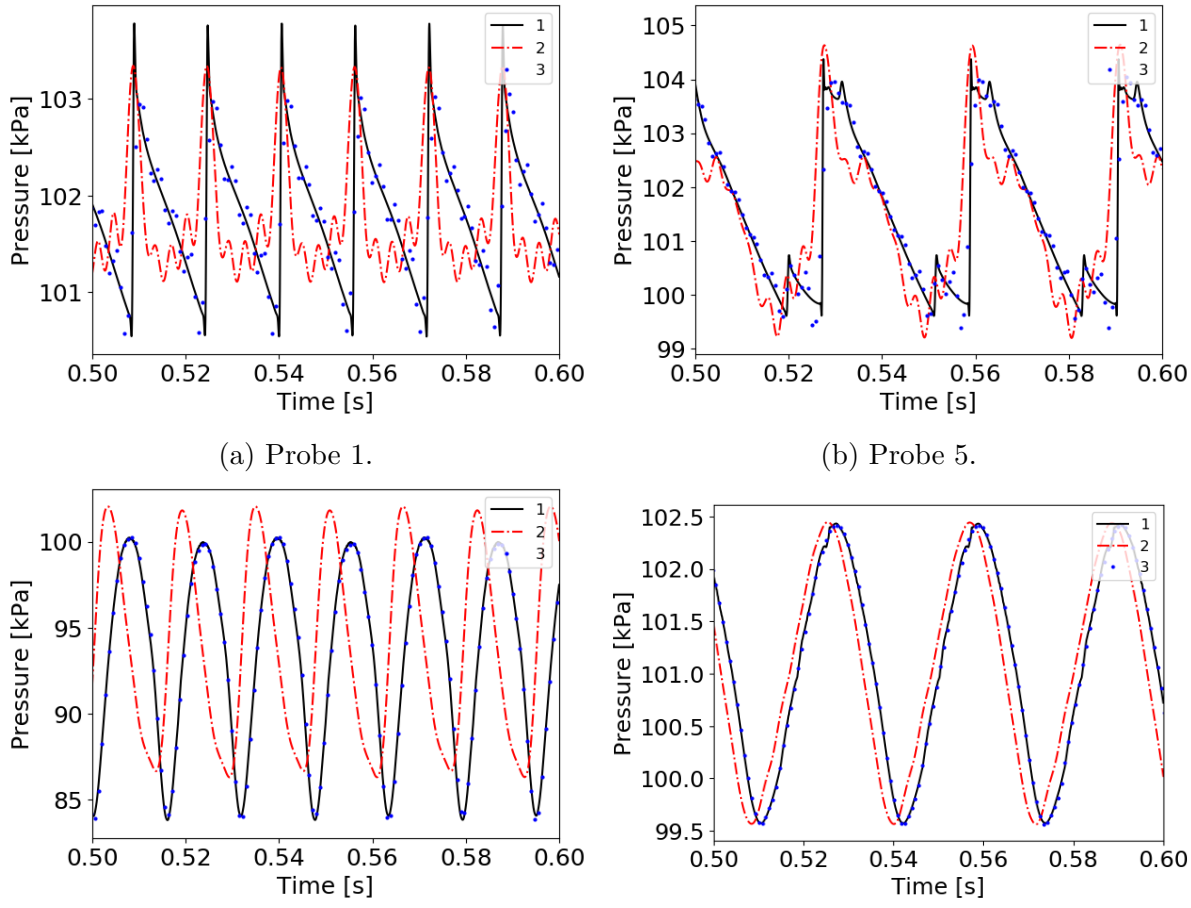

(a) Probe 1.

(b) Probe 5.

(c) Probe 7.

(d) Probe 10.

Figura 4.17 – Flow reconstruction. 1 - Original signal from the vat code. 2 - Reconstruction with DMD modes. 3 - Reconstruction with the projection on the left singular vectors.

The results from this method had a much better agreement with the original data when compared to the reconstruction with the DMD modes. The upwind probes, in figures 4.17a and 4.17b, show that there is some oscillation in the expansion phase of the waves, but the overall shape of the wave is preserved. At the downwind region, represented by probes 7 and 10 shown in figures 4.17c and 4.17d, the reconstruction matches the original

data almost perfectly, without the phase, shape and mean value errors observed in the reconstruction with the DMD modes. However, in a similar manner to the POD, this method is only capable of calculating the reconstruction at the time instants in which the snapshots were created.

This approach and the traditional DMD reconstruction with equation 2.22 are very similar, as both use the same matrix $\tilde{\mathbf{A}}$ obtained from the DMD method. The main difference is that the latter involves a transformation from a discrete time domain to continuous when we write $\omega_k = \ln(\lambda_k)/\Delta t$, in a sort of bilinear transformation. This might introduce phase errors in the modes that prevent the continuous time reconstruction from matching the original data and is a possible reason for the better agreement between the reconstruction with the discrete equation and the data seen in figure 4.17.

Snapshots with pressure and Mach number

The results for the DMD presented so far were obtained with pressure field snapshots given by

$$\mathbf{x}_k = \begin{bmatrix} p(1,1,t_k) \\ p(1,2,t_k) \\ \vdots \\ p(1,n_y,t_k) \\ p(2,1,t_k) \\ \vdots \\ p(n_x,n_y,t_k) \end{bmatrix}, \tag{4.2}$$

where n_x and n_y are the dimensions of the domain and t_k is the time instant for snapshot $\mathbf{x}_k$. However, it is possible to include more variables in the snapshots.

When applied to data from compressible flows, the POD snapshots are often formed by pressure and velocity data (HOLMES et al., 2012). Seid et al. (2012) also mentions the importance of including thermodynamic and kinematic data on the snapshots for DMD of a compressible flow and used velocity and the inner product of the pressure and enthalpy fields. To prevent the memory requirements from growing excessively, we decided to use pressure and Mach number data for the snapshots, as it still contains thermodynamic and

kinematic information. The DMD was then applied to snapshots given by

$$x_k = \begin{bmatrix} p(1,1,t_k) \\ p(1,2,t_k) \\ \vdots \\ p(1,n_y,t_k) \\ p(2,1,t_k) \\ \vdots \\ p(n_x,n_y,t_k) \\ M(1,1,t_k) \\ M(1,2,t_k) \\ \vdots \\ M(1,n_y,t_k) \\ M(2,1,t_k) \\ \vdots \\ M(n_x,n_y,t_k) \end{bmatrix}, \tag{4.3}$$

and the flow reconstruction results are presented in Figure 4.18.

The use of the Mach number resulted in slight improvements to the reconstruction of the flow, especially in the expansion region of the waves shown in figure 4.18a and in the phase error seen in figure 4.18c. However, this difference is small for most of the flow reconstruction, while the memory requirement is twice as big as when only the pressure is used.

Different data-sets

The results presented in the previous sections were obtained with a data set composed of snapshots sampled at a rate of 40 per period for 10 periods. To investigate the influence of the data set on the reconstruction with the DMD modes, two new data sets were used. The first had a rate of 20 snapshots per period for 20 periods, and the second had a rate of 10 per period for 40 periods. Therefore, all sets had 400 snapshots and the objective is to determine the best way to distribute them over the time series. Figure 4.19 depicts the reconstructed signals at some probes.

It is difficult to draw conclusions from the reconstruction of the upwind region of the flow, seen in figures 4.19a and 4.19b without a more objective error estimation, as neither new data set provides a significantly better result. A qualitative analysis shows that the use of 10 snapshots per period for 40 periods (green dotted lines) results in more oscillation in the expansion phase of the waves, while the use of 20 per period for 20 periods (blue dashed lines) has very similar results to the original data-set of 40 per period for 10 periods (red dash-dot lines). The downwind probes seen in figures 4.19c and 4.19d, on the other hand, show a clear difference between the analysed cases. The use of 20

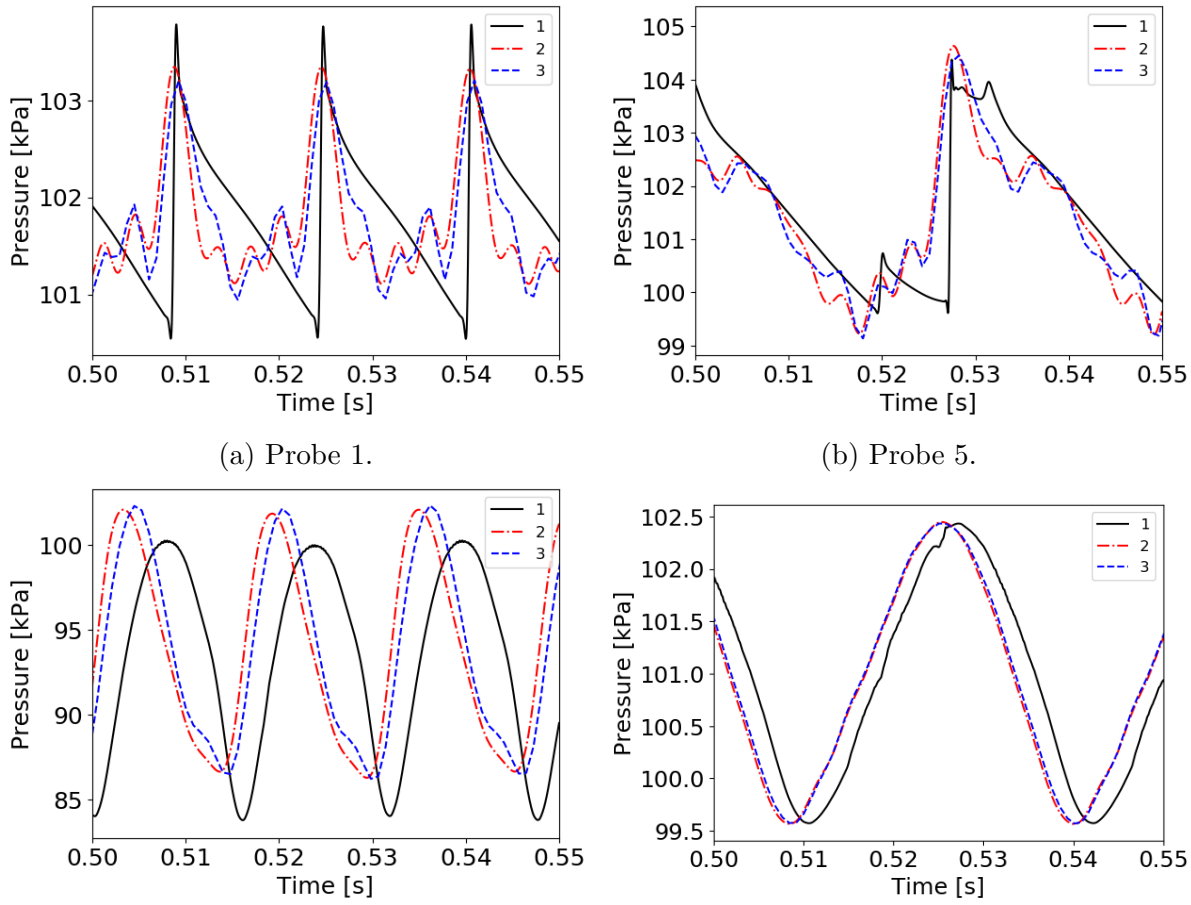

(a) Probe 1.

(b) Probe 5.

(c) Probe 7.

(d) Probe 10.

Figura 4.18 – Flow reconstruction. 1 - Original signal from the vat code. 2 - Reconstruction with DMD modes with pressure snapshots. 3 - Reconstruction with DMD modes with pressure and Mach number snapshots.

snapshots per period resulted in smaller phase and mean value errors and a wave format more similar to the original when compared to the original results with 40 snapshots per period, while the use of 10 snapshots per period resulted in larger errors. These results show that the reconstruction depends directly on the chosen data set, and to obtain a better reconstruction of the flow, it is necessary to find a balance between the sampling rate and the total time covered by the data.

Number of DMD modes

The number of DMD modes was the final parameter used in the investigation of possible strategies for improving the flow reconstruction. The original results were obtained with $r = 21$ modes, and a new set of 51 DMD modes was generated. The resulting flow reconstruction is presented in figure 4.20.

Figure 4.20a shows that the use of 51 modes resulted in more oscillations, with larger amplitudes, in the expansion phase of the waves. The reconstruction with 51 modes also resulted in higher pressure peaks in the signals from the upwind probes, and at probe 5

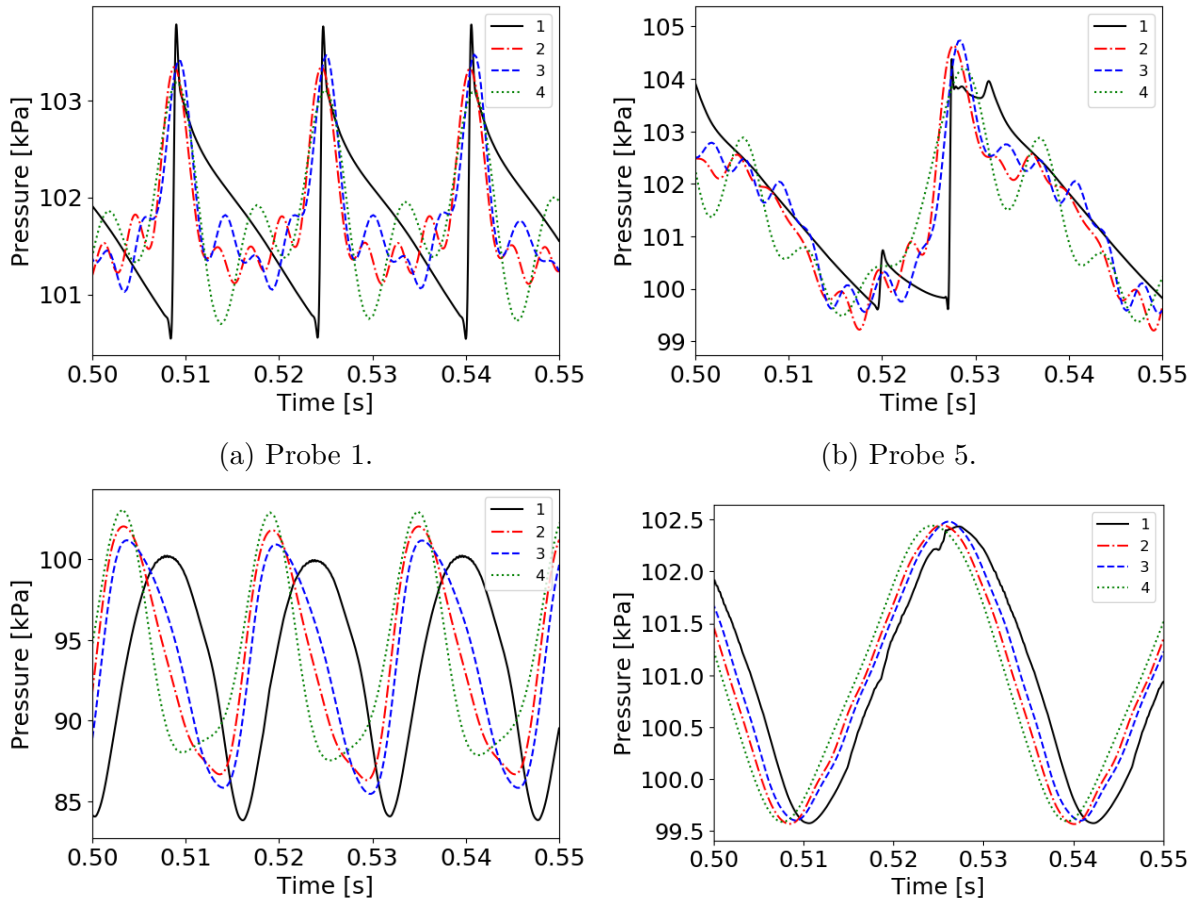

(a) Probe 1.

(b) Probe 5.

(c) Probe 7.

(d) Probe 10.

Figura 4.19 – Flow reconstruction with DMD modes. 1 - Original signal from the vat code. 2 - 40 snapshots per period for 10 periods. 3 - 20 snapshots per period for 20 periods. 4 - 10 snapshots per period for 40 periods.

(figure 4.20b) the reconstructed signal had a significantly higher amplitude when compared to the result from the vat code. At downwind probes, shown in figures 4.20c and 4.20d, there was no relevant difference between the two reconstructed signals. This is consistent with an observation made by Kutz et al. (2016) that it is not always better to use more DMD modes for the reconstruction.

4.3 Mach 0.75

The flow around the cylinder with a Mach number of 0.75 is illustrated in figure 4.21, with different properties. Figure 4.21a shows the pressure field, figure 4.21b, the visualisation variable β_T, figure 4.21c, the Mach number and figure 4.21d shows the vorticity field.

The fundamental dynamics of the flow with $M_\infty = 0.75$ is similar to that of the flow with $M_\infty = 0.5$, discussed in section 4.2. As the flow passes through the cylinder, it is accelerated until it reaches supersonic speed, as indicated by the black contour lines for $M = 1.0$ in figure 4.21c. When the shock waves decelerate the flow back to a subsonic

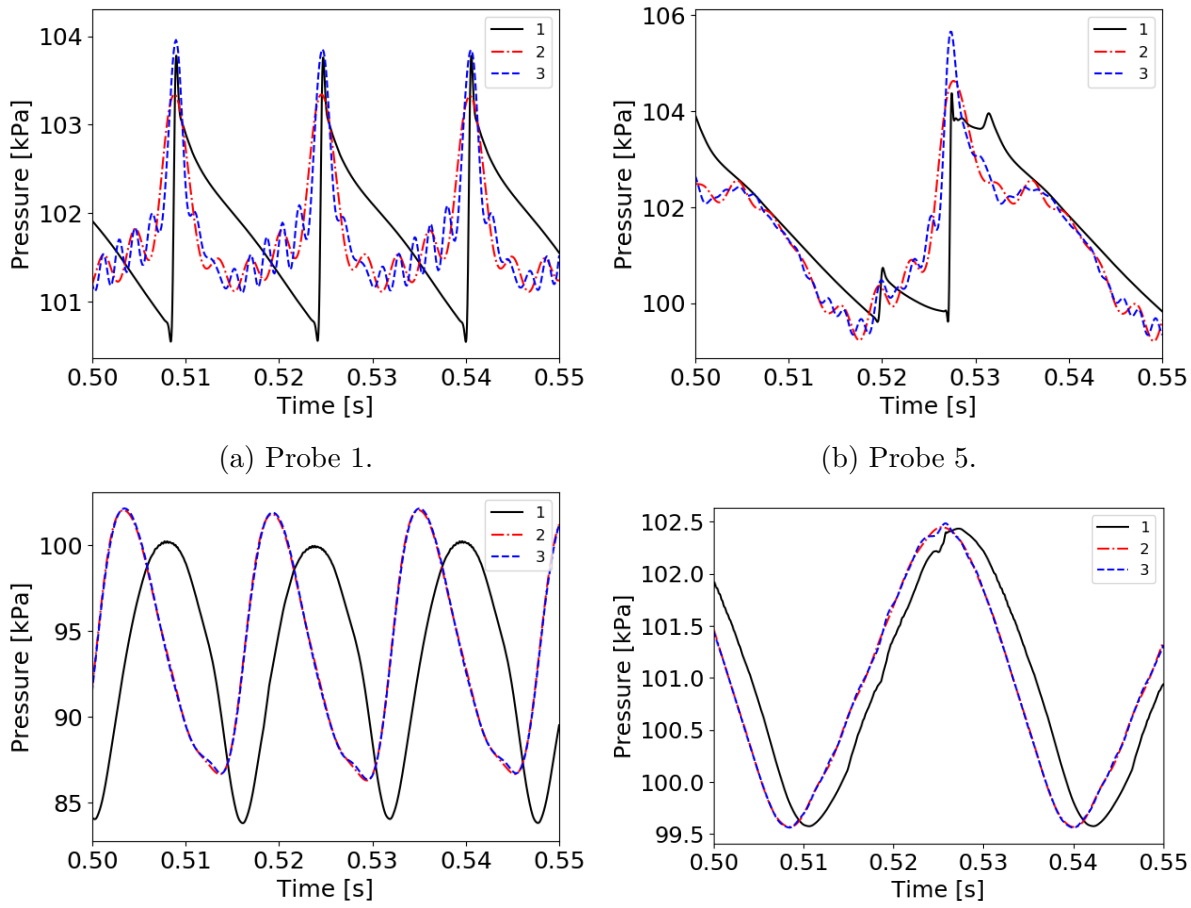

(a) Probe 1.

(b) Probe 5.

(c) Probe 7.

(d) Probe 10.

Figura 4.20 – Flow reconstruction with DMD modes. 1 - Original signal from the vat code. 2 - 21 DMD modes. 3 - 51 DMD modes.

condition, the associated adverse pressure gradient causes the separation of the flow and the formation of a vortex street at the wake. An interesting difference from the case of $M_\infty = 0.5$ is that, as figure 4.21c shows, there are supersonic regions inside the vortex street, caused by the combination of the tangential and advective velocities of the vortices. As a consequence, shock waves appear and there is noise emission from the wake, seen on the β_t field. A video of the temporal evolution of the β_T field is available here.

Figure 4.21d shows how vorticity is generated through the baroclinic effect and is transported by the flow. As the solution for the flow was obtained with the Euler equations, there is no dissipation of vorticity, as the model does not include viscosity.

Associated with the flow separation is the emission noise due to the detachment of the shock waves. The pressure and β_T images show how the propagation of these sound waves is influenced by flow, i.e., the Doppler effect. When sound propagates upwind, the mean flow has the effect of reducing the resultant propagation speed, and the wave fronts get closer to each other. When the sound waves propagate downwind, on the other hand, the mean flow has the effect of increasing the propagation speed, and the distance between consecutive wavefronts gets bigger.

The greater complexity of the flow with $M_\infty = 0.75$ is also reflected in the pressure

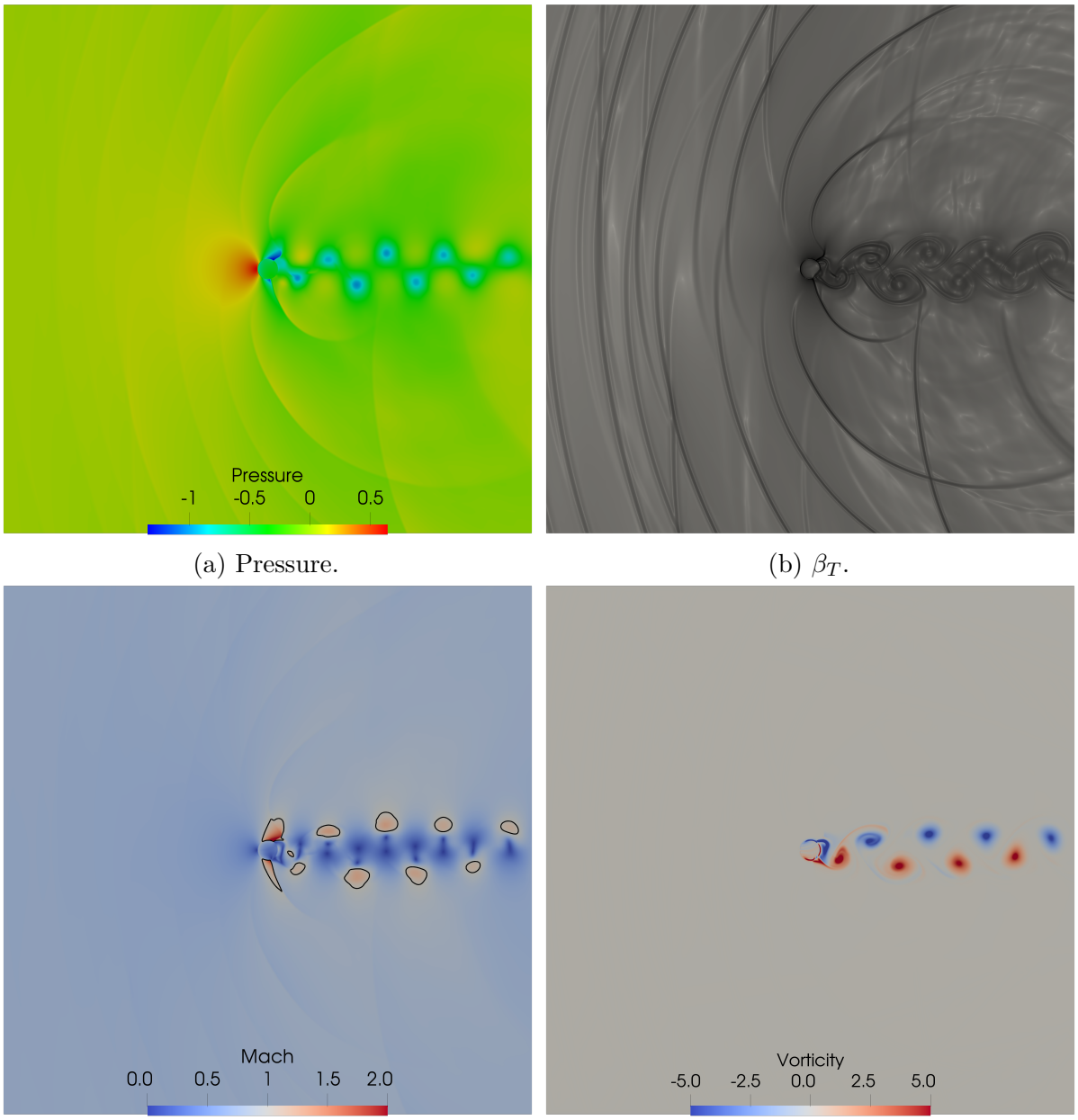

(a) Pressure.

(b) β_T.

(c) Mach number.

(d) Vorticity.

Figura 4.21 – Flow visualisation, $M_\infty = 0.75$

signals depicted in figures 4.22 to 4.24, acquired from the measurement probes shown in the diagram on figure 3.1. The upwind probes in figure 4.22 show the same discontinuities at the compression phase of the waves, but the periodicity seen with $M_\infty = 0.5$ is not present. Not only there are significant changes in amplitude, but also there are lower and higher frequency effects.

The downwind probes in figure 4.23 also show how the flow is more complex and not periodic. The signal from probe 7, located inside the vortex wake, shows what appears to be a lower-frequency modulation of the higher-frequency oscillations (figure 4.23a). Probe 7 also shows the shock waves that appear because the flow at some regions is locally supersonic, a behaviour that was absent from the flow with $M_\infty = 0.5$.

The probes located above the cylinder, shown in figure 4.24, reinforce the obser-

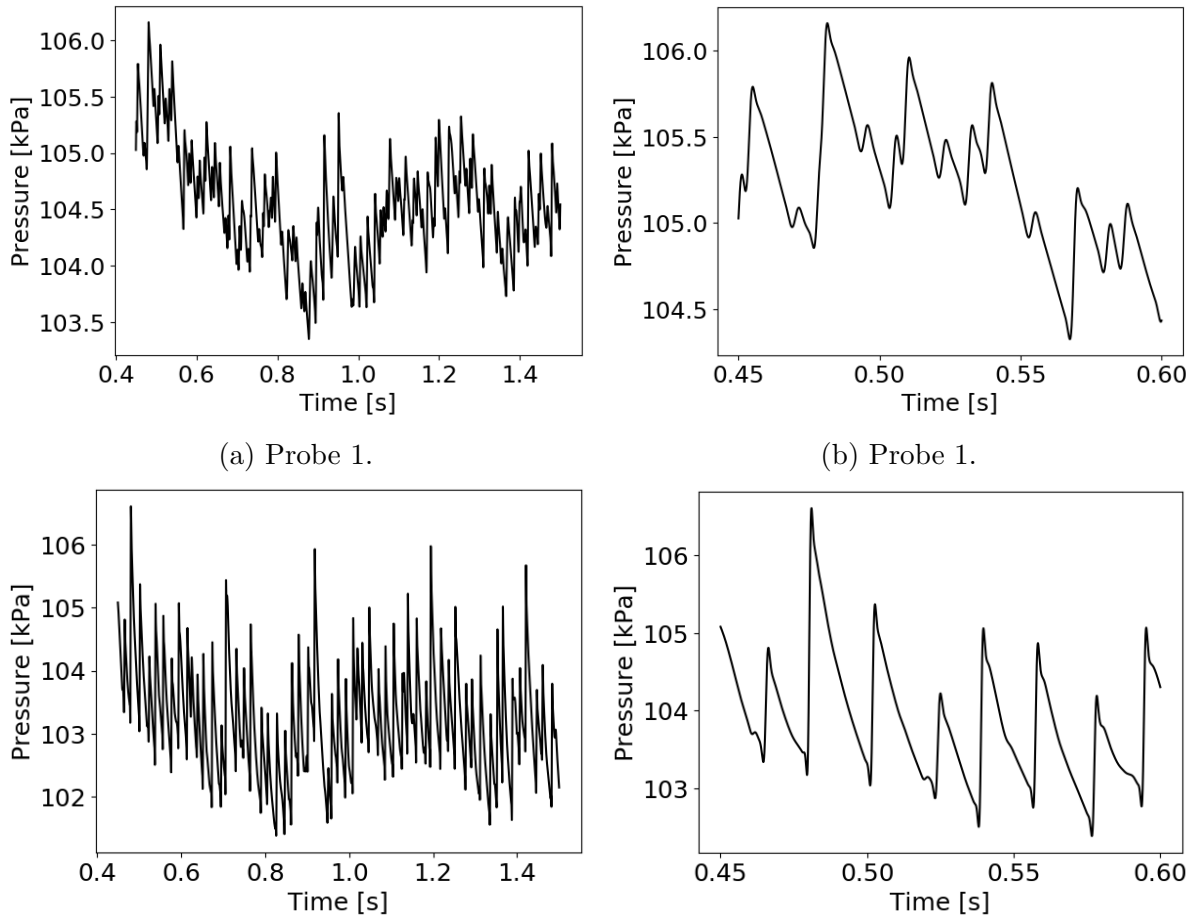

(a) Probe 1.

(b) Probe 1.

(c) Probe 5.

(d) Probe 5.

Figura 4.22 – Pressure signals at the upwind probes.

vations made from the downwind and upwind probes. The signals also present strong variations in amplitude, in addition to influence from multiple frequencies.

The pressure spectra depicted in figure 4.25 provide further confirmation about the complexity of the flow. Probes 1, 5, 7, 10 and 16 all show a peak close to $St = 0.2$, the expected value for the flow around the cylinder (BOTTA, 1995). The spectra from probes 7 and 16 also show the first harmonic of this frequency, at $St = 0.4$. However, there are many other relevant frequencies in the signals. The spectra for the upwind probes show peaks around Strouhal numbers 0.006, 0.025, 0.07, and 0.13 and a smaller peak at 0.27. These lower frequency components are consistent with the signals from figure 4.22.

Probe 7, located downwind and inside the vortex street, also shows the lower-frequency peaks at $St = 0.006$ and 0.025, but in addition to $St = 0.2$, there is an important peak at 0.21, and at around 0.27 there are several close peaks with high amplitude, which means that higher frequency effects at the wake are important. At this position, there is also the first harmonic for $St = 0.2$ and a close peak at $St = 0.33$. At probe 10, located downwind and above the wake, there is no relevant content at Strouhal numbers above the fundamental value of $St = 0.2$, but there are several peaks around 0.13 with significant amplitudes. We can then conclude that higher frequency effects are more present inside

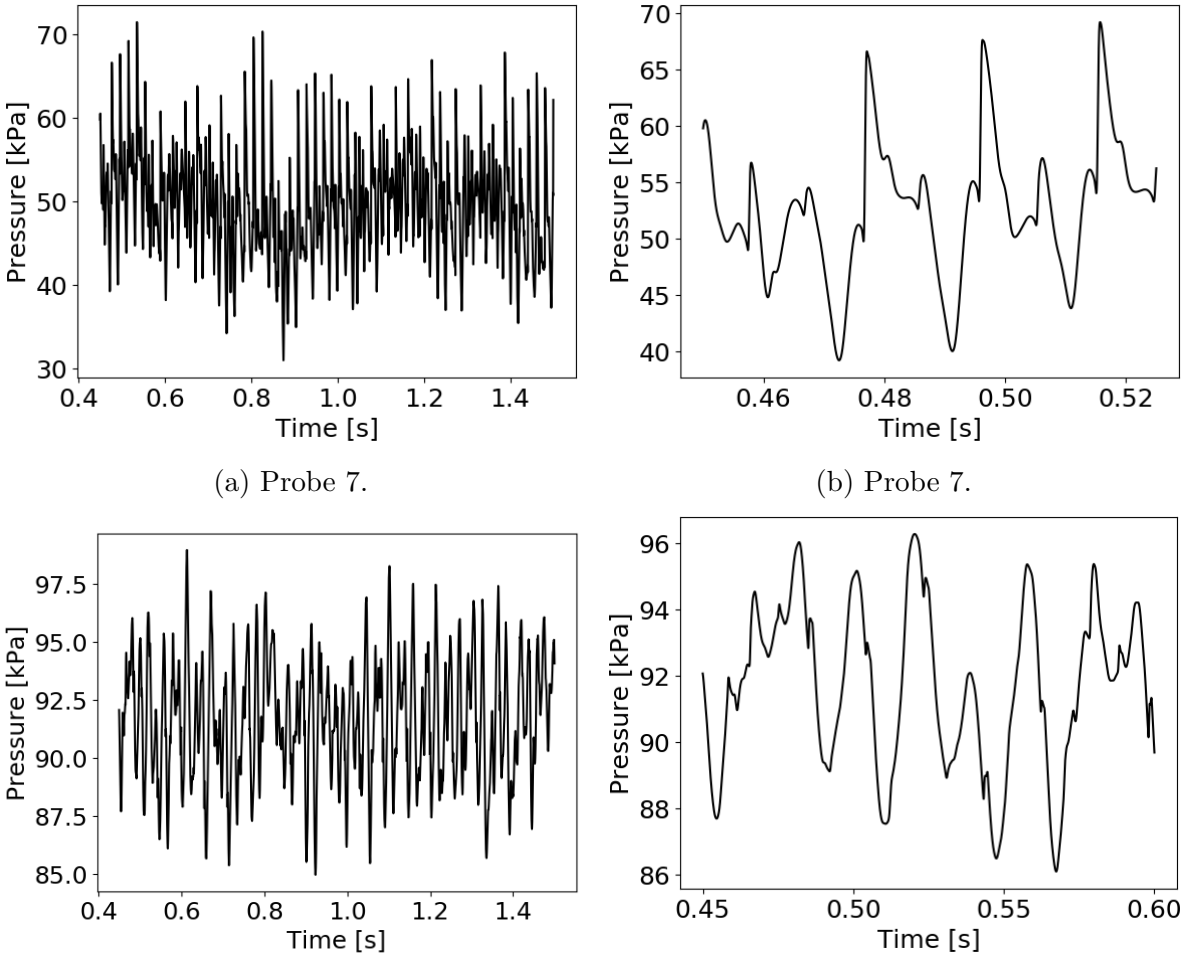

(a) Probe 7.

(b) Probe 7.

(c) Probe 10.

(d) Probe 10.

Figura 4.23 – Pressure signals at the downwind probes.

the vortex wake, while lower frequency contributions are more important outside the wake.

The spectrum for probe 13, located above the cylinder, has a very dominant peak at $St = 0.007$, and smaller peaks at 0.07 and around 0.13 and 0.2. This is consistent with the lower-frequency oscillation shown in figure 4.24a. At probe 16, the peaks for $St = 0.2$ and its harmonic at $St = 0.4$ return. The spectrum also shows the lower frequency peaks at $St = 0.007$, 0.025, 0.07 and around 0.13, which also appear at the upwind probes, and, with smaller amplitudes, peaks at $St = 0.27$ and 0.33.

Figure 4.26 shows the Sound Pressure Level field for the flow with $M_\infty = 0.75$, calculated with equation 4.1. The SPL field shows the influence of the flow on the propagation of sound, which results in a region of relative silence upwind and causes the higher-intensity regions above and below the cylinder to incline towards the downwind region. It is also possible to see, through the contour lines, a break in symmetry in the downwind region as a consequence of the greater complexity of the flow, a result also reported by Botta (1995).

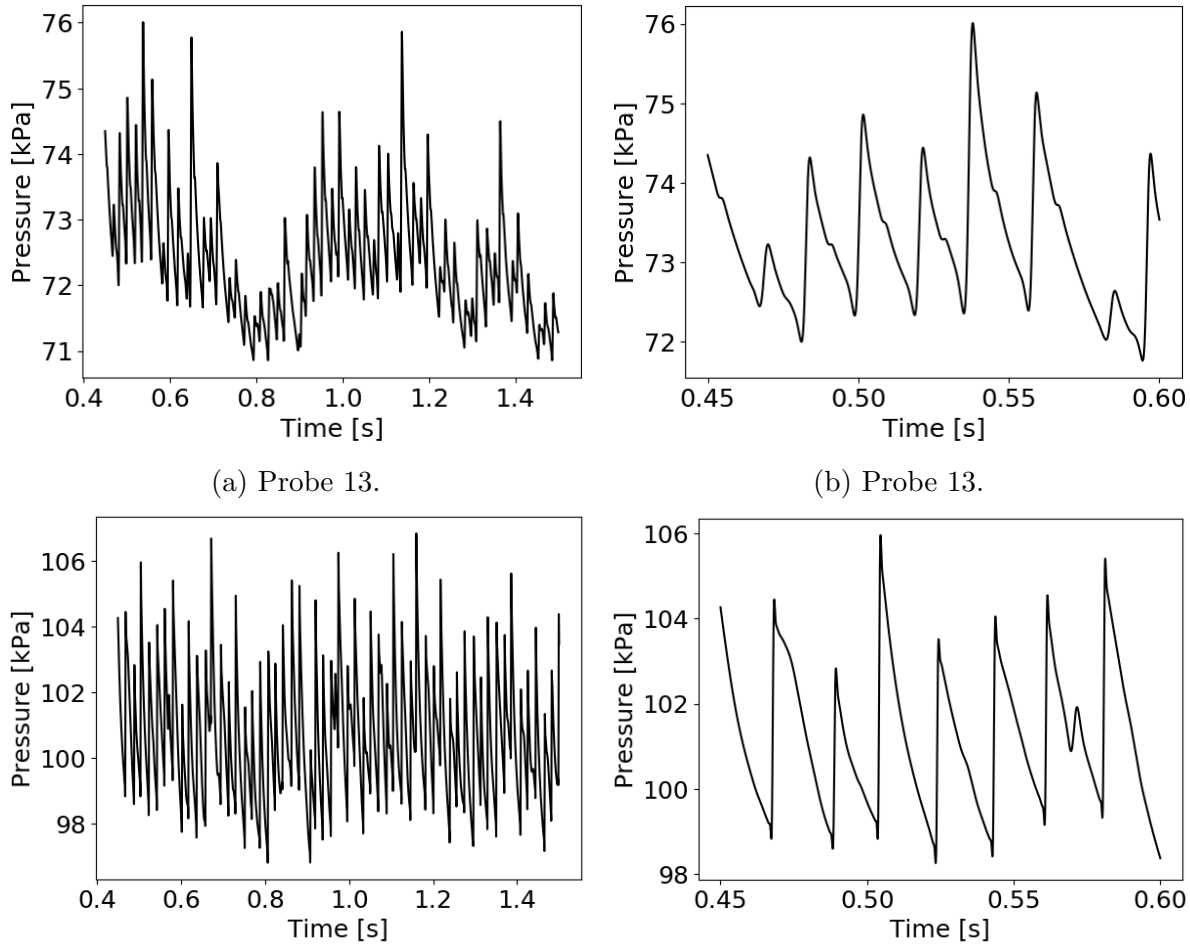

(a) Probe 13.

(b) Probe 13.

(c) Probe 16.

(d) Probe 16.

Figura 4.24 – Pressure signals at the probes above the cylinder.

4.3.1 Proper Orthogonal Decomposition

The results from the simulation of the flow around a cylinder with $M_\infty = 0.75$ were decomposed with the Proper Orthogonal Decomposition (POD) method. The data set used for the decomposition was generated by evaluations of the pressure field at a rate of 80 samples per period over a period of time corresponding to 10 periods, using the frequency $St = 0.2$ as a reference. The sampling rate was increased, in comparison to the case with $M_\infty = 0.5$, to ensure the higher frequency effects shown in the spectra are properly captured.

Figure 4.27 shows the calculated singular values, and figure 4.28 shows some selected POD modes. Again, the modes are numbered according to their corresponding singular values, ordered from highest to lowest. As explained in section 4.2.1, the partial sum in figure 4.27b represents the fraction of the variance captured by the first i modes. It is interesting to notice that the first mode, the mean flow shown in figure 4.28a, accounts for only about 20% of the variance, while the first mode for $M_\infty = 0.5$ accounted for more than 91%. In addition, the second mode, in figure 4.28b, contributes with about 7%, while for $M_\infty = 0.5$, it contributed with 1.2%. This illustrates how the flow with $M_\infty = 0.75$ is

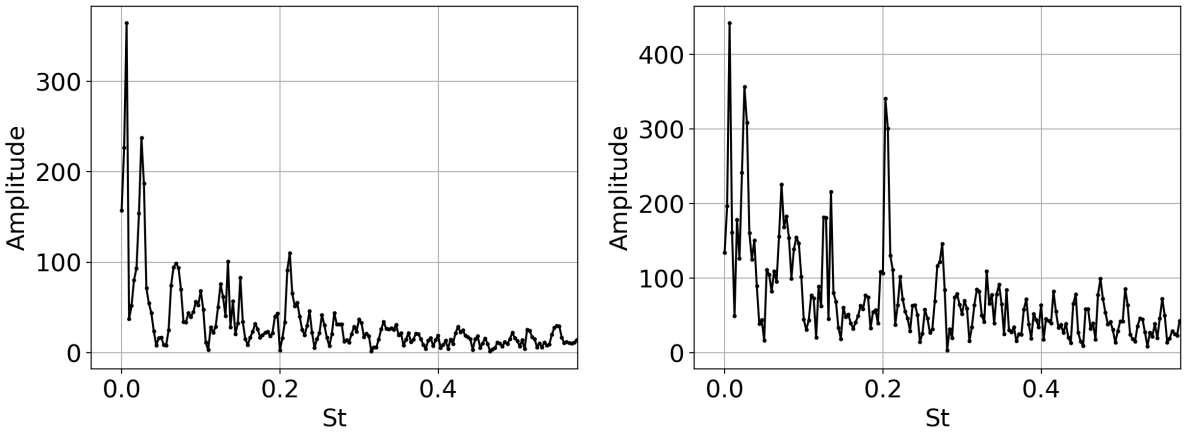

(a) Probe 1.

(b) Probe 5.

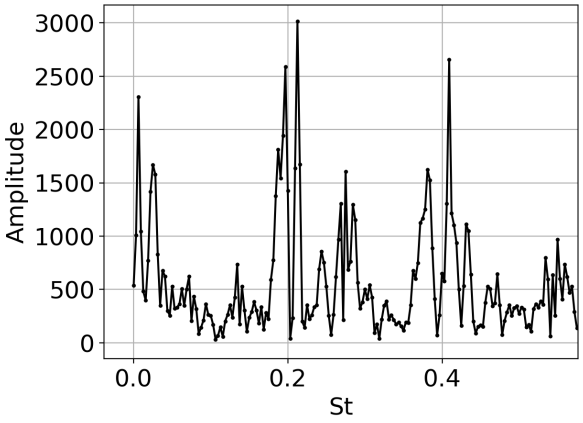

(c) Probe 7.

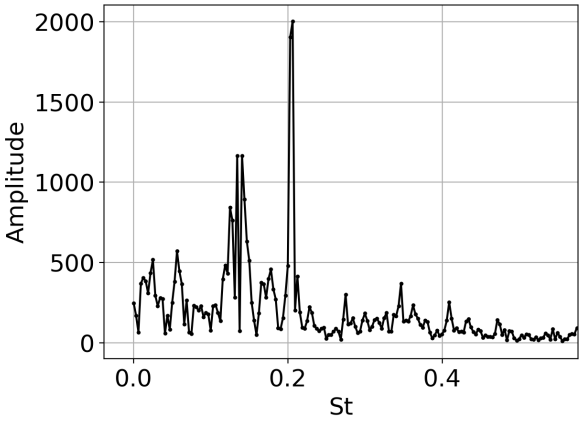

(d) Probe 10.

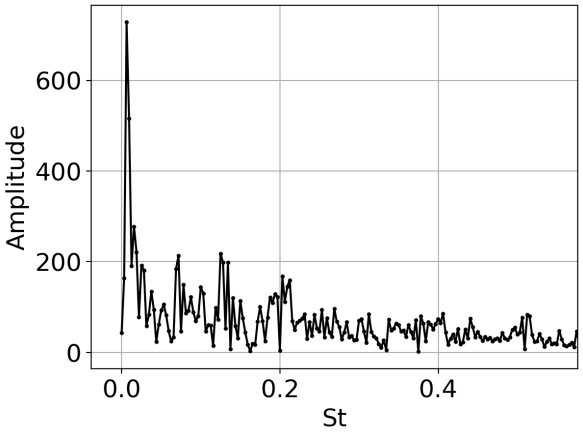

(e) Probe 13.

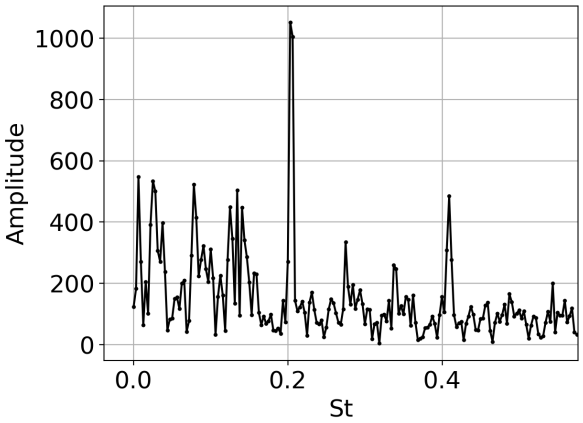

(f) Probe 16.

Figura 4.25 – Pressure spectra.

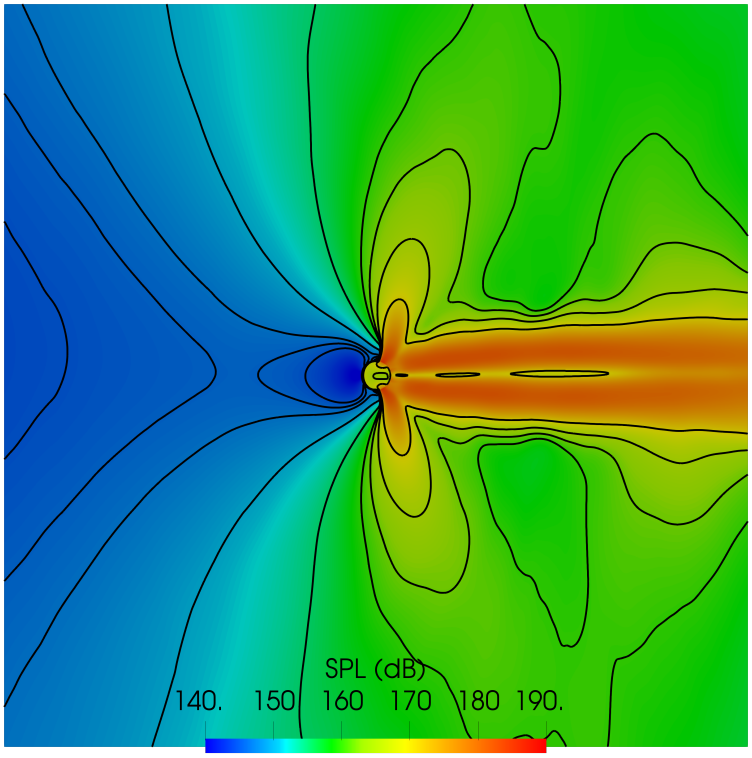

Figura 4.26 – Sound Pressure Level field, $M_\infty = 0.75$.

much more complex, and requires more modes to be properly described.

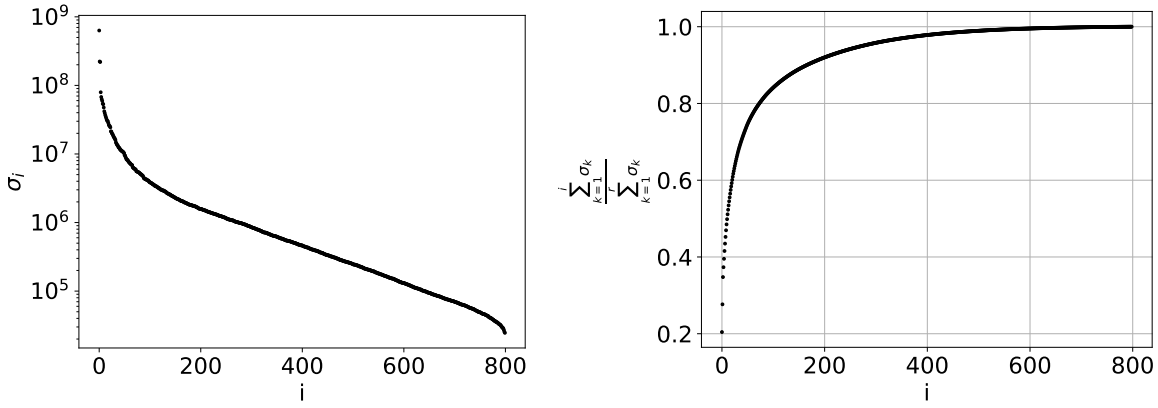

(a) Singular values

(b) Partial sum of the singular values

Figura 4.27 – Singular values of the data matrix $\mathbf{X}$.

The POD again decomposed the flow in a mean flow, mode 1, in figure 4.28a, and in modes that account for the pressure fluctuations. It is important to highlight again, however, that the POD modes might contain information about different frequencies. The acoustic region of modes 2 and 8, seen in figures 4.28b and 4.28d, present structures that resemble acoustic dipoles, and the very low magnitudes of the modes in the upwind region show how the mean flow affects the sound waves propagating upwind. It is also possible to see a pattern in the downwind of the flow that resembles the interaction between waves, as if the wake generates noise, and not only the cylinder, a result consistent with the β_T visualisation. These modes decomposed the wake part of the flow in alternating

structures similar to those observed for Mach 0.5 and consistent with the literature. There are also some modes, like the fourth, depicted in figure 4.28c, that present more complex, not well-defined, structures. They appear to be associated with the vortex wake and the acoustic field in the downwind region, considering that the upwind region has a much lower magnitude, but it is difficult to interpret these structures at this point.

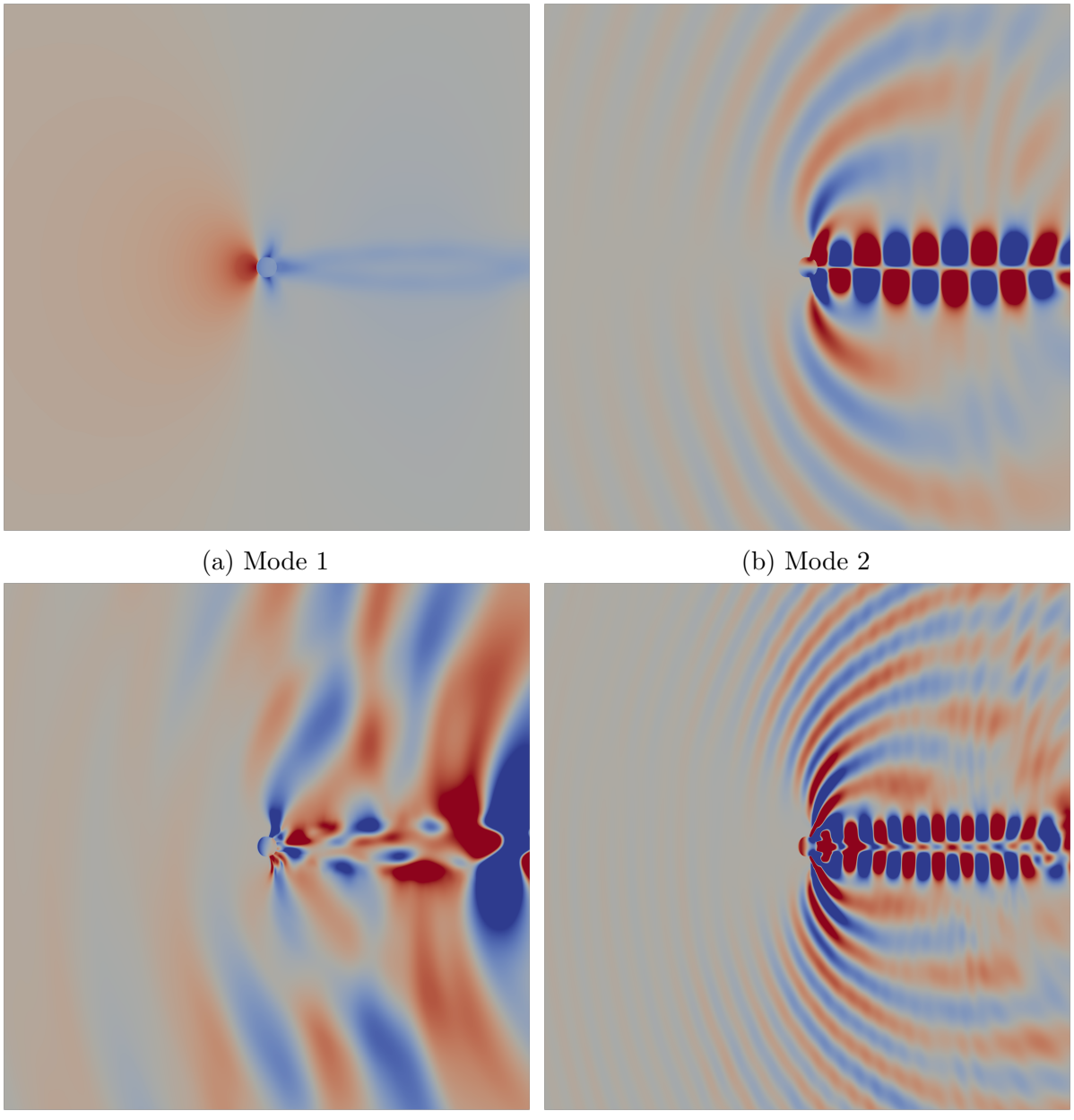

(a) Mode 1

(b) Mode 2

(c) Mode 4

(d) Mode 8

Figura 4.28 – Selected POD modes, $M = 0.75$

The calculated POD modes were used to reconstruct the flow, using equation 2.4. To investigate the influence of the number of modes used, (parameter r in equation 2.4) three reconstructions were performed, using $r = 51$, $r = 91$ and $r = 151$. According to the partial sum of the singular values shown in figure 4.27b, these numbers of modes correspond, respectively, to about 75%, 83% and 89% of the data variance. The results are shown in figure 4.29.

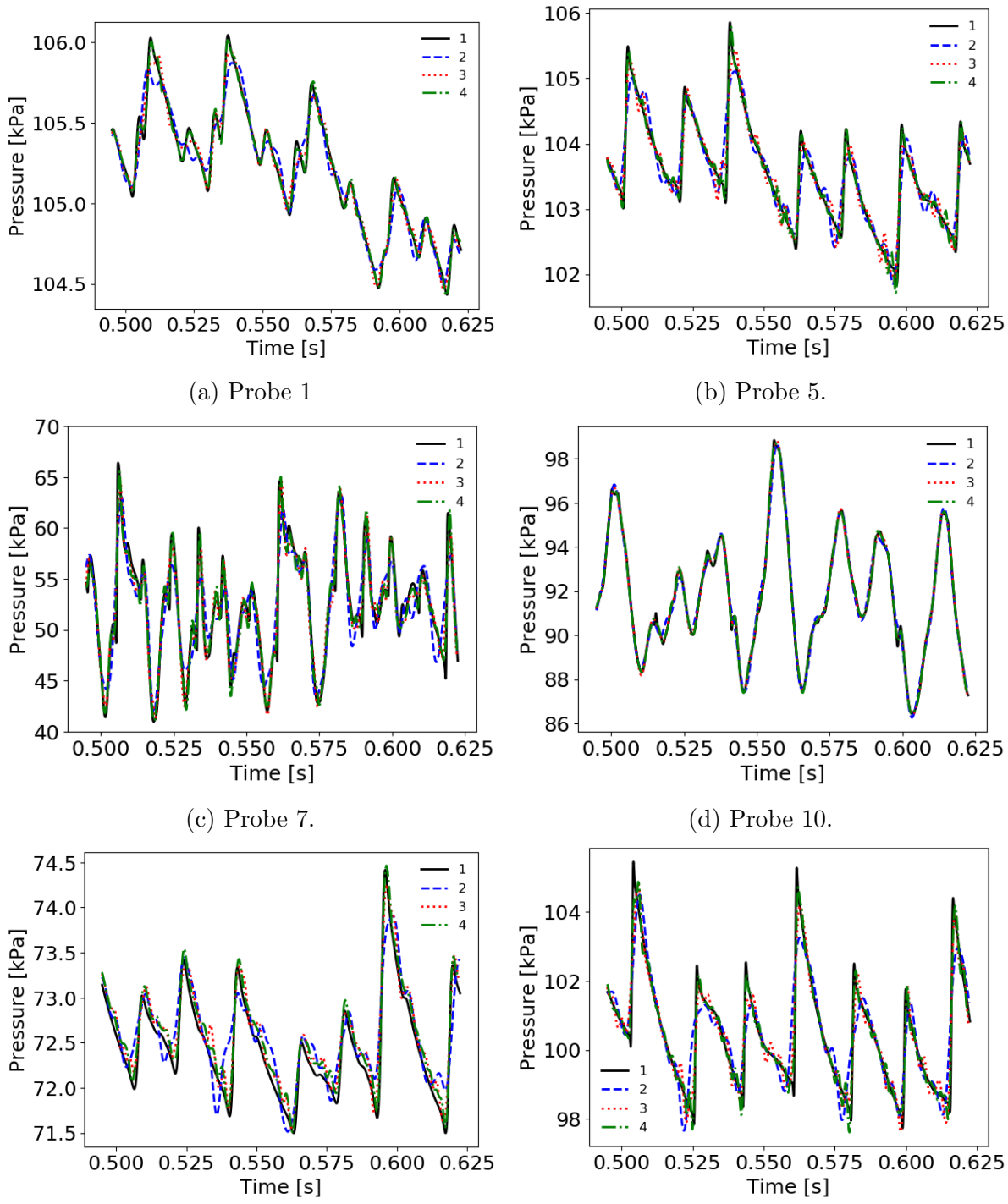

(a) Probe 1

(b) Probe 5.

(c) Probe 7.

(d) Probe 10.

(e) Probe 13.

(f) Probe 16.

Figura 4.29 – Flow reconstruction with different numbers of POD modes 1 - Original signal from the VAT code. 2 - 51 POD modes. 3 - 91 modes. 4 - 151 modes.

The results show that, with 51 modes, the POD describes the flow reasonably well, but there is some error in the signals. The discontinuities at probes 1, 5, 13 and 16 appear to be smoothed and pressure peaks very close to each other, such as those in probes 7 and 10, are merged together. There is also some oscillation, especially in the expansion phase of the waves seen in probes 13 and 16. As the number of modes used grows, the error is reduced. With 91 modes, there is less oscillation, but not all pressure peaks are captured. With 151 modes, there are some small oscillations, especially at probe 13, and some errors

at the amplitudes of the pressure peaks and the extremities of the discontinuities, but overall there is a good agreement with the original data.

4.3.2 Dynamic Modes Decomposition

The Dynamic Modes Decomposition (DMD) was used to decompose the same data set used for the POD analysis in section 4.3.1. In order to compare the results with those for $M_\infty = 0.5$, matrix $\tilde{\mathbf{A}}$ from equation 2.17 was calculated through a projection on the first 21 POD modes (r=21).

Figure 4.30 shows the DMD eigenvalues plotted on the complex plane, along with the unit circle. A difference from the case of $M_\infty = 0.5$ is that the imaginary parts of the eigenvalues are smaller, which means, from equation 2.20, that the frequencies of the modes are smaller. This is also visible in figure 4.31, which shows that the frequencies of the modes only reach the first harmonic of the fundamental frequency $St = 0.2$. This is consistent with the lower frequency content shown in the spectra in figure 4.25.

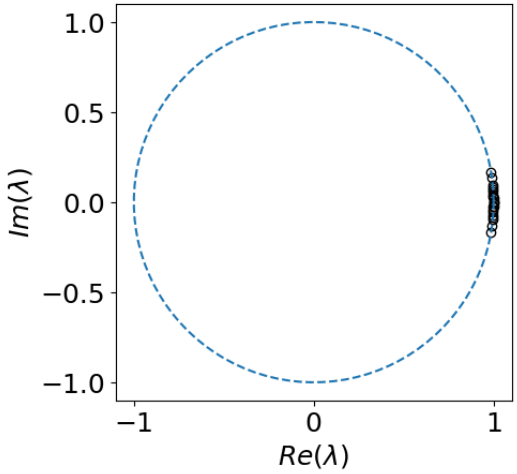

Figura 4.30 – DMD eigenvalues λ.

As all eigenvalues appear to lie on top of the unit circle, the DMD modes can be understood to be marginally stable, an expected result consistent with the data set and similar to the obtained for $M_\infty = 0.5$. However, the observation of the DMD modes' frequencies and rates of growth, depicted in figure 4.31, shows that most modes have non-zero rates of growth ς.

Most have $\varsigma < 0$, which means their amplitudes decrease with time, but modes 1 and 2 actually have positive rates of growth. These deviations from the expected null values are an effect of the higher complexity of the flow. A possibility is that the negative rates of growth are a consequence of the drop in the pressure fluctuations' mean values seen, for example, at probes 1 and 13 (figures 4.22a and 4.24a), between 0.4 s and 0.8 s, as the data set used for the DMD covers a time interval from 0.45 s to 0.65 s, approximately.

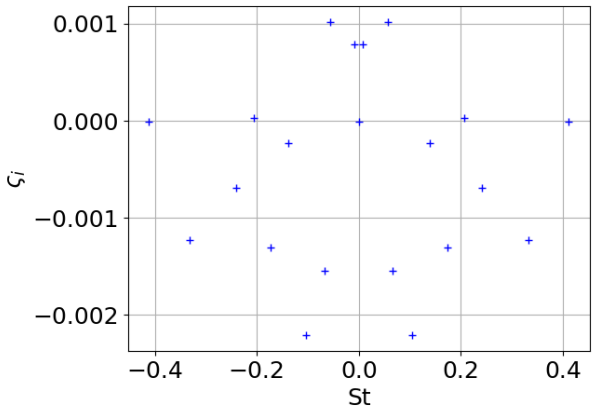

Figura 4.31 – DMD frequencies and rates of growth, $r = 21$, $M_\infty = 0.75$.

By plotting, in figure 4.32, the modes' frequencies as red dashed vertical lines with the pressure spectra at the probes previously presented in figure 4.25, we can associate the modes to specific phenomena seen in the flow.

From probes 7 and 16 (figures 4.32c and 4.32f), we can see that modes 7 and 10 (numbered in crescent order of frequency) are associated with the fundamental frequency of the flow, $St = 0.2$, and it's first harmonic at around $St = 0.4$. Since probe 7 is located inside the vortex wake, we can attribute this fundamental frequency to the rate of emission of vortices. These two modes are depicted in figure 4.33. The acoustic part of these modes resemble acoustic dipoles and are similar to POD modes 2 and 8 in figure 4.28. The modes also show a pattern downwind that indicates that the vortex wake is a source of noise, which is consistent with the flow visualisation in figure 4.21. These modes also reflect the influence of the mean flow on the propagation of noise, favoured in the downwind direction and hindered in the upwind direction. The decomposition of the wake is similar to that obtained for a Mach number of 0.5.

Modes 1 through 6 are all related to lower frequency phenomena (with $St = 0.2$ as reference) and are presented in figure 4.34. Mode 1's frequency is close to $St = 0.006$, a frequency that appears with high amplitude in the spectrum of most probes, especially those upwind (1 and 5) and closest to the cylinder (7 and 13). This indicates that this mode is related to the lower-frequency dynamics shown in the probes' signals in figures 4.22a and 4.24a. It is also possible to see in the pressure and β_T fields in figure 4.21, that sound waves are emitted in clusters of wave fronts, which might account for the lower frequency effect. These wavefronts are also similar to the vertical structure of the mode.

Modes 2 and 3 have frequencies close to each other and to peaks that appear in the spectra for probes 1 and 5 ($St = 0.07$), probe 10 ($St = 0.056$), and with smaller amplitudes, probes 13 and 16. As these peaks are notably absent in probe 7's spectrum, the only one located inside the wake, these modes are probably related to the acoustic field. They decomposed the acoustic region in mostly vertical structures, in a similar manner to mode 1.

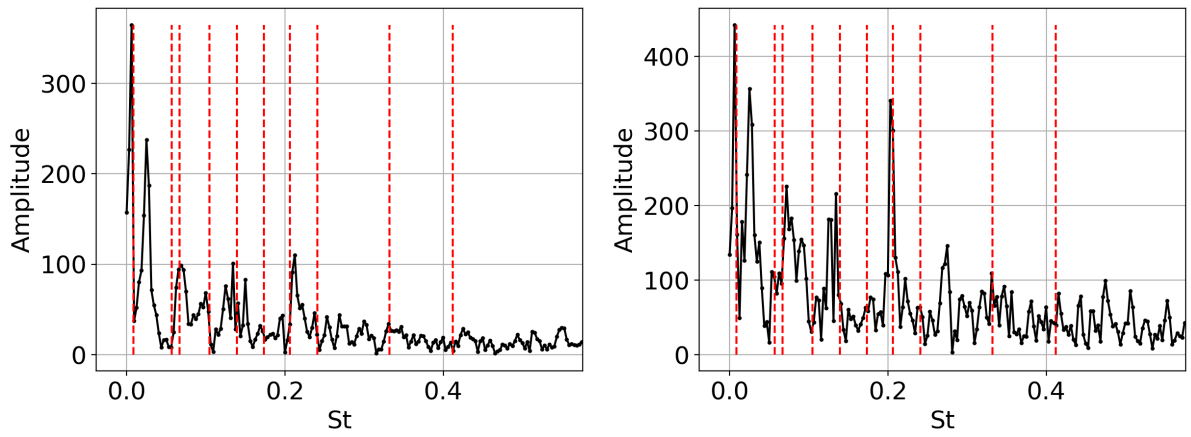

(a) Probe 1

(b) Probe 5

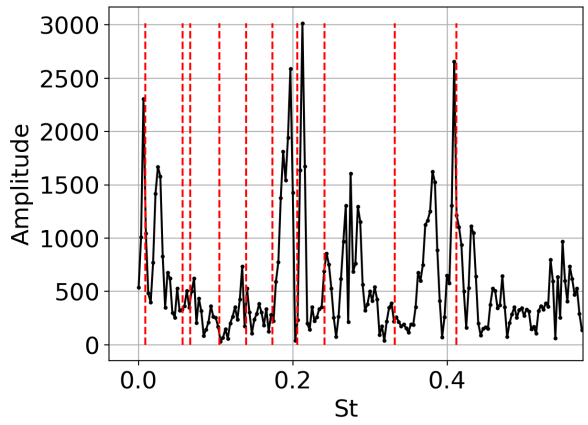

(c) Probe 7

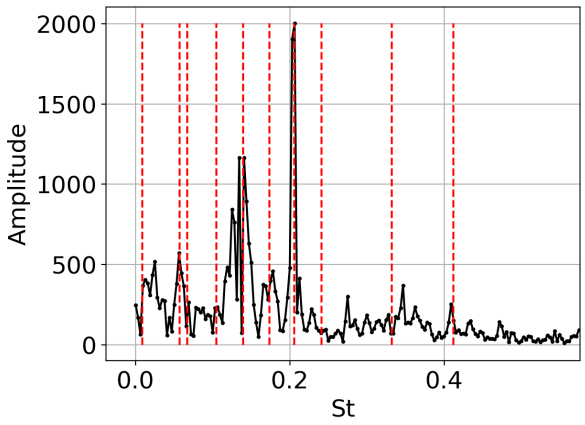

(d) Probe 10

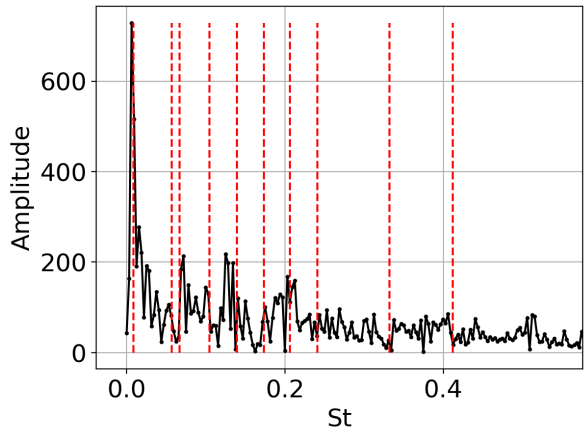

(e) Probe 13

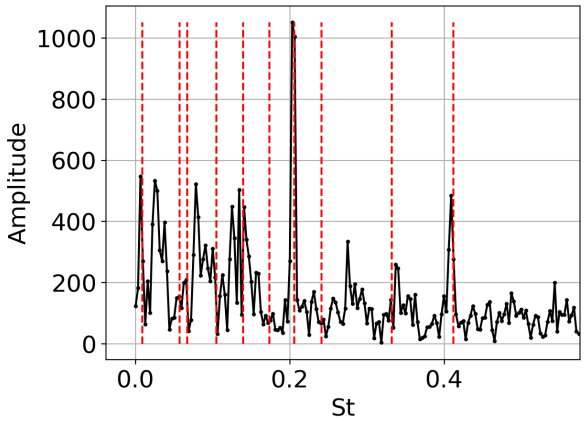

(f) Probe 16

Figura 4.32 – Fourier transform of the pressure signal at different probes. The red dashed vertical lines represent the frequencies of the DMD modes obtained for $r = 21$. $M = 0.75$

Mode 5, with $St = 0.139$, is close to several peaks ($St = 0.12$, 0.13 and 0.14) that appear with larger amplitudes in the spectra for probes 5, 10 and 16, but are also present at the other probes' signals. The acoustic field in this mode also appears to capture the influence of the mean flow on the propagation of the sound waves, as the structures are curved towards the downwind direction, and the upwind region has a much smaller amplitude. In addition to that, the downwind section has structures that resemble the

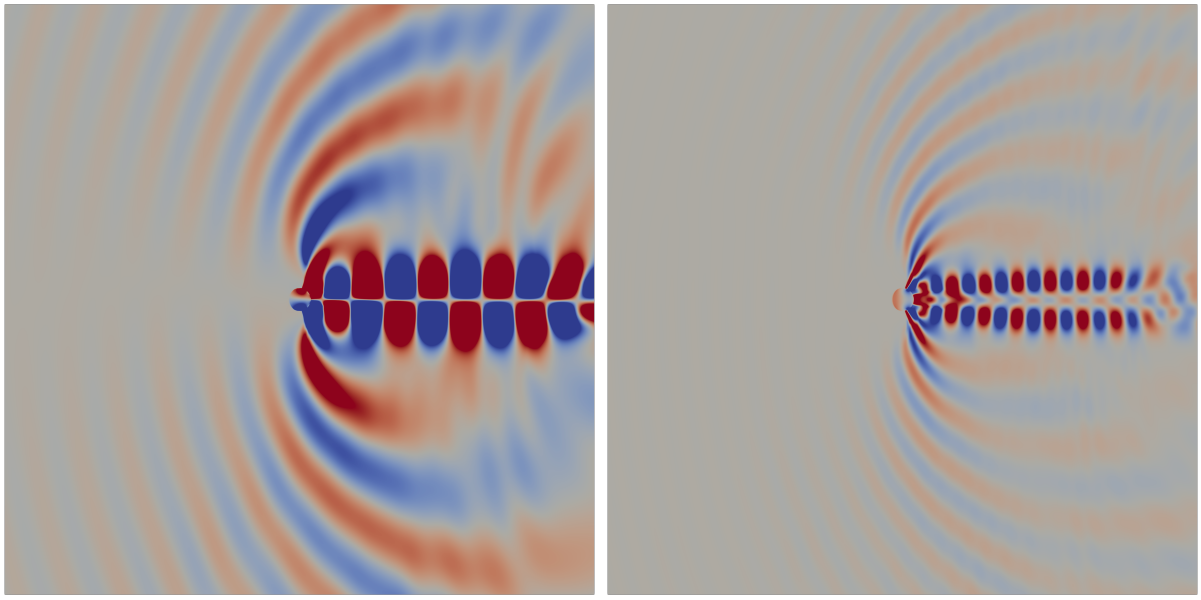

(a) Mode 7, $St = 0.205$ (b) Mode 10, $St = 0.41$

Figura 4.33 – DMD modes 7 and 10.

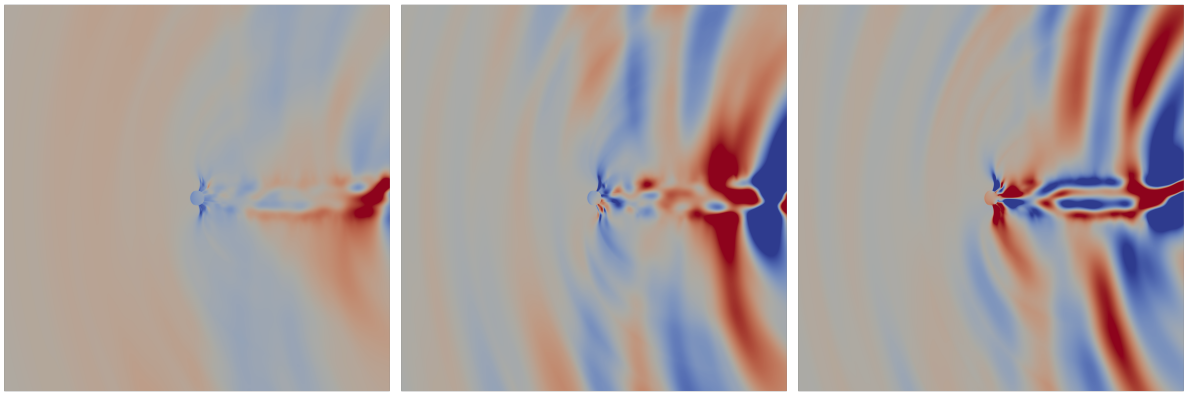

(a) Mode 1, $St = 0.008$. (b) Mode 2, $St = 0.057$. (c) Mode 3, $St = 0.0667$.

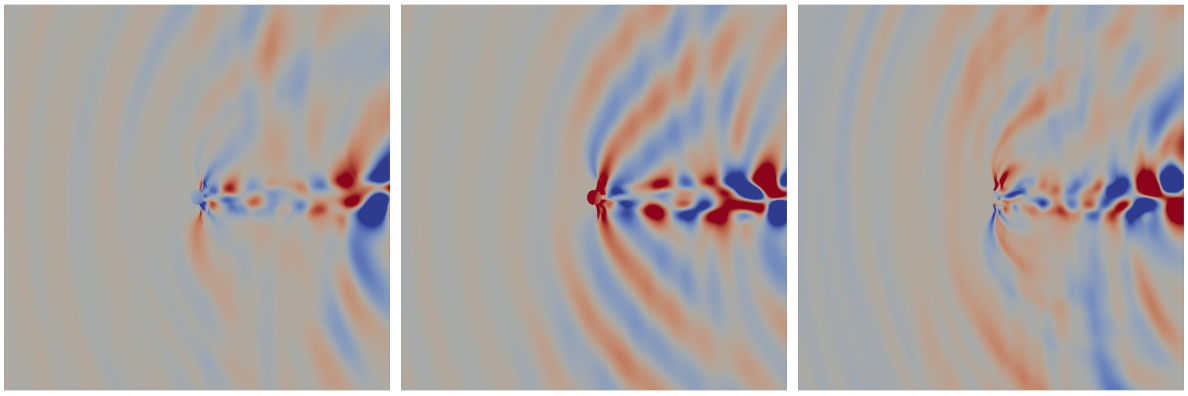

(d) Mode 4, $St = 0.104$. (e) Mode 5, $St = 0.139$. (f) Mode 6, $St = 0.173$.

Figura 4.34 – DMD modes 1 through 6.

interaction of sound waves, in a similar manner to mode 7, which reinforces the observation that the vortex wake emits noise.

Modes 4 and 6 present structures similar to the other modes with $St < 0.2$, but their frequencies do not correspond to any significant peaks at the spectra, so it is difficult

to obtain new information from them.

Figure 4.35 presents DMD modes 8 and 9. Their structures are similar to mode 5, with an acoustic field that shows the influence of the mean flow, and a pattern in the downwind part that indicates noise being emitted from the wake. In addition to that, mode 8 has a frequency associated with a small peak in the spectrum for probe 7, located inside the vortex wake, which further indicates it is related to this part of the flow field. At mode 9's frequency, there is a small peak in the spectrum for probe 16, located above the cylinder at $y = 10$.

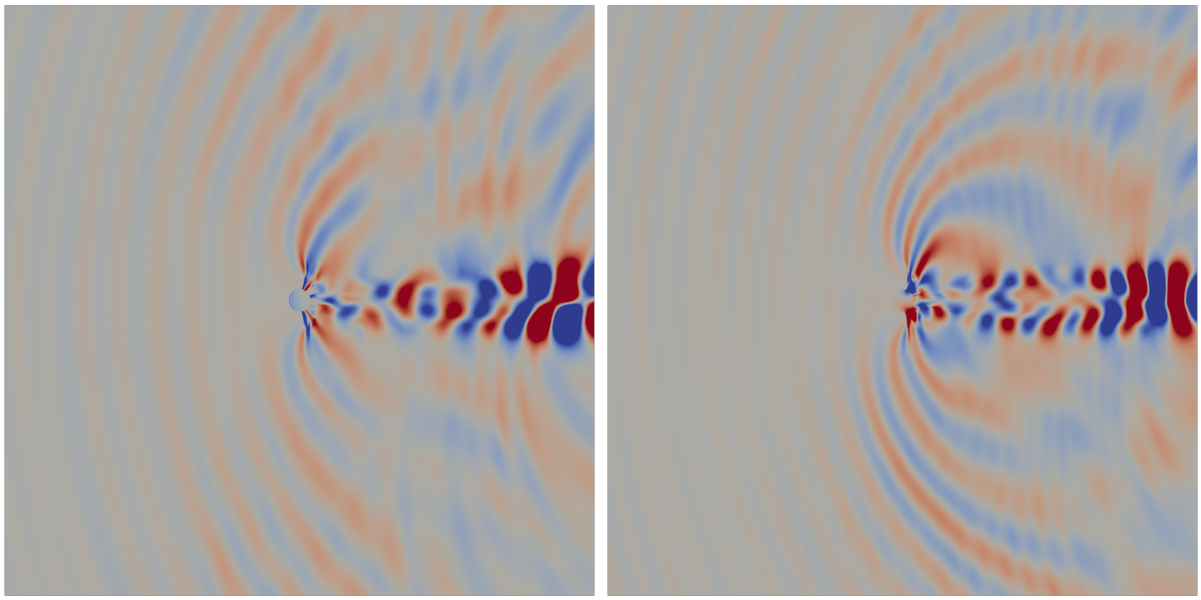

(a) Mode 8, $St = 0.24$ (b) Mode 9, $St = 0.0.33$

Figura 4.35 – DMD modes 8 and 9.

It is interesting to note that, while some modes (in particular, modes 4 and 6) cannot be clearly associated with important frequencies in the spectra, there are several peaks around $St = 0.27$ that appear with relatively high amplitudes in the spectra from probes 5, 7 and 16, but there is no DMD mode associated with these frequencies.

4.3.3 Flow reconstruction with the DMD modes

The flow around the cylinder with $M_\infty = 0.75$ was reconstructed with the 21 DMD modes presented in section 4.3.2, through equation 2.22, and the results are shown in figure 4.36. It is clear from the reconstructed signals that, with 21 modes, the DMD method is unable to describe the dynamics of the flow. The reconstructed signals in all probes show large errors, although in some cases, such as probes 5 and 16, there is some similarity in the signals. Due to these large discrepancies, a more detailed analysis of the error for the Sound Pressure Level and p'_{rms}, such as the one conducted in section 4.2.3, was considered unnecessary.

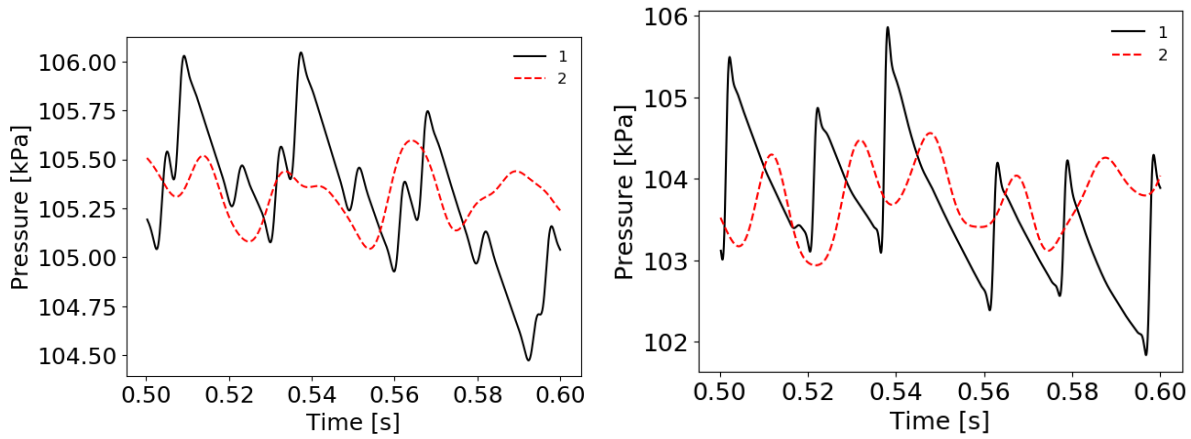

(a) Probe 1

(b) Probe 5

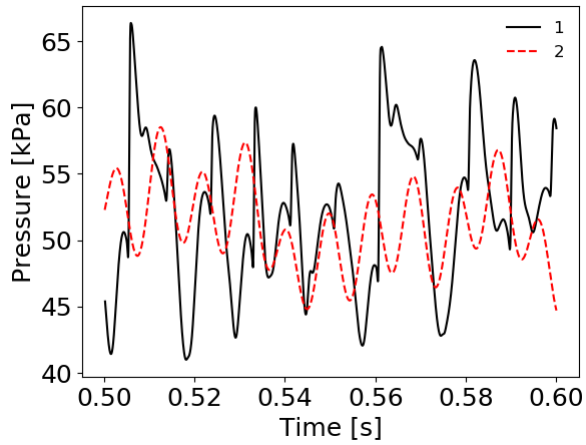

(c) Probe 7

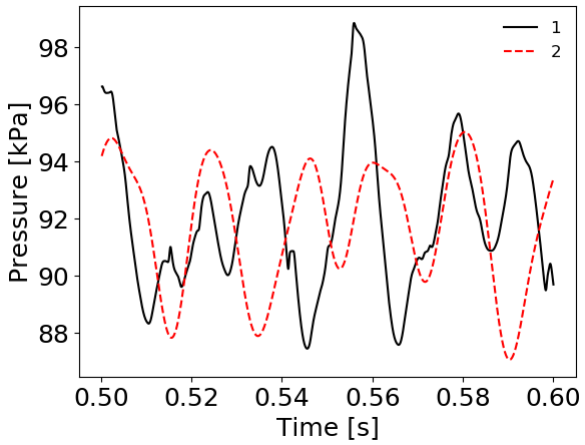

(d) Probe 10

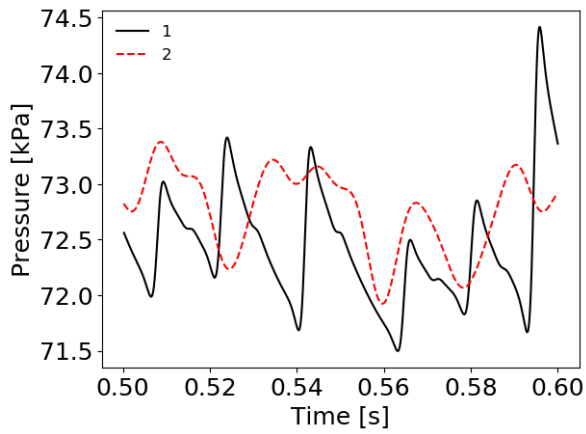

(e) Probe 13

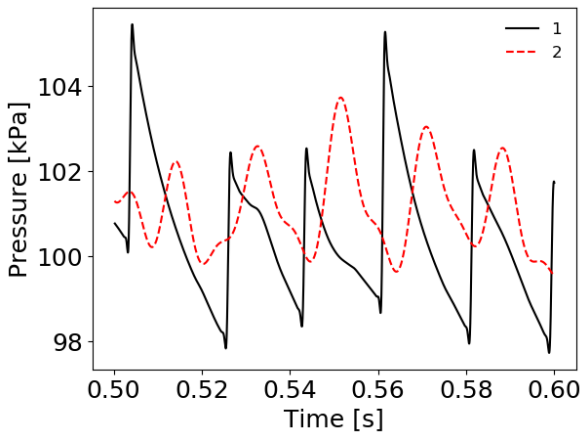

(f) Probe 16

Figura 4.36 – Pressure signals, $M_\infty = 0.75$. 1: Original result from the vat code. 2: DMD reconstruction with 21 modes.

This large error observed for the DMD reconstruction is not surprising, as the flow with $M_\infty = 0.75$ is much more complex than with $M_\infty = 0.5$ and, according to the partial sum of the singular values shown in figure 4.27b, the first 21 POD modes account for only about 60% of the variance of the data. Thus, it is expected that the projection of the matrix $\mathbf{A}$, of the equivalent linear system, on this basis would not capture enough of the dynamics of the flow. The reconstruction was performed with 21 modes for two main

reasons: to allow for a direct comparison to the results for the flow with a Mach number of 0.5, and because the modes are divided in a mean flow, with $St = 0$, and 10 pairs of complex conjugate modes, and we were able to analyse all 10 distinct modes in detail, seeking a physical interpretation (with 51 modes, for example, the analysis of 25 different modes would be much more difficult).

To investigate if a decomposition with more DMD modes leads to better reconstruction results, the data set was decomposed into 51 and 91 modes. This means that matrix $\tilde{\mathbf{A}}$ was calculated with a basis formed by POD modes that contain, respectively, 75% and 83% of the variance of the data. The results are depicted in figure 4.37. Even with more DMD modes, the reconstructed signals in all probes continue to be very distant from the original results from the simulation. It is possible to see that, in comparison to the case with 21 modes, the new signals have components with higher frequencies and, in this aspect, some get closer to the original signals, such as probe 7. However, the discrepancies in mean value, phase and amplitude of oscillation remain significant, and in some cases, are even larger than for $r = 21$.

A more detailed analysis of the new eigenvalues provides some insight into what happens when we increase the number of modes in the DMD decomposition. Figure 4.38 shows the new DMD eigenvalues, plotted in the complex plane along with the unitary circle. In a similar manner to the results for 21 modes (figure 4.30), all eigenvalues lie approximately on the unit circle, but it is possible to see that, as the number of modes increases, the maximum frequency of the modes (given by the phase of the eigenvalues, per equation 2.20) increases, even though the spectra for the probes, in figure 4.25, show no relevant frequencies beyond $St \approx 0.4$.

Figure 4.39 shows the DMD eigenvalues, plotted according to their frequencies (Strouhal numbers) and rates of growth, obtained with decompositions with $r = 51$ (figure 4.39a), and $r = 91$ (figure 4.39b), and a comparison of the results from these two cases and $r = 21$, in figure 4.39c. As observed with the results in figure 4.38, as more modes are used for the decomposition, more modes appear with higher frequencies, not observed in the spectra of the pressure signals. In addition to that, there are modes with more significant rates of decay. The comparison of the results shows that, when the number of modes is increased, a whole new set of DMD modes is generated, unlike the POD method, in which more modes are added to the existing set.

This issue with the flow reconstruction with the DMD modes was also reported by Alenius (2012), and among the explanations, the author mentioned that the constant growth factors of the DMD modes might not be a physically accurate representation.

The fact that the added modes did not improve the results for the reconstruction of the flow, combined with the observations about the new modes' frequencies and rates of growth, indicate that not all eigenvalues of $\tilde{\mathbf{A}}$ are physically relevant. This observation was also made by other authors and motivated the development of DMD variations that

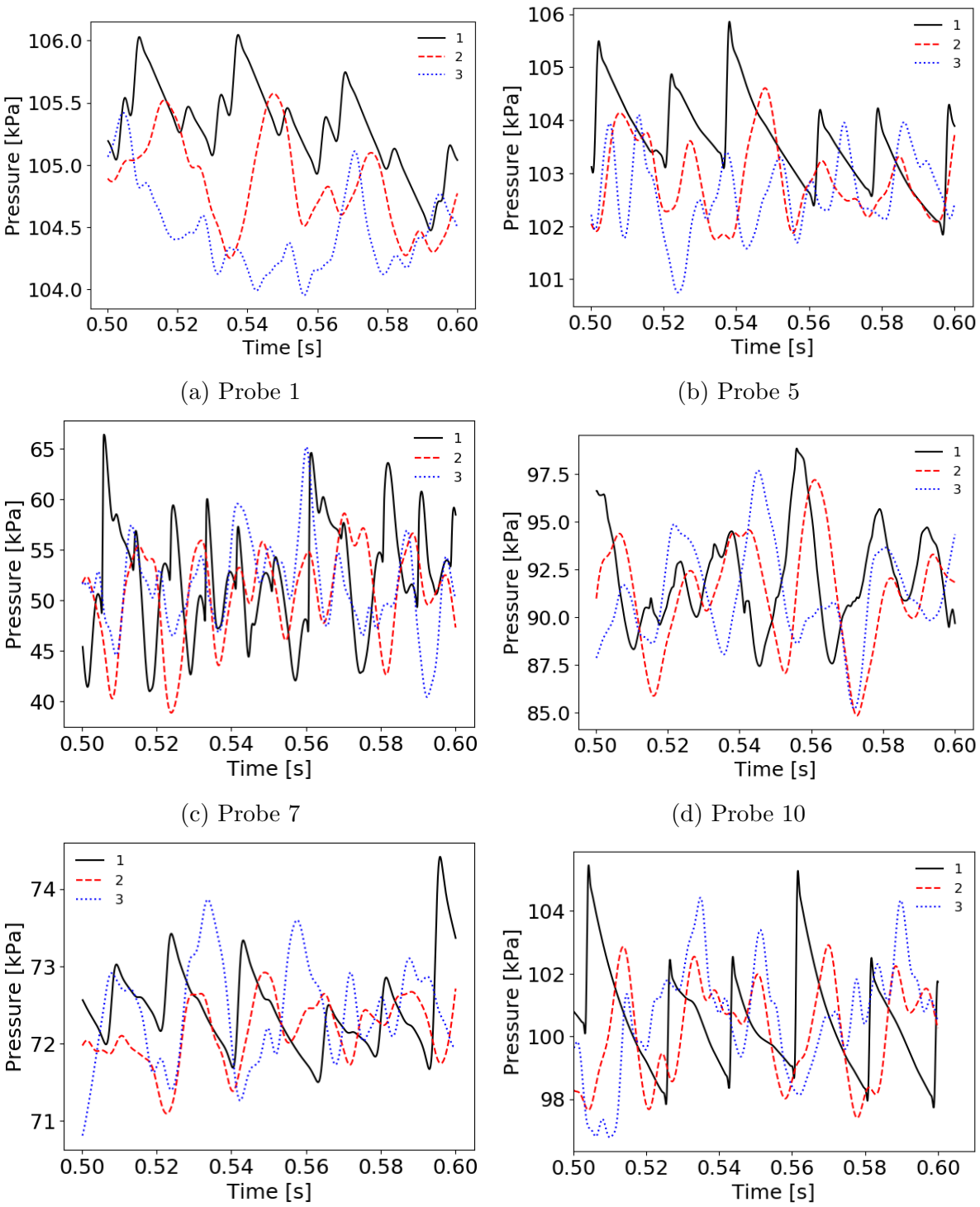

(a) Probe 1

(b) Probe 5

(c) Probe 7

(d) Probe 10

(e) Probe 13

(f) Probe 16

Figura 4.37 – Pressure signals, $M_\infty = 0.75$. 1: Original result from the vat code. 2: DMD reconstruction with 51 modes. 3: DMD reconstruction with 91 modes.

use optimisation algorithms to select the most relevant modes and find the amplitudes of the modes that result in the best reconstruction (JOVANOVIC; SCHMID; NICHOLS, 2014),(OHMICHI, 2017). To investigate this effect, we calculated the amplitudes of the modes as

$$|\boldsymbol{\varphi}_i| = \frac{\langle \boldsymbol{\varphi}, \mathbf{x}_1 \rangle}{\langle \mathbf{x}_1, \mathbf{x}_1 \rangle^{1/2}}, \tag{4.4}$$

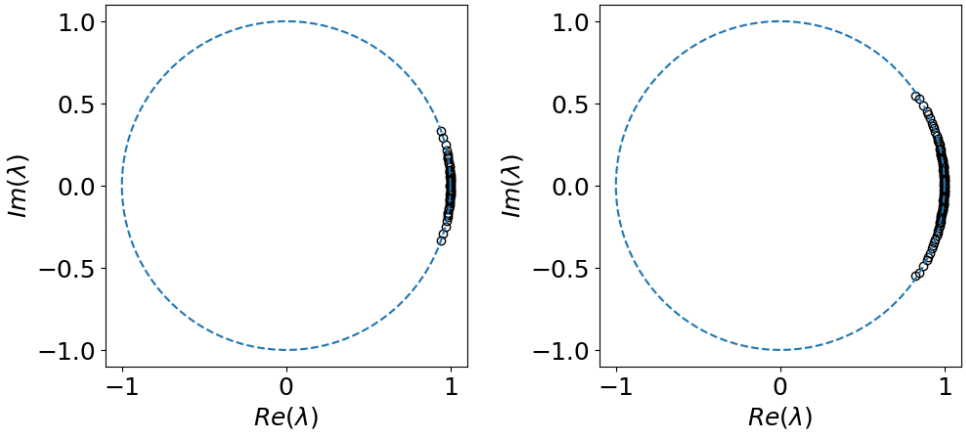

(a) $r = 51$ (b) $r = 91$

Figura 4.38 – DMD eigenvalues, $M = 0.75$

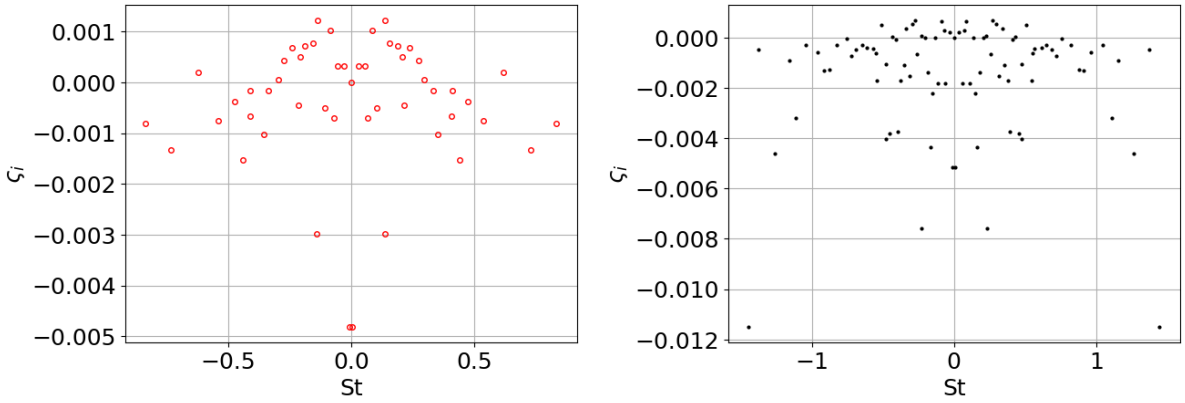

(a) 51 modes. (b) 91 modes.

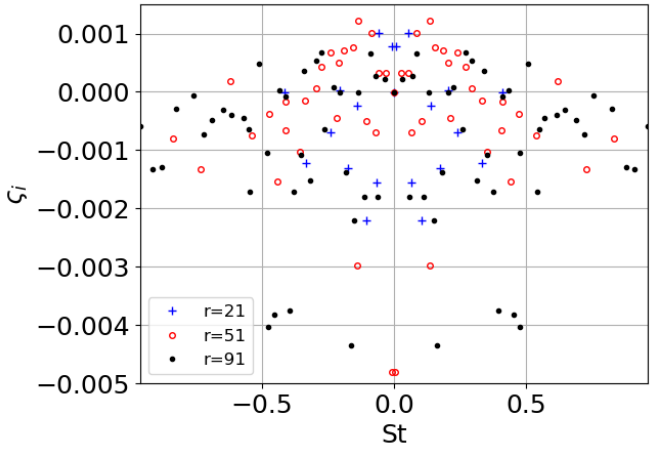

(c) Comparison for different numbers of modes.

Figura 4.39 – DMD frequencies and rates of growth, $M = 0.75$.

where $\boldsymbol{\varphi}_i$ is the ith DMD mode, $\mathbf{x}_1$ is the first snapshot and $\langle \cdot, \cdot \rangle$ denotes the inner product. The resulting amplitudes calculated for different numbers of modes r are depicted in figure 4.40. The vertical grey line represents $St = 0.2$. The figure shows that, regardless of the number of modes, the mean flow, associated with $St = 0$, has the largest amplitude, equal to 1. It is interesting to note that for $St = 0.2$, marked with the grey vertical line in the

figure, the amplitudes of the modes are some of the lowest for all cases. The harmonics of this mode, with $St = 0.4$, show the same behaviour with some of the lowest amplitudes. This is an unexpected result, as the spectra for the pressure signals showed that these are some of the most important frequencies of the flow, but might explain the discrepancies between the original signals and the DMD reconstructions. For different frequencies, figure 4.40 shows that the modes not only often have much higher amplitudes than those with Strouhal numbers of 0.2 and 0.4, but modes with similar frequencies have very different amplitudes when calculated with different values of r. These results further reinforce the need for selecting the most relevant modes and amplitudes to obtain better reconstructions, highlighted by the previously mentioned authors.

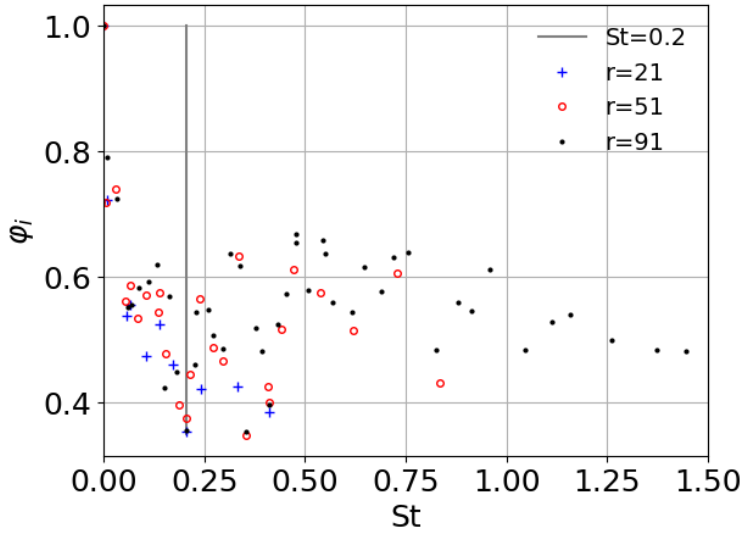

Figura 4.40 – Amplitude of the DMD modes for different numbers of calculated modes, $M_\infty = 0.75$.

5 Conclusion

The present work investigated the transonic flow around a cylinder with Mach numbers 0.5 and 0.75. We used a finite volumes discretization combined with an immersed boundary method, implemented in the VAT code, to solve the Euler Equations. The results were consistent with numerical and experimental results found in the literature (RODRIGUEZ, 1984; BOTTA, 1995). The flow with $M_\infty = 0.5$ was periodic, with vortex shedding and emission of pressure waves with a Strouhal number of 0.18. The flow with $M_\infty = 0.75$ was much more complex and with other frequency components but still had a dominant Strouhal number of 0.2.

The POD and DMD methods were implemented in FORTRAN language codes. This choice was made because the outputs from the VAT code were written in FORTRAN binary files, and it is not trivial to read these files with other programming languages. The implementations were straightforward, as the algorithms are relatively simple, and LAPACK functions were used to calculate the SVD and the eigendecomposition. The POD and DMD were used to decompose data sets composed of pressure snapshots from the simulations. The most time-consuming steps were the SVD and the data input, but the most important constraint for the analyses was a large memory cost, a problem intensified by the use of double precision for all variables in the code.

The modal decomposition with the POD and DMD methods revealed interesting features about the flows. The acoustic region of flow with $M_\infty = 0.5$ was decomposed with the DMD in a fundamental mode with $St = 0.18$ and the shape of a dipole, and in harmonics of this first mode, with shapes of acoustic multipoles. The decomposition of the vortex street had alternating structures similar to the decomposition of the incompressible wake presented in other works. The POD modes for the flow with $M_\infty = 0.5$ had structures very similar to the DMD modes even though the former are orthogonal structures without frequency distinction, while the latter are not necessarily orthogonal but have distinct frequencies and rates of growth.

The DMD decomposition of the flow with $M_\infty = 0.75$ revealed more interesting structures. In addition to a mode with $St = 0.2$ and the shape of a dipole and its also dipole-shaped harmonic with $St = 0.4$, modes with different shapes and frequencies corresponded to other peaks in the spectra for the pressure fluctuations. We attempted to interpret the DMD modes by comparing the modes' frequencies with the spectra at

different flow regions, as some peaks were more relevant in some probes and not in others. Additionally, the DMD modes revealed that the vortex street also acts as a sound source, an observation consistent with the visualisation of shock waves in the wake, that detach and propagate as noise.

The flows were reconstructed using the POD and the DMD modes. The reconstruction with the POD modes had an excellent agreement with the original data, and for $M_\infty = 0.75$, it was clear that, as more POD modes are used, the reconstruction results improve. This is an expected result since the POD is a method constructed to decompose the data in the optimal basis for the reconstruction. The reconstruction with the DMD, on the other hand, presented more discrepancies when compared to the original flow. For $M_\infty = 0.5$, the reconstruction captured some important elements of the flow, such as the frequencies and amplitudes of the waves, pressure discontinuities and smoother pressure fluctuations, but there were phase and mean value errors and strong oscillations in the expansion phase of the waves in the acoustic region. For $M_\infty = 0.75$, the reconstructed pressure signals had even greater discrepancies when compared to the original data. Changes in the composition of the snapshots and variations in the data set and the number of DMD modes did not result in much better reconstruction results. This difficulty in reconstructing the data with the DMD modes has also been described by other authors (ALENIUS, 2012), and attributed to the fact that the DMD modes have constant growth or decay rates, but this might not represent the data set accurately. The change from discrete to continuous time domain in the DMD might also introduce some errors, and it is possible that small mismatches in the phase for each DMD mode result in a large reconstruction error when the modes are added. This effect can also explain the better agreement between the data and the reconstruction with the discrete equation $\tilde{\mathbf{x}}_{k+1} = \tilde{\mathbf{A}}\tilde{\mathbf{x}}_k$, presented in figure 4.17. Some authors, such as Jovanovic, Schmid e Nichols (2014) and Ohmichi (2017) also proposed variations to the DMD method that use optimisation methods to select the DMD modes that best describe the flow. Schmid (2022) presents a broad review of variations to the original DMD algorithm.

5.1 Suggestions for further work

Even though the transonic flow around a cylinder is a well-described problem (BOTTA, 1995), the acoustic field that results from the detachment and propagation of the shock waves has not been described in detail before and could be further studied with other methods and models for the flow. There is also room for a more rigorous, formal grid convergence analysis, as only a simple qualitative comparison between two discretizations was performed in this work.

An immediate continuation of this work could be using single precision variables for the POD and DMD analyses. Even though this might result in some loss of information,

it would greatly reduce the memory cost of the decompositions and would allow for the use of larger data sets, with a higher sampling frequency or covering a larger time interval, or snapshots including the velocity field in addition to the pressure, as mentioned by Seid et al. (2012), for example. This might help improve the reconstruction results. In addition to that, it would also be interesting to investigate the influence of the time step between successive snapshots on the DMD results.

Another possibility for further study is to calculate the DMD using data from a small number of probes positioned along the domain, instead of using the entire pressure fields. This approach is more compatible with the form experimental data is usually acquired, either through accelerometers for structural vibrations or through pitot tubes or hot wire anemometers for fluid flows, for example. In this context, the simulation data could be used to define the optimal positions for the sensors in experiments, in the sense that they would provide the best data set to a posterior DMD analysis.

Another interesting next step is the implementation of variations of the DMD method. The DMD algorithms with optimised mode selection (JOVANOVIC; SCHMID; NICHOLS, 2014; OHMICHI, 2017) could be used in an attempt to obtain better reconstruction results with the data sets used in this work. The parallel and streaming algorithms by Hemati, Williams e Rowley (2014) and Anantharamu e Mahesh (2019), for example, would not only save memory due to their streaming feature but also allow for more efficient use of the AMADEA cluster through shared memory parallelism. They could also be implemented directly into the VAT code, thus saving the time required to generate and read the snapshots.

The development or use of existing reduced order models based on the POD and DMD methods would also be an interesting evolution of this research, and a ROM could even be integrated into traditional CFD codes. Anantharamu e Mahesh (2019), for example, present an error analysis that could be used as a stopping criterion for the CFD code, and from this point forward, a reduced order model based on the DMD could be used to further describe the flow.

References

ALENIUS, E. *Flow Duct Acoustics - An LES Approach*. 2012. Tese (Doutorado) — Department of Aeronautical and Vehicle Engineering, Royal Institute of Technology, Stockholm. Cited 5 times on pages 1, 17, 18, 74 e 79.

ALENIUS, E. et al. Large eddy simulations of acoustic-flow interaction at an orifice plate. *Journal of Sound and Vibration*, v. 345, p. 162–177, 2015. ISSN 0022-460X. Disponível em: <https://www.sciencedirect.com/science/article/pii/S0022460X15001467>. Cited on page 17.

ALI, M. Y. et al. Dynamic mode decomposition of fast pressure sensitive paint data. *Sensors*, v. 16, n. 6, 2016. ISSN 1424-8220. Disponível em: <https://www.mdpi.com/1424-8220/16/6/862>. Cited on page 18.

ANANTHARAMU, S.; MAHESH, K. A parallel and streaming dynamic mode decomposition algorithm with finite precision error analysis for large data. *Journal of Computational Physics*, v. 380, 2019. Cited 3 times on pages 19, 36 e 80.

ANDERSON, D. A. et al. *Computational Fluid Mechanics and Heat Transfer*. 2. ed. [S.l.]: Taylor e Francis, 1997. Cited 4 times on pages 21, 22, 27 e 29.

ANDERSON, J. D. *Computational FLuid Dynamics. An Introduction*. 3. ed. [S.l.]: Springer, 2009. Cited on page 27.

ANDERSON, J. D. *Fundamentals of Aerodynamics*. 6. ed. New York: McGraw-Hill Education, 2017. Cited on page 6.

BAGHERI, S. Koopman-mode decomposition of the cylinder wake. *Journal of Fluid Mechanics*, Cambridge University Press, v. 726, p. 596–623, 2013. Cited 2 times on pages 15 e 46.

BELLIZZI, S.; SAMPAIO, R. Poms analysis of randomly vibrating systems obtained from karhunen–loève expansion. *Journal of Sound and Vibration*, v. 297, n. 3, p. 774–793, 2006. ISSN 0022-460X. Disponível em: <https://www.sciencedirect.com/science/article/pii/S0022460X06003427>. Cited on page 12.

BERKOOZ, G. et al. The proper orthogonal decomposition in the analysis of turbulent flows. *Annual Review of Fluid Mechanics*, v. 25, p. 539–575, 1993. Cited on page 10.

BOTTA, N. The inviscid transonic flow about a cylinder. *Journal of Fluid Mechanics*, Cambridge University Press, v. 301, p. 225–250, 1995. Cited 7 times on pages 7, 8, 37, 61, 62, 78 e 79.

BROATCH, A. et al. Dynamic mode decomposition of the acoustic field in radial compressors. *Aerospace Science and Technology*, v. 90, p. 388–400, 2019. ISSN 1270-9638.

Disponível em: <https://www.sciencedirect.com/science/article/pii/S1270963819304298>. Cited on page 18.

BUNING, P.; STEGER, J. Solution of the two-dimensional euler equations with generalized coordinate transformation using flux vector splitting. In: *AIAA/ASME 3rd Joint Thermophysics, Fluids, Plasma and Heat Transfer Conference*. [s.n.], 1982. Disponível em: <https://arc.aiaa.org/doi/abs/10.2514/6.1982-971>. Cited on page 7.

CHEN, N. et al. Effects of low-frequency noise from wind turbines on hearth rate variability in healthy individuals. *Scientific Reports*, v. 11, 2021. Disponível em: <https://10.1038/s41598-021-97107-8>. Cited on page 1.

EMBRAER. *Sustainability in action – Embraer's roadmap for a greener future*. 2022. Blog post. Disponível em: <https://www.embraercommercialaviation.com/sustainability-in-action-embraers-roadmap-for-a-greener-future/>. Cited on page 2.

FELLI, M. et al. A novel approach for the isolation of the sound and pseudo-sound contributions from near-field pressure fluctuation measurements: Analysis of the hydroacoustic and hydrodynamic perturbation in a propeller-rudder system. *Experiments in Fluids*, v. 55, 12 2013. Cited on page 2.

FRANK, H. M.; MUNZ, C.-D. Direct aeroacoustic simulation of acoustic feedback phenomena on a side-view mirror. *Journal of Sound and Vibration*, v. 371, p. 132–149, 2016. ISSN 0022-460X. Disponível em: <https://www.sciencedirect.com/science/article/pii/S0022460X1600136X>. Cited on page 18.

GERBRANDS, J. J. On the relationships between svd, klt and pca. *Pattern Recognition*, v. 14, n. 1, p. 375–381, 1981. ISSN 0031-3203. 1980 Conference on Pattern Recognition. Disponível em: <https://www.sciencedirect.com/science/article/pii/0031320381900820>. Cited on page 10.

GOWEN, F. E.; PERKINS, E. W. Drag of circular cylinders for a wide range of reynolds numbers and mach numbers. *NACA Research Memorandum*, 1952. Cited on page 6.

HEMATI, M. S. et al. Dynamic mode decomposition for large and streaming datasets. *Physics of Fluids*, v. 26, n. 11, p. 111701, 2014. Disponível em: <https://doi.org/10.1063/1.4901016>. Cited 4 times on pages 16, 19, 36 e 80.

HOLMES, P. et al. *Turbulence, Coherent Structures, Dynamical Systems and Symmetry*. 2. ed. Cambridge: Cambridge University Press, 2012. Cited 2 times on pages 11 e 55.

HOLTON, J. R.; HAKIM, G. J. *An Introduction to Dynamic Meteorology*. 5. ed. Oxford: Elsevier, 2013. Cited on page 21.

HUGHES, T. J. R.; TEZDUYAR, T. E. Finite elements method for first-order hyperbolic systems with particular emphasis on the compressible euler equations. *Computer Methods in Applied Mechanics and Engineering*, v. 45, p. 217–284, 1984. Cited on page 7.

IATA. *Net-Zero Carbon Emissions by 2050*. 2021. Press Release, 4 October 2021. Disponível em: <https://www.iata.org/en/pressroom/pressroom-archive/2021-releases/2021-10-04-03/>. Cited on page 2.

JAMESON, A. et al. Numerical solutions of the euler equations by finite volume methods using runge-kutta time-stepping schemes. In: AIAA (Ed.). *14th Fluid and Plasma Dynamics Conference*. [s.n.], 1981. Disponível em: <https://arc.aiaa.org/doi/abs/10.2514/6.1981-1259>. Cited on page 26.

JOURDAIN, G. et al. Application of dynamic mode decomposition to acoustic-modes identification and damping in a 3-dimensional chamber with baffled injectors. *Journal of Sound and Vibration*, v. 332, n. 18, p. 4308–4323, 2013. ISSN 0022-460X. Disponível em: <https://www.sciencedirect.com/science/article/pii/S0022460X13002162>. Cited on page 17.

JOVANOVIC, M. R. et al. Sparsity-promoting dynamic mode decomposition. *Physics of Fluids*, v. 26, n. 2, 2014. ISSN 1070-6631. Disponível em: <https://doi.org/10.1063/1.4863670>. Cited 4 times on pages 18, 75, 79 e 80.

King III, W. A precis of developments in the aeroacoustics of fast trains. *Journal of Sound and Vibration*, v. 193, n. 1, p. 349–358, 1996. ISSN 0022-460X. Disponível em: <https://www.sciencedirect.com/science/article/pii/S0022460X96902758>. Cited on page 1.

KUTZ, J. N. et al. *Dynamic Modes Decomposition: Data-Driven Modeling of Complex Systems*. 1. ed. Philadelphia: SIAM, 2016. ISBN 9781611974508. Cited 4 times on pages 13, 15, 46 e 58.

LIU, H. et al. Analysis of pressure fluctuation in transonic cavity flows using modal decomposition. *Aerospace Science and Technology*, v. 77, p. 819–835, 2018. ISSN 1270-9638. Disponível em: <https://www.sciencedirect.com/science/article/pii/S1270963817321648>. Cited on page 18.

LUI, H. F. S.; WOLF, W. R. Construction of reduced-order models for fluid flows using deep feedforward neural networks. *Journal of Fluid Mechanics*, Cambridge University Press, v. 872, p. 963–994, 2019. Cited on page 12.

LUMLEY, J. L. The structure of inhomogeneous turbulence. *Atmospheric Turbulence and Wave Propagation*, p. 166–178, 1967. Cited 2 times on pages 2 e 10.

MAIER, M.; KRONBICHLER, M. Efficient parallel 3d computation of the compressible euler equations with an invariant-domain preserving second-order finite-element scheme. *ACM Transactions on Parallel Computing*, v. 8, p. 1–30, 09 2021. Cited on page 8.

MISERDA, R. B.; LEAL, R. Numerical simulation of the unsteady aerodynamic forces over a circular cylinder in transonic flow. In: *44th AIAA Aerospace Sciences Meeting and Exhibit*. [s.n.], 2006. Disponível em: <https://arc.aiaa.org/doi/abs/10.2514/6.2006-1408>. Cited on page 7.

MISERDA, R. F. B. et al. Numerical simulation of rotor-stator interaction noise in transonic cascades. *Journal of Propulsion and Power*, v. 36, n. 3, p. 363–380, 2020. Disponível em: <https://doi.org/10.2514/1.B37627>. Cited 3 times on pages 26, 30 e 38.

MONGEAU, L. et al. Aircraft noise technology review and medium and long term noise reduction goals. *Proceedings of Meetings on Acoustics*, v. 19, n. 1, 2013. ISSN 1939-800X. 040041. Disponível em: <https://doi.org/10.1121/1.4800944>. Cited on page 2.

NAIR, V. et al. Inspecting sound sources in an orifice-jet flow using lagrangian coherent structures. *Computers & Fluids*, v. 140, p. 397–405, 2016. ISSN 0045-7930. Disponível em: <https://www.sciencedirect.com/science/article/pii/S0045793016302626>. Cited on page 17.

NICHOLS, J. W. et al. Stability and modal analysis of shock/boundary layer interactions. *Theoretical and Computational Fluid Dynamics*, v. 31, n. 1, p. 33–50, 2017. Disponível em: <https://doi.org/10.1007/s00162-016-0397-6>. Cited on page 16.

OHMICHI, Y. Preconditioned dynamic mode decomposition and mode selection algorithms for large datasets using incremental proper orthogonal decomposition. *AIP Advances*, v. 7, n. 7, 2017. Disponível em: <https://doi.org/10.1063/1.4996024>. Cited 4 times on pages 19, 75, 79 e 80.

OHMICHI, Y. et al. Modal decomposition analysis of three-dimensional transonic buffet phenomenon on a swept wing. *AIAA Journal*, v. 56, n. 10, p. 3938–3950, 2018. Cited on page 19.

PALLAS, M.-A. et al. Towards a model for electric vehicle noise emission in the european prediction method cnossos-eu. *Applied Acoustics*, v. 113, p. 89–101, 2016. ISSN 0003-682X. Disponível em: <https://www.sciencedirect.com/science/article/pii/S0003682X16301608>. Cited on page 1.

PANDOLFI, M.; LAROCCA, F. Transonic flow about a circular cylinder. *Computers & Fluids*, v. 17, n. 1, p. 205–220, 1989. ISSN 0045-7930. Disponível em: <https://www.sciencedirect.com/science/article/pii/0045793089900170>. Cited on page 7.

PIMENTA, B. G. *Simulação numérica de ondas não lineares em dinâmica dos gases e ruído de interação rotor-estator em turbofans aeronáuticos*. 2016. Tese (Doutorado) — Departamento de Engenharia Mecânica, Univeridade de Brasília, Brasília. Cited 2 times on pages 25 e 30.

PRIEBE, S. et al. Low-frequency dynamics in a shock-induced separated flow. *Journal of Fluid Mechanics*, Cambridge University Press, v. 807, p. 441–477, 2016. Cited on page 16.

RAGHUNATHAN, R. S. et al. Aerodynamics of high-speed railway train. *Progress in Aerospace Sciences*, v. 38, n. 6, p. 469–514, 2002. ISSN 0376-0421. Disponível em: <https://www.sciencedirect.com/science/article/pii/S0376042102000295>. Cited on page 1.

RICCIARDI, T. R. et al. Numerical noise prediction and source identification of a realistic landing gear. *Journal of Sound and Vibration*, v. 496, 2021. Disponível em: <https://www.sciencedirect.com/science/article/pii/S0022460X21000055>. Cited on page 12.

RODRIGUEZ, O. The circular cylinder in subsonic and transonic flow. *AIAA Journal*, v. 22, n. 12, p. 1713–1718, 1984. Disponível em: <https://doi.org/10.2514/3.8842>. Cited 2 times on pages 7 e 78.

SARMAST, S. et al. Mutual inductance instability of the tip vortices behind a wind turbine. *Journal of Fluid Mechanics*, Cambridge University Press, v. 755, p. 705–731, 2014. Cited on page 16.

SAUCY, A. et al. Does night-time aircraft noise trigger mortality? a case-crossover study on 24 886 cardiovascular deaths. *European Heart Journal*, v. 42, n. 8, p. 835–843, 11 2020. ISSN 0195-668X. Disponível em: <https://doi.org/10.1093/eurheartj/ehaa957>. Cited on page 1.

SCHMID, P. J. Dynamic mode decomposition of numerical and experimental data. *Journal of Fluid Mechanics*, Cambridge University Press, v. 656, p. 5–28, 2010. Cited 3 times on pages 3, 13 e 15.

SCHMID, P. J. Dynamic mode decomposition and its variants. *Annual Review of Fluid Mechanics*, v. 54, n. 1, p. 225–254, 2022. Disponível em: <https://doi.org/10.1146/annurev-fluid-030121-015835>. Cited 2 times on pages 19 e 79.

SCHMID, P. J. et al. Applications of the dynamic mode decomposition. *Theoretical and Computational Fluid Dynamics*, v. 25, n. 1, p. 249–259, 2011. Disponível em: <https://doi.org/10.1007/s00162-010-0203-9>. Cited on page 15.

SCHMID, P. J.; SESTERHENN, J. Dynamic mode decomposition of numerical and experimental data. In: AMERICAN PHYSICAL SOCIETY. *61st Annual Meeting of the APS Division of Fluid Dynamics*. [S.l.], 2008. Cited on page 3.

SEID, K.-H. et al. A comparison study of reduced order models for aeroacoustic applications. In: *18th AIAA/CEAS Aeroacoustics Conference (33rd AIAA Aeroacoustics Conference)*. [s.n.], 2012. Disponível em: <https://arc.aiaa.org/doi/abs/10.2514/6.2012-2072>. Cited 3 times on pages 17, 55 e 80.

SEIDLER, A. et al. The effect of aircraft, road, and railway traffic noise on stroke – results of a case–control study based on secondary data. *Noise and Health*, v. 20(95), p. 152–161, 2018. Cited on page 1.

SIROVICH, L. S. Turbulence and the dynamics of coherent structures part i: Coherent structures. *Quarterly of Applied Mathematics*, Brown University, v. 45, n. 3, p. 561–571, 1987. Disponível em: <http://www.jstor.org/stable/43637457>. Cited on page 11.

STATNIKOV, V. et al. Analysis of characteristic wake flow modes on a generic transonic backward-facing step configuration. *European Journal of Mechanics - B/Fluids*, v. 59, p. 124–134, 2016. ISSN 0997-7546. Cited on page 16.

TAKAHASHI, S. et al. A numerical scheme based on an immersed boundary method for compressible turbulent flows with shocks: Application to two-dimensional flows around cylinders. *Journal of Applied Mathematics*, v. 2014, 2014. Disponível em: <https://doi.org/10.1155/2014/252478>. Cited on page 8.

TAM, C. K. et al. Numerical simulation of a slit resonator in a grazing flow under acoustic excitation. *Journal of Sound and Vibration*, v. 313, n. 3, p. 449–471, 2008. ISSN 0022-460X. Cited on page 2.

TANG, S. et al. Numerical investigation of the influences of the features of transonic flow over a hemispherical turret on beam wavefront distortions. *Journal of Applied Fluid Mechanics*, v. 16, n. 3, p. 443–458, 2023. ISSN 1735-3572. Disponível em: <https://www.jafmonline.net/article_2157.html>. Cited on page 13.

TEFF-SEKER, Y. et al. Noise pollution from wind turbines and its effects on wildlife: A cross-national analysis of current policies and planning regulations. *Renewable and Sustainable Energy Reviews*, v. 168, 2022. ISSN 1364-0321. Disponível em: <https://www.sciencedirect.com/science/article/pii/S1364032122006852>. Cited on page 1.

THOMAS, J. P. et al. Three-dimensional transonic aeroelasticity using proper orthogonal decomposition-based reduced-order models. *Journal of Aircraft*, v. 40, n. 3, p. 544–551, 2003. Disponível em: <https://doi.org/10.2514/2.3128>. Cited on page 12.

TORIJA, A. J. et al. Psychoacoustic analysis of contra-rotating propeller noise for unmanned aerial vehicles. *J Acoust Soc Am*, v. 149, p. 835–846, 2021. Disponível em: <https://doi.org/10.1121/10.0003432>. Cited on page 2.

TRINDADE, M. et al. Karhunen–loève decomposition of coupled axial/bending vibrations of beams subject to impacts. *Journal of Sound and Vibration*, v. 279, n. 3, p. 1015–1036, 2005. ISSN 0022-460X. Disponível em: <https://www.sciencedirect.com/science/article/pii/S0022460X04000574>. Cited on page 12.

VANHERPE, F. et al. Sound vs. pseudo-sound contributions to the wind noise. In: AIAA (Ed.). *18th AIAA/CEAS Aeroacoustics Conference*. [S.l.: s.n.], 2012. Cited on page 1.

VIOLATO, D.; SCARANO, F. Three-dimensional vortex analysis and aeroacoustic source characterization of jet core breakdown. *Physics of Fluids*, v. 25, n. 1, 2013. Disponível em: <https://doi.org/10.1063/1.4773444>. Cited on page 12.

WEISS, J. A tutorial on the proper orthogonal decomposition. In: *AIAA Aviation 2019 Forum*. [s.n.], 2019. Disponível em: <https://arc.aiaa.org/doi/abs/10.2514/6.2019-3333>. Cited 2 times on pages 11 e 43.

WHITE, F. M. *Fluid Mechanics*. 8. ed. New York: McGraw-Hill Education, 2016. Cited 2 times on pages 6 e 9.

XU, C. Y. et al. Numerical simulation of shock wave and turbulence interaction over a circular cylinder. *Modern Physics Letters B*, v. 23, n. 03, p. 233–236, 2009a. Disponível em: <https://doi.org/10.1142/S0217984909018084>. Cited on page 7.

XU, C. Y. et al. Effect of mach number on transonic flow past a circular cylinder. *Chinese Science Bulletin*, v. 54, n. 11, p. 1886–1893, 2009b. ISSN 1861-9541. Cited on page 7.

XU, C. Y. et al. Large-eddy simulation of the compressible flow past a wavy cylinder. *Journal of Fluid Mechanics*, Cambridge University Press, v. 665, p. 238–273, 2010. Cited on page 8.

XU, L. et al. A data-driven reduced order modeling for fluid flow analysis based on series forecasting intelligent algorithm. *IEEE Access*, v. 10, p. 60163–60176, 2022. Cited on page 12.